Wave-Cavity Resonator: Experimental Investigation of an Alternative Energy Device

by

Jonathan Daniel Reaume
B.Eng. , University of Victoria , 2011

A Thesis Submitted in Partial Fulfillment
of the Requirements for the Degree of

MASTER OF APPLIED SCIENCE

in the Department of Mechanical Engineering

Supervisory Committee

Wave-Cavity Resonator: Experimental Investigation of an Alternative Energy Device

by

Jonathan Daniel Reaume
B.Eng. , University of Victoria , 2011

Supervisory Committee

Dr. Peter Oshkai, (Department of Mechanical Engineering)
Supervisor

Dr. Caterina Valeo, (Department of Mechanical Engineering)
Departmental Member

Abstract

Supervisory Committee
Dr. Peter Oshkai, (Department of Mechanical Engineering)
Supervisor
Dr. Caterina Valeo, (Department of Mechanical Engineering)
Departmental Member

A wave cavity resonator (WCR) is investigated to determine the suitability of the device as an energy harvester in rivers or tidal flows. The WCR consists of coupling between self-excited oscillations of turbulent flow of water in an open channel along the opening of a rectangular cavity and the standing gravity wave in the cavity. The device was investigated experimentally for a range of inflow velocities, cavity opening lengths, and characteristic depths of the water. Determining appropriate models and empirical relations for the system over a range of depths allows for accuracy when designing prototypes and tools for determining the suitability of a particular river or tidal flow as a potential WCR site. The performance of the system when coupled with a wave absorber/generator is also evaluated for a range piston strokes in reference to cavity wave height. Video recording of the oscillating free-surface inside the resonator cavity in conjunction with free-surface elevation measurements using a capacitive wave gauge provides representation of the resonant wave modes of the cavity as well as the degree of the flow-wave coupling in terms of the amplitude and the quality factor of the associated spectral peak. Moreover, application of digital particle image velocimetry (PIV) provides insight into the evolution of the vortical structures that form across the cavity opening. Coherent oscillations were attainable for a wide range of water depths. Variation of the water depth affected the degree of coupling between the shear layer oscillations and the gravity wave as well as the three-dimensionality of the flow structure. In terms of the power investigation, conducted with the addition of a load cell and linear table-driven piston, the device is likely limited to running low power instrumentation unless it can be up-scaled. Up-scaling of the system, while requiring additional design considerations, is not unreasonable; large-scale systems of resonant water waves and the generation of large scale vortical structures due to tidal or river flows are even observed naturally.

Table of Contents

List of Tables

List of Figures

Acknowledgments

I would like to thank my advisor, Dr. Peter Oshkai, for his invaluable guidance and advice that has been essential in the completion of this research endeavor and for providing me access to the world of research while still completing my undergraduate degree. I am grateful for the knowledge of fluid dynamics and flow induced vibrations that he has shared.

I am grateful to my friends and colleagues Andrew, Majid, Mostafa, Oleksandr, Krishna, Victor, Gorkem, and Jeremy for their assistance and support for the duration of my research and for the adventures we shared exploring Vancouver Island and fishing during breaks.

I would also like to thank my family for their support and assistance throughout my academic career and my beautiful wife Alyssa for her support, encouragement, and understanding.

Finally, I would like to thank God for the many blessings I have been given, for teaching me patience, and true fulfillment through the gift of his Son.

Dedication

I dedicate this thesis to my family; my beautiful wife Alyssa; parents John and Wendy; brothers Joshua, Jeremy, and Josiah; sisters Shianne, Brianna, Jessy, and Kylie. Without your wisdom, encouragement, support, and love I would not have pursued this goal.

1 Introduction

1.1 Purpose of Thesis

In an effort to find a sustainable balance of energy sources in a modernizing world considerable work has been placed on developing alternative energy devices. One such device that is proposed is the wave-cavity resonator (WCR). This novel device takes advantage of the energy transport from a mean flow to a free surface wave via flow induced resonance. The primary application of the WCR is in small to mid-sized river or tidal systems in which turbine-based alternatives are either too disruptive to ecosystems or to natural appearances. Since free surface waves are commonly observed in shallow rivers and streams along with natural rock channels the negative effect on the associated ecosystems is much reduced. In fact, the side cavities of the proposed systems could even be used as resting areas for various species of fish similar to natural rock formations causing eddies. In order to determine the suitability of such a device it is necessary to gain further insight into the effect of a number of system parameters: in particular, the effect of depth and velocity variations that are common to many river and stream systems. Determining appropriate models and empirical relations for the system over a range of depths would allow accuracy when designing prototypes and tools for determining the suitability of a particular river or tidal flow as a potential WCR site. It is also of great interest to determine the sensitivity and performance of the system during energy harvesting, gain insight into tuning the system for maximum performance, and

comment on how active a control system may be required to operate at if necessary at all and what effects hysteresis and non-linearities may have if found to exist.

1.2 Summary of Contributions

This thesis proposes a number of contributions to the field, many of which are applicable to the future design and evaluation of alternative energy devices based on the coupling of shear layer oscillations with a standing gravity wave mode. Specifically, predictive models for cavity frequency and hydrodynamic frequency are presented and coupling of a locked-on state with a wave absorber is demonstrated without breaking down resonance.

An empirical model for the prediction of the wave frequency in the cavity is adapted from an analogous aero-acoustic model by including effects such as wave celerity variation with depth, added mass, and free surface flow characteristics (Froude number). No previous investigations had been conducted except for a very shallow apparatus; in the current study intermediate and deep water waves are also investigated with and without being coupled to a wave absorber. The models for predicting cavity frequency and wavelength are applied to systems with varying depth and cavity length, two critical system dimensions, with good success. Furthermore, the effect of depth, vortex shedding mode, cavity length, hysteresis and added mass on the resonant response of the system are quantified in terms of the wave mode that is excited, the cavity wave frequency, and the reduced velocity threshold for resonance. Specifically, it is shown that for shallow water wave conditions a closed-closed boundary condition best predicts the cavity frequency and that for intermediate and deep water waves a closed-open boundary

condition solution provides the best fit. An expression for effective cavity length for shallow water waves based on the cavity opening length is demonstrated. Intermediate and deep water wave conditions give an effective cavity length related to the hydraulic diameter based on the analogous aero-acoustic work. Similarly, an empirical expression for predicting hydrodynamic frequency is presented that is analogous to an acoustic system where Froude number replaces the Mach number. In terms of cavity geometry it is shown that above a certain depth, namely the transition from shallow water wave conditions, the natural frequency of the cavity becomes completely dependent on the cavity length; however, the maximum amplitude of the resonant wave is not affected significantly above this depth. Results show that the cavity wave mode typically corresponds to the hydrodynamic mode although mode jumping does occur. Hysteresis is observed when the velocity is gradually increased or decreased in which cases lock-on can occur for a wider band of inflow velocities due to the organization of the free shear layer by interacting with a cavity wave that would not otherwise exist. Hysteresis in the context of this project is where a different state is observed for a set of system parameters depending on the path taken to reach said set of parameters. This includes incrementally changing inflow velocity between data sets instead of starting from zero velocity or physically blocking the cavity opening between data sets to break down resonant coupling. The differences are associated with energy losses due to flow acceleration and formation of large-scale vortical structures via shear layer-cavity wave interactions. A shift in hydrodynamic frequency and shift in cavity wave wavelength are observed when parameters are in vicinity of a locked-on system. Lock-on occurs when the natural frequency of the cavity and the hydrodynamic frequency coincide and large amplitude

oscillations are observed; when a certain threshold between the two frequencies is reached the system pulls the frequencies to a locked-on state. In addition, a sufficiently large ratio of signal power to noise power (unwanted mode frequency components included) is associated with lock-on; for this discussion the ratio is a minimum of 2:1.

Finally, a wave absorber is successfully added to the system in a resonant state demonstrating the potential for a future energy harvesting device. The system has the potential to operate as a wave absorber extracting approximately 18-20% of the available power while still maintaining self-sustained oscillations. A method for predicting wave amplitude using quantitative flow field data is also outlined. Its implementation is left as a point of future work.

1.3 Experimental Methods

The methods used to investigate the above mentioned objectives include Power Spectral Density (PSD) analysis of the time-dependent free surface height data, investigation of the free shear layer and determination of mean inflow velocity using global, quantitative flow imaging using Particle Image Velocimetry (PIV), force measurement of a wave absorber paddle, and free surface image tracking of the cavity waves. Detailed discussion of the experimental system and techniques is given in Chapter 2.

1.4 Flow Regimes

This project involves an experimental investigation of resonant coupling between turbulent flow past a rectangular cavity and a standing gravity wave mode for a range of

parameters, namely the depth and the opening length of the cavity. Schematics displaying the parameters discussed herein can be found in Section 2.1.1; a summary is provided in Figure 1.1.

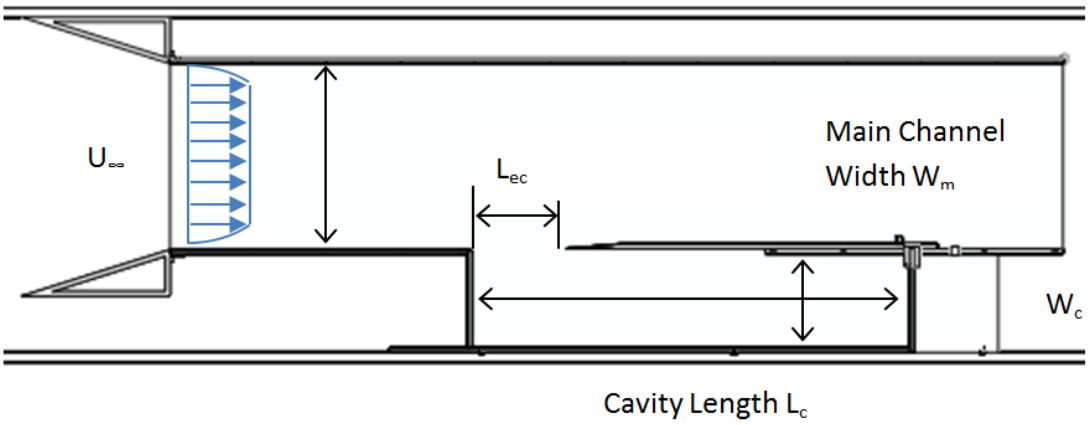

Figure 1.1: Schematic of the WCR (Planform).

The scope of the project includes analysis of the base setup in flows with water depths ranging from 0.02 m to 0.30 m and free stream velocities of 0.278 m/s to 1.10 m/s for a rectangular parallel side branch cavity with rigid walls. The base setup has a cavity width of 0.125 m and a length of 0.622 m and was selected based on maximum wave amplitude and range of self-sustained oscillations observed during a preliminary parameter sweep. The system itself has an overall length of 1.2 m and is inserted into the 2.5 m working length of a 0.45 x 0.45 m water tunnel. An elliptical converging section is mounted upstream of the system to provide a uniform inflow 1 m upstream of the cavity leading edge. An investigation using a piston-type wave absorber travelling over various stroke lengths at depths of 0.102 m and 0.185 m at inflow velocities corresponding to a peak lock-on condition is also within the scope. Analysis of these configurations includes deep, intermediate, and shallow water waves of various modes and amplitudes. The

inflow velocities correspond to turbulent inflow conditions based on the wall length upstream from the cavity leading edge; Froude numbers range from 0.63 to 1.43 based on the mean depth of the cavity. While the resonant mode of interest corresponds to the cavity length, other modes were observed and have been addressed since such an occurrence would be relevant to prototype design and testing. A proposed but yet to be validated empirical model for predicting wave amplitude based on inflow conditions is also included albeit primarily left for future investigation.

1.5 Reference to existing contributions for similar systems

A number of contributions relevant to the WCR project have been published to-date. The general focus has been on the structure of the shear layer that forms across the cavity entrance for various intermediate states between a non-locked-on mode and a fully locked-on mode, conditions present at lock-on, and the feedback mechanism that sustains impinging shear layer oscillations. There is also a vast amount of research on acoustically analogous systems; a detailed summary of the most relevant articles is given followed by a narrative literature review of other relevant sources.

The wave-cavity resonator creates a standing water wave that is sustained by periodic excitation from the free shear layer across the cavity opening. When the frequency of vortex shedding across the opening approaches a natural frequency of the cavity the shear layer can be characterized by the organization of small-scale structures into large-scale voritical structures. This was observed by Ekmekci and Rockwell in the impinging shear flows past a rectangular cavity [1].

1.5.1 Impinging shear flows past rectangular cavities

Ekmekci and Rockwell investigated the behavior of a separated free-shear flow coupled with a gravity wave for the cases of both slotted (shear flow) and unobstructed (free-shear flow) cavity openings [1]. Distinct instabilities for the two cases were observed through variation in dimensionless frequency as inflow velocity was increased to approach a locked-on state. An elongated form of the shear layer consisting of small-scale structures was observed in the absence of lock-on. Large-scale structures after lock-on were observed along with cavity fluid ejections into the main flow. These same observations were made for the range of system parameters of the WCR investigation. The peak magnitude and location of large scale structures were observed to correspond with the degree of lock-on along with increased coherence of phase contours. For fully coupled oscillations a phase difference of $2\pi/3$ was observed in comparison to a phase difference of π prior to the onset of lock-on. In addition, large-scale recirculations were observed and the effect of pulsations through the slotted geometry were investigated. Digital PIV techniques were employed and time traces and spectral analysis of streamwise velocity variations were tracked. The investigation was conducted primarily at a cavity depth of 38.1 mm for a velocity range of 172.8-286.5 mm/s.

Wolfinger, Ozen, and Rockwell later investigated fully-turbulent shallow flows and demonstrated that peak spectral lock-on can occur and that the standing gravity wave (SGW) frequency was close to the theoretical prediction [2]. The characteristics of lock-on were determined and the shear layer RMS velocity and Reynolds stress magnitude were observed to increase. Flow from the shear layer into the cavity at the trailing edge of the cavity and likewise from the cavity to the shear layer at the leading edge was

demonstrated using time-averaged PIV results. Phase-averaged analysis of the results demonstrated the presence of “cyclic” large-scale vortical structures and the transverse velocity in the cavity correlated with the development of these structures. Unlike the parallel side branch WCR that is the focus of this thesis the investigation was performed for a side branch cavity perpendicular to the main channel for shallow flow for a cavity depth of 38 mm and velocity range of 243-470 mm/s.

For shallow flows Tuna, Tinar, and Rockwell investigated the structure of the flow at various planes above the bed and showed that the time-averaged form of the streamlines for any plane above the bed did not change in the presence of a standing gravity wave [3]. Close to the bed secondary flow caused the streamlines to deflect towards the cavity; this result was also seen for the intermediate and deep water wave experiments of this thesis. Mass transfer between the cavity and main flow were once again observed and further investigations using a submerged cylinder at leading edge of the cavity showed a reduction 50% of the mass transferred from the cavity to the free stream [4]. Furthermore, a series of cavities was investigated and showed that highly organized oscillations of longitudinal and transverse modes were relative easy to excite [5]. The coupling is characterized as global as the two waves were observed to be in phase with each other.

In order for the WCR to be of practical use it is necessary to have self-sustained oscillations for which the organized shear layer and cavity wave are mutually affected by each other. A very detailed overview of the behaviour of self-sustained oscillations of impinging shear layers is given for many impingement geometries in an investigation conducted by Rockwell and Naudascher [6]. The impingement oscillations can be

organized into four distinct types of shear layers. These types include planar jets, axisymmetric jets, planar mixing layers, and axisymmetric mixing layers. However, additional classification is necessary if effects such as resonance and elasticity are considered. The research focuses primarily on impingement flow oscillations that are induced by instability in the shear layer, known as instability-induced excitation (IIE), and also on disturbance feedback. The effects of disturbance feedback, frequency and amplitude variations, resonance effects, and characteristics of the onset of oscillation are discussed.

The type of shear layer most relevant to the WCR project is the planar mixing layer of a rectangular cavity. The discussion of the onset of the shear layer oscillations, the instabilities and disturbance feedback mechanism that sustains the oscillations, and the effects of resonance on the system is very interesting and helpful for understanding the behaviour of the WCR system.

The necessary interactions that sustain shear oscillations can be summarized by the following series of events: Flow travels past the leading edge of the cavity and interacts with the pressure field of the cavity which may include impingement on the trailing edge. This disturbance undergoes a feedback effect and propagates upstream to the region of the flow where the shear layer is about to separate. This disturbance then causes localized vorticity fluctuations to occur at this sensitive region where the flow is about to separate and the fluctuations are subsequently amplified as they travel downstream towards the interaction region. These vorticity fluctuations then further interact with the pressure field in the vicinity of the cavity opening and produce an organized disturbance that repeats the cycle. The shed vortices can impinge upon the trailing edge and undergo complete

clipping, partial clipping, or escape the trailing edge altogether. The authors summarize that the feedback mechanism is critical for self-sustained oscillations as it makes the shear-layer oscillation a globally organized phenomenon. For low-flow velocities, the feedback is limited to the near-field and can be categorized as fully-hydrodynamic, pressure-based perturbations.

Rockwell and Naudascher concluded that prediction of non-linear effects such as vortex formation, coalescence, and the behaviour of non-impingement cases is required to accurately predict the main features of oscillating impingement flows. This would suggest that for the WCR system empirical wave amplitude prediction would correlate best with experimentally obtained vorticity data as has been done for acoustically-coupled systems. This thesis outlines an approach specifically for a system coupled with a gravity way. For Rockwell and Naudascher solution models based on finite-difference methods were obtained but limited to the near-field due to the important three dimensional effects that exist in the far region and are not considered in the quasi-2D solution. The authors also concluded that distortions of the mean and unsteady approach flow result from the impingement geometry and must be considered. The impingement geometry also affects formation of vortices at the sensitive leading-edge and results in an additional complication in terms of modelling the free shear layer oscillations. This conclusion is of particular interest to the WCR project and justifies the special impingement plate geometry design that is discussed in Section 2.2.1 and was also used by Rockwell et al in the investigation that is summarized in Section 1.5.1. However, manufacturing of such geometry was not possible within a reasonable time frame and preliminary data was collected with the standard impingement geometry and therefore

used for the entire investigation for consistency. It would be expected that the standard configuration would produce more noise in the system in comparison to a tapered impingement plate. Since location of free surface measurement was a significant distance away from the region of impingement no issues of unexplained noise were observed. In fact, free surface perturbations during impingement may be greater without the tapered impingement plate geometry. Qualitative examination of the resonant coupling is discussed in Section 3.4 to support this justification [7].

1.5.2 Acoustically analogous systems

While limited research has been conducted on water waves in a cavity resonating with shear layer oscillations there has been a great deal of research into acoustic waves in cavities resonating with shear layer oscillations. The acoustic system is highly analogous and much of the theory, observed behaviour and models are relevant to the WCR. An investigation of fully-turbulent pipe inflow past a shallow cavity was carried out by Rockwell, Lin, Oshkai, Reiss, and Pollack (2002) to determine conditions that lead to locked-on states between shear oscillations and acoustic modes of cavities [8]. The Strouhal modes of the cavity oscillations were deduced from examining plan views of the pressure gradients. The organized unsteadiness of the velocity and vorticity fields across the cavity, as discussed by Rockwell and Naudascher [6], was found to be the initial mechanism that eventually leads to a fully-locked on (coupled) state. The investigation makes a number of important conclusions. A hypothesis is made that coupling of acoustic resonant modes of the pipe with the inviscid shear layer instability across the cavity actually strengthens the inherent instability of the shear layer. Results indicate that the mean flow that develops this instability can be represented by the time-averaged flow of

the turbulent background. For relatively long cavity lengths, flow tone generation occurs in large-scale modes and frequency can be scaled with the pipe diameter. The geometry limit is in the range of 1/8 of the pipe diameter and represents the conditions at and below which large-scale mode flow tones cannot be observed due to the acoustic dampening of the system. It was expected that for the WCR project a similar consideration would need to be observed wherein a certain geometry configuration would result in enough bottom friction and visco-thermal dampening to result in an over damped system where no standing gravity waves will be observed. A threshold was also expected for the removal of energy from the cavity-side branch system via the wave absorber after which the fully-coupled, or locked-on state, between the shear layer oscillations and natural modes of the longitudinal waves of the cavity will break down. These considerations are addressed in the discussion of the experimental results found in Section 3.7.

The investigation also concluded that flow tone frequencies of the large-scale mode generally occur at the second mode and can be scaled with both pipe-diameter ($fD/U=\pi_1$) and cavity length ($fL/U=\pi_2$) for all values of cavity depths for which flow tones were generated regardless of whether or not large scale vortex formation is predicted. It would be interesting to see if the analogous WCR project can be scaled with internal cavity length or width. The nature of locked-on states was also investigated and the Q-factor was identified as a good indicator of the onset of locked-on flow tones. The Q-factor is an indication of the quality of the power spectrum, in this case of the pressure fluctuations, and can be seen as small amplitude “bumps” or much larger peaks that may represent robust locked-on states. A second indicator of the onset and degree of locked-on states was found to be represented by the ratio of the peak amplitude of the pressure spectrum

and the background pressure observed when flow tone coupling is not present. The analogy to this second indicator for the WCR system could be obtained from the ratio of hydrostatic pressure via wave height. Figure 9b of Rockwell and Naudascher [6] shows how the system can actually pull the frequency of the shear layer oscillations to match that of the cavity resonant modes. It would be interesting to observe the form of the shear layer across the cavity and the standing gravity wave in the cavity when this "pull" occurs and to determine similar indicators of a robust locked-on state for the WCR device.

In resonant systems, a net increase in the amplitude of the motion results due to the effect the shed vorticity has on the flow. In the case of vorticity produced by sound, viscous damping is significantly increased when the mean flow velocity is non-zero as compared to a system where the mean flow is zero [9]. In addition, when operating at high Reynolds numbers the viscous effects are only significant in the region close to the leading edge of the cavity where the vorticity is produced. The rate of dissipation of acoustic energy is seen to be negative when a coupled state exists wherein the shear layer oscillations are maintained by a feedback mechanism. This is the same mechanism discussed by Rockwell and Naudascher [6], Sobey [10], and many of the other papers that make up this literature review. However, Howe goes further to explain that the phase of the vorticity production is what results in the steady transfer of energy from the mean flow to the oscillations that make the oscillations self-sustaining. Detailed information is given regarding vorticity interactions with leading and trailing edges. The case of resonant coupling with vortex shedding is also discussed. An interesting conclusion is that only certain mean flow velocities will result in resonance because

sound can be absorbed in vorticity formation. Therefore, only certain mean flow velocities will result in phase relationships wherein the production mechanism is dominant in the system.

A pipe with closed side branches is investigated by Bruggeman et al and a model is presented for aero-acoustic sources that result in self-sustained pulsations of a low frequency [7]. The model approximates the magnitude of the pulsation amplitude along with and without friction and radiation losses. The paper outlines theory that predicts that downstream growth of perturbations at the leading edge will only occur when the Strouhal number is less than 0.04. The Strouhal number for the investigation was based on the initial shear layer momentum thickness. This is valid for low amplitudes and explains why only certain Strouhal number ranges will result in coupling with cavity resonances as observed by Rockwell (1979) and Rockwell and Naudascher [11]. An additional conclusion made by the authors is that sharp cavity edges are not required to generate large amplitudes and that making sharp edges round can actually reduce the amplitude of pulsations by a considerable amount.

Low frequency self-sustained pulsations in a coaxial gas pipe flow side-branch configuration with equal side branch lengths operating at low Mach numbers and high Reynolds numbers were investigated by Kriesels et al [12]. The main flow velocity and acoustic flow velocities are compared for configurations with sharp or rounded edges. The acoustic velocity is observed based on the path a shed vortex takes when travelling across the cavity entrance. A positive acoustic velocity is observed when the vortex goes into a side branch but this vortex can also impinge on the trailing edge of the cavity or escape the cavity altogether. Vortex paths were observed for the WCR that include

entrance to the cavity, impingement, and escape from the cavity while for non-resonant cases the vortex (of a small scale) path was largely impinging in nature with some cases in which escape occurred. A method for predicting source power based on the Strouhal number and acoustic amplitude is given and it is shown that the maximum pulsation amplitude can be predicted accurately by balancing source power with radiation and viscothermal losses in the system. For low velocities, however, the radiation losses can be neglected which suggests that for the WCR project only viscothermal losses need to be considered. However, as discussed in Section 3.3 since the hydraulic Froude number is indicative of compressibility of shallow flow water waves similar to the Mach number in air acoustic systems radiation cannot be ruled out. The non-linear relationship of acoustic power sources in terms of the velocity amplitude is observed to result in static pressure having a very large effect on pulsation amplitude.

Dequand et al investigate another closed side branch system where coupling between vortex shedding frequency and acoustic resonant modes is once again present [13]. A numerical method is developed for predicting the amplitude pulsations from the self-sustained flow oscillations that result and the method is found to predict amplitudes 30-40% higher than those experimentally observed. The numerical model neglects visco-thermal dampening and any vibrations that the walls of the system may undergo. Sharp cavity edges lead to a singularity in the numerical solution, thus rounded edges are used and result in an experimental error of 30%. A model is proposed for the WCR system that replaces the acoustic velocity term used by Dequand et al with the more involved relationship for water wave celerity but is left for future validation efforts. It is outlined and presented in Section 4.1 as a potential next step for the project.

Oshkai et al investigated acoustic power in a coaxial side branch resonator system with turbulent flow and low Mach number conditions to provide better characterization of acoustic noise-source based on shape and the effect of individual vortices [14]. The investigation was the first to combine global quantitative flow imaging with numerical simulation of the acoustic wave field and vortex sound theory. The shear layer transformation into large-scale vortical structures while undergoing downstream convection is captured in a vorticity field plot that demonstrates the effect of acoustic waves coupling with the shear layer. Shifting to lower acoustic modes is observed for narrow ducts and as the separation distance between the two side branches decreases the two independent sources join and become one source. In a similar way, for the parallel side branch system care was taken to ensure that the main channel width was large enough that the shear layer was not affected by the proximity of the parallel channel wall or cavity wall. This can be demonstrated in the flow images of the vector field obtained for the system. For a coaxial WCR design, care will need to be taken to ensure that the configuration has a sufficient separation distance between the side branches so that two independent sources will be present resulting in greater standing wave amplitudes.

Oshkai et al also note that for configurations with long side branches and at atmospheric pressures, viscothermal damping is very significant in terms of the acoustic response of the system and the observed amplitude of the pulsations. A similar problem may exist for either coaxial or parallel side branch WCR configurations with long cavity lengths.

An acoustic resonant system with fully-turbulent inflow and an axisymmetric cavity configuration was observed for acoustic wavelengths that are considerably larger

than the length of the cavity [15]. As cavity length is decreased, the oscillation mode is observed to change from being large-scale to small-scale and can be scaled based on the momentum thickness of the shear layer at separation. The conclusion drawn is that compatibility between the acoustic modes and oscillating shear layer hydrodynamic modes must exist but that the hydrodynamic modes may be distorted, or "pulled" by the system, to become compatible with the acoustic resonant modes of the system.

As discussed in Chapter 3 and Appendix C, incompatibility between higher hydrodynamic modes and WCR cavity modes was observed in most cases where n>2 (mode = n) as seen by travelling cavity waves. When incompatibilities did occur, cavity wave amplitudes were found to be less than 0.01 m peak-to-peak.

Oshkai et al observed that hydrodynamic modes of the oscillating shear layer exist even when an acoustic-resonant condition does not exist. Flow tones were only observed for even modes: a coaxial WCR design would need to have geometry capable of supporting resonance at the second mode.

Rockwell and Ekmekci [1] successfully coupled the first resonant cavity mode with an oscillating shear layer for a parallel side branch WCR configuration and in the thesis investigation the second mode was found to be the most favourable configuration in terms of system lock-on. One advantage of the parallel side branch configuration over the coaxial configuration is that odd modes can be excited while possibly changing the cavity boundary conditions.

For the acoustic resonant system a jump was also observed from higher to lower modes when the cavity length was varied for a configuration with widely spaced side branches. The spacing between the side branches of coaxial WCR configuration would

need to be kept sufficiently small to avoid a similar mode-jumping situation that may exist between the acoustic resonance and standing gravity wave resonance cases. However, it is also favourable to have a spacing that is large enough to support two independent shear layers to maximize power potential: a distinct advantage of this configuration over a design with a single shear layer as a power source for cavity wave excitation.

Oshkai and Yan investigated the interaction between separated shear layers of a deep cavity with a coaxial branch configuration coupled with acoustic modes [16]. Digital particle image velocimetry was used and results showed that if the distance between separation is wide enough the two shear layers will develop independently resulting in two independent sources of shear layer oscillations to excite resonance. However, after the separation width is reduced below a certain amount the two shear layers combine and act as a single power source. It was also observed that the acoustic-coupling with the second hydrodynamic mode was associated with a much lower acoustic power of a more complex form relative to the first hydrodynamic mode. Based on the conclusions of Oshkai and Yan the coaxial branch configuration design must ensure that the spacing width between the side branches is large enough to allow for two independent power sources for the resonant coupling with the standing gravity wave. This coaxial configuration may therefore be more effective than a single parallel side branch configuration under the same conditions assuming that the standing gravity wave-coupled system behaves in the same way as Oshkai and Yan observed the acoustically-coupled system to behave.

Tonon, Hirschberg, Golliard, and Ziada present a very detailed review paper summarizing the contributions related to flow induced pulsations in resonant pipe systems with closed branches [17]. Many of these are summarized above but there is also a great deal of other work, especially in relation to various configurations and series of side branches that is of interest.

1.5.3 Water wave mechanics and wave energy harvesting

Dean and Dalrymple compiled a textbook that gives an introduction to classical water wave theory for small amplitude waves (Airy wave theory) [18]. The text covers important sections on wave power calculation and wave maker theory that are also relevant to the design of wave absorbers. The excitation of the natural frequencies of standing gravity waves in natural and artificial basins, known as Seiching, is discussed and is very relevant to the WCR design. Seiching is of particular importance to the study as it provides the basic relationships to predict the wave frequency via the Merian formula. It also demonstrates that the phenomena of self-sustained oscillations of a free surface wave can occur on an immensely large-scale providing at the very least some insight into the possibility of up-scaling the WCR device.

Investigations were carried out by Hourigan on resonator tubes and energy transfer and absorption of a system undergoing resonant coupling [19]. Resonant feedback between a resonator tube and triangular trip rods in a shallow water tunnel was studied and it was found that for any inflow velocity the amplitude was dependant on the distance between the trip rod and resonator. It was found the amplitude in the resonator tube increased when changing the geometry of the trip rod by rounding the tips as this reduced damping

of the oscillations. A numerical study was conducted showing good agreement with the experimental results. The study is conducted in shallow water and aero-acoustic theory for low Mach numbers is applied to accurately predict the optimum trip rod-tube spacing; this very relevant to the shallow water flow regimes studied in this thesis. Beyond this, intermediate and deep water flows and the effect of coupling with an energy harvesting device was done in the investigation for this thesis.

1.6 Theory relevant to the analysis and design of cavity-wave resonators

Evaluation and analysis of the wave-cavity resonator with an ultimate goal of gaining insight into the viability of such a device for energy harvesting requires review of a range of fluid dynamics material. The primary mechanisms discussed include shear layer instabilities, water wave mechanics, and wave absorber theory. In addition, background theory around the various experimental and analysis techniques used in the investigations is also required but has been included in the appropriate experimental approach sections.

1.6.1 Oscillating flow

The characteristics of an oscillating flow mechanism can be described by a dimensionless quantity called the Strouhal number. It is described by Equation 1.1 given below:

$$St = \frac{fL}{V}. \tag{1.1}$$

In this equation f is the frequency of vortex shedding, L is the characteristic length, and V is the characteristic fluid velocity. In the case of the parallel side branch resonator design

that is the focus of this project, the characteristic length is equal to the cavity opening length L_{ec} shown in Figure 1.1 of Section 1.4.

The characteristic fluid velocity is that of the free stream velocity in the main channel (U_{∞}) and the vortex shedding frequency (f) is in relation to the flow separation region that is found between the leading and trailing edges of the cavity opening length denoted as L_{ec}.

The vortices that are created by the separating shear layer can interact with the downstream edge of the cavity entrance in a number of ways. In some cases the vortex completely escapes the cavity while in other cases it impinges on the trailing edge or becomes fully enveloped by the cavity as seen in Figure 1.2 [6]. The type of impingement can have a considerable effect on how much energy is transferred to the fluctuating shear layer and the formation of subsequent vortices in the system but is not necessary for feedback.

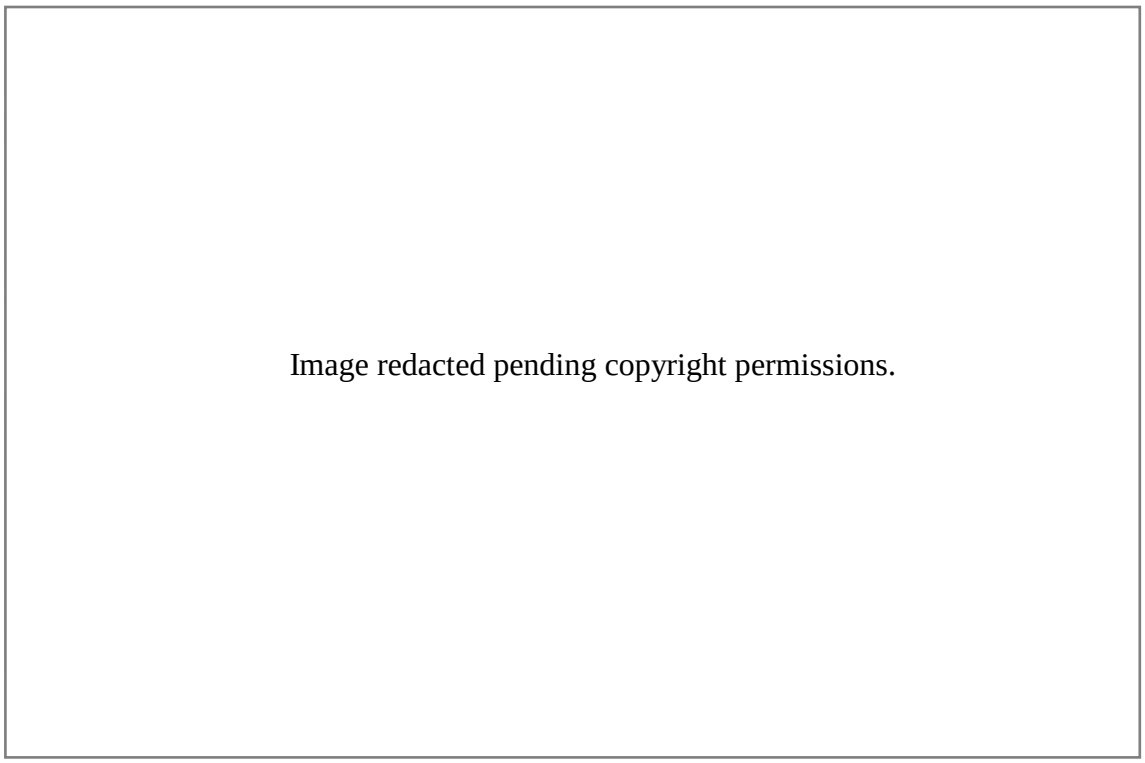

Figure 1.2 Vortex-impingement interaction from Rockwell and Naudascher [6].

When a vortex impinges upon the trailing edge of cavity system variations of pressure can be introduced into the system as discussed by Rockwell and Naudascher [6]. This impingement is not a necessary condition as feedback that allows self-sustained oscillations of the shear layer can also occur for systems for which edge impingement does not occur [20]. For example, when the vortex enters the cavity directly without impingement and disturbs the pressure field or even through velocity induction due to the vortex [21]. The necessary condition is that the potential field must have an interaction with the shear layer as seen as a response by the field. A positive acoustic velocity was observed by Kriesels et al when the vortex was encompassed by the cavity. A typical vortex path can be seen in the result of the investigation by Kriesels et al in Figure 1.3 [12].

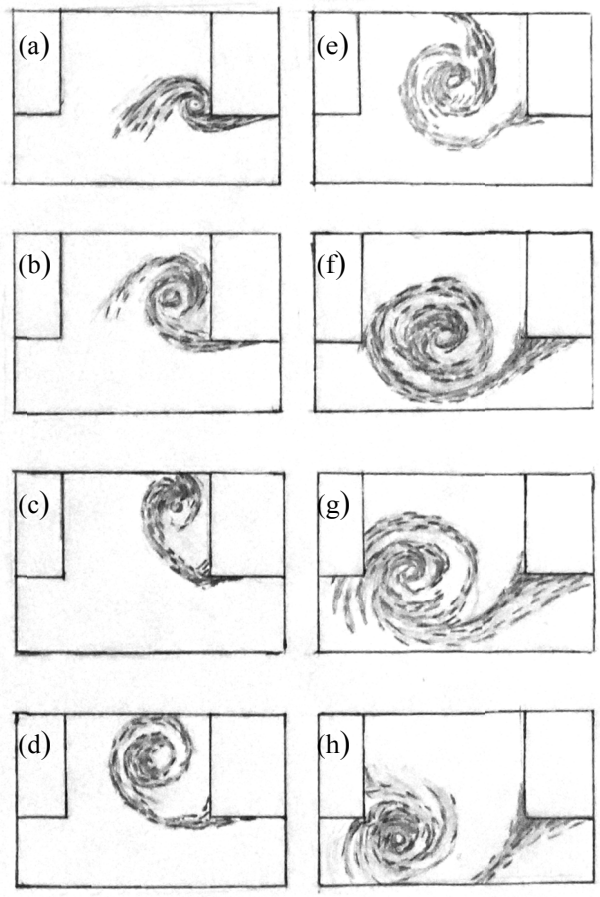

Alyssa Reaume

Figure 1.3 Vortex layer path in cavity.

Acoustic velocity is defined by the wavelength and frequency of an acoustic wave and corresponds to the longitudinal velocity of the wave particles about their initial positions. In the hydrodynamic system of the WCR the wave particle celerity, that is the i-component of particle velocity, is analogous to the acoustic velocity.

It is helpful if the hydrodynamic oscillations of the cavity are analyzed first before gravity wave oscillations are considered. These hydrodynamic oscillations resulting from fluctuations in the separating shear layer can be attributed to organized unsteadiness of velocity and vorticity fields along the cavity opening. In order for the hydrodynamic oscillations to be self-sustaining four essential features are proposed by [6] in the system.

The first of these is that there must be one or more incident vorticity concentrations at the trailing edge of the cavity. Secondly, the sensitive shear layer region that formed at the leading edge of the cavity must be influenced by the downstream vorticity distortion that occurs at the trailing edge. The next feature is that this disturbance that influences the sensitive shear layer region at the leading edge of the cavity is converted to a fluctuation in the separating shear layer. Finally, this fluctuation in the separating shear layer is amplified as the separating shear layer grows downstream [8]. From fluid mechanics, this fourth feature will occur during flow separation to satisfy the conservation of mass principle. This flow mechanism is discussed further in terms of feedback mechanisms in Section 1.6.3. The first of these proposed features, the interaction with the trailing edge of the cavity, is not a necessary condition of the feedback mechanism as later shown by Tonon et al. [20]. Vortex-induced velocity and perturbations to the pressure field without trailing edge interactions are sufficient [21] including free surface fluctuations. In any case, the instability-induced excitation (IIE) mechanism present in the resonant coupling is the dominant mechanism and receives feedback from the excited cavity wave.

1.6.2 Strouhal number regimes

Strouhal numbers with an order of magnitude of unity indicate that the fluid particles will move as an oscillating fluid plug resulting from the dominating viscous effects: inertial separation will never occur even for high Reynolds numbers [10]. For Strouhal numbers of the order of 10^{-4} and below, the quasi-steady state portion (velocity) of the flow dominates the oscillation. In fluid systems characterized by $10^{-4} < S_r < 1$ build-up and then rapid shedding of vortices will be observed [10]. Based on this insight it would be expected that in order for shear layer oscillations to occur in the WCR system, the flow

conditions must be such that the Reynolds number is high enough for separation to occur and the Strouhal number is in the intermediate range ($10^{-4} < S_r < 1$).

1.6.3 Feedback control and flow mechanisms [22]

For flow instabilities in viscous fluids, energy from the mean stream flow is transferred by mechanisms causing flow fluctuations. This transfer of energy is dependent on both the geometry of the system and the disturbance frequency. The disturbances are amplified only if they occur within a range of frequencies for flows in which the Reynolds number is above a critical value. This is related to stability theory that shows that for a particular set of inflow conditions different rates of amplification will occur to the fluctuating components (with fluctuations occurring at various fixed frequencies) of the flow as they are carried downstream. It follows that below a threshold Reynolds number no amplification occurs for the frequency ranges of the fluctuating components of the flow that are present. This amplification by energy transfer to the disturbances causes the flow to fluctuate in a somewhat periodic manner but will not result in oscillatory flow without the effect of feedback mechanisms. The feedback control mechanism can be described as being fluid-elastic, fluid-dynamic, or fluid resonant.

In fluid-dynamic feedback control, the fluctuating flow leads to flow-boundary interactions that control the fluctuating flow. If this flow-boundary interaction interacts with a resonating body oscillator, fluid-elastic feedback control will control the fluctuating flow. Finally, if the flow-boundary interaction occurs with a resonating fluid oscillator, fluid resonant feedback control is said to control the feedback flow [22]. Periodic disturbances and random disturbances can also cause flow instabilities and drive

fluctuating flow. This type of control is referred to as extraneous control but is not applicable to the WCR system unless the wave absorber is used to drive the SGW.

The case of feedback control that is most relevant to this project is that of fluid-dynamic feedback from instability-induced excitation (IIE) with a trailing edge impingement or vortex path exciting a fluid oscillator. In a system with rotational fluctuating flow natural feedback is inherent to the system. However, if a point of impingement is present at the trailing edge of the free shear layer, or in the revised view of Tonon et al. [20] if any interaction between the shear layer and resonant mode causes coupling, pressure perturbations in a fluid-dynamic feedback mechanism will be present that are much larger than those of the natural pressure perturbations. These pressure perturbations are created for example, when vortices impinge on the trailing edge of the cavity as already discussed in Section 1.6.1, when the vortex enters the cavity, or even when a large scale vortical structure travels along the cavity opening length causing pressure perturbations or inducing velocity [21]. When these pressure perturbations reach the separation region where the new vortices are formed, new flow fluctuations occur and are subsequently amplified by downstream expansion. The fluctuations occur because the separation region is very sensitive to flow disturbances. When these fluctuations reach the downstream region where the interaction occurred greater pressure perturbations are produced that propagate upstream and the process continues. When the feedback mechanism is successful the system is said to have self-sustained shear layer oscillations. This will only occur if the new flow fluctuations produced by the pressure perturbations from the interaction region are in phase with the flow fluctuations produced at the separation region and certain amplification conditions are met. At start-up it was

observed that the primary mechanism was interaction between small scale vortical structures impinging on the trailing edge of the cavity.

In this case the impingement region is referred to as the flow-boundary interaction and an integer number of vortices corresponding to the hydrodynamic mode must be able to fit in the cavity gap. However, in real systems a non-integer fraction of wavelengths can also exist in the gap in which case shear layer oscillations will still be observed. Radiation considerations can be neglected for flows in which the convective velocity is much less than the speed of sound for acoustically coupled systems. As shown in Chapter 3 for the WCR system wave celerity, Froude number, and convective velocity must be considered in order to predict the behaviour of the system accurately.

Likewise, a free surface system can act as a resonating fluid oscillator and can provide fluid-resonant feedback control to the flow fluctuations present. In the case of this project the fluid-dynamic and fluid-resonant feedback mechanisms may both be present and can compete for control of the feedback system. Overall, the mechanism that dominates will meet the phase condition best, have the most direct interaction with the sensitive separation region at the leading edge of the cavity, and will thus transfer the most energy from to the oscillating flow from the mean flow. It is important to note that when two oscillators are coupled a hybrid feedback mechanism can be present having unique system characteristics.

1.6.4 Boundary layer considerations

Based on flow-induced vibrations theory, a number of design considerations must be made in order to generate one of the hydrodynamic modes of the separating shear layer.

According to Naudascher and Rockwell [22] and Sarohia [23], experimental evidence has been collected for 2D cavities under turbulent boundary layer conditions. This non-dimensionalized data can be used to predict what Strouhal numbers and corresponding hydrodynamic modes will exist in terms of cavity length L_{ec} and the cavity critical length W_c or L_c. Based on the design solution obtained for the WCR from a preliminary optimisation, the cavity opening length and width were determined to be L_{ec}=0.294 m and W_c=0.125 m respectively. The Strouhal number corresponding to peak pressure fluctuations for this geometry can be estimated from the data in Figure 1.4 [22]. The result obtained gives a Strouhal number of approximately 0.5 and corresponds to the 1st hydrodynamic mode.

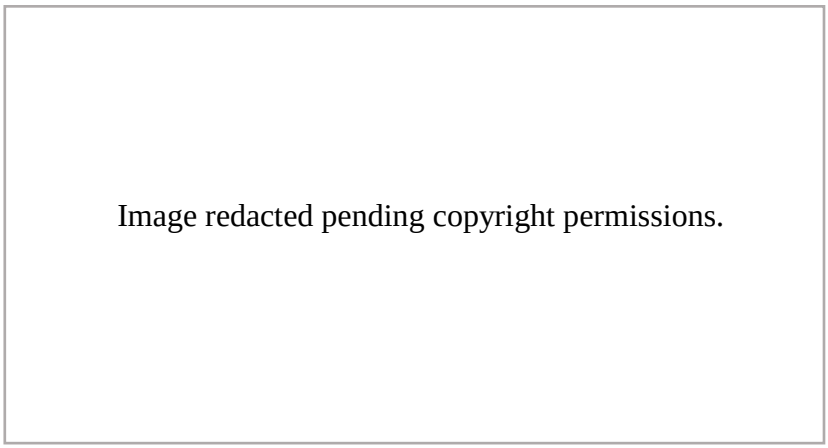

Figure 1.4: Strouhal number as a function of cavity width, gap length, and hydrodynamic mode from Ethembabaoglu [24], [25].

The data of Figure 1.4 is valid for a 2D cavity having turbulent boundary layer conditions at separation and is taken from Figure 6.25 [22] from Ethembaboaglu. Since the Strouhal number is defined as $S_t = \frac{fL_{ec}}{V}$ this corresponds to a frequency of 2.548Hz.

However, for the cavity length geometry L_c=0.5 m of the design solution, the frequency of the corresponding standing gravity wave is only 1.58 Hz. In order to match

the shear layer oscillation frequency, L_c must be changed to approximately 0.31 m which is within the adjustable range for the WCR system. With these dimensions the standing gravity wave may propagate out into the main channel as there would not be a significant fixed cavity wall to contain it with this geometry. This was indeed observed during preliminary testing leading to the decision to extend cavity length to L_c=0.622 m to reduce the influence and energy losses of wave radiation.

Using the Strouhal number corresponding to the first hydrodynamic mode reported by Rockwell and Ekmekci for a parallel side branch WCR of St=0.32, a shear layer oscillation frequency of 1.63 Hz is expected at a free-stream velocity of 1.5 m/s [1]. In order to meet the expected Strouhal number for the first hydrodynamic mode and match the frequency of the standing gravity wave of 1.58 Hz a free stream velocity of 0.93 m/s would be required. The design allows both of these free-stream velocities to be easily obtained to increase the likelihood of resonant coupling.

The relationship between cavity opening length (L_{ec}) and boundary layer thickness (δ) also determines what Strouhal numbers will be present at a given hydrodynamic mode. According to Figure 1.5 from Sarohia [22], for a 2D cavity the first hydrodynamic mode will occur for approximately $0.6 \leq St \leq 0.8$ and $6 \leq L_{ec}/\delta A \leq 10$ for a fully-turbulent boundary layer and $V\delta/\nu = 2860$. For the operating conditions of V=1.5 m/s and $\mu = 8.91E^{-4}$ kg/m.s and ρ=997 kg/m^3 (water at 298 K) the boundary layer thickness is approximately 1.91 mm and for V=0.93 m/s the boundary layer thickness is approximately 3.10 mm based on flat plate theory. With final inflow conditions the boundary layer ranged from 8.5 mm to 20 mm at 0.27 m/s and 1.1 m/s respectively.

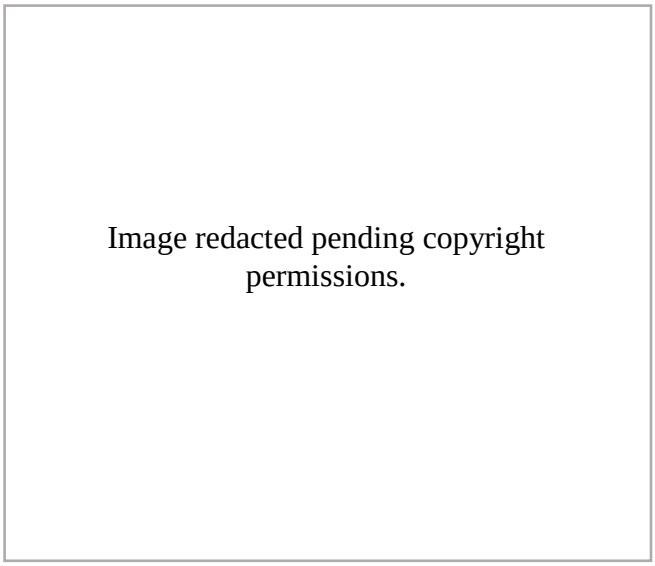

Figure 1.5 Strouhal number as a function of hydrodynamic mode and Lec/δ from Sarohia [22].

Because the WCR system differs from the 2D geometry, is an open channel, and the boundary layer is turbulent, additional work will be required to determine whether or not the configuration will have a similar boundary layer thickness at the corresponding free-stream velocities. The boundary layer will be turbulent for free-stream velocities greater than 0.5 m/s for an entrance length of 1 m using the critical Reynolds number for a flat plate of $5E^5$. Since most of the current data is available only for fully-turbulent boundary layers the WCR should be operated above a free stream velocity of 0.5 m/s to ensure that the system parameters required to generate a given hydrodynamic mode can be predicted. However, this was not an issue with the operation of the actual WCR system as resonant effects were observed for inflow velocities below this value.

1.6.5 Shear layer frequency estimation

A number of models to predict the fundamental frequencies of the hydrodynamic mode have been proposed for various conditions. This is necessary since the Strouhal number

cannot be obtained apriori. While there is some insight into what range the Strouhal number must be within in order for resonance to occur such as Bruggeman et al predicting St≤0.04 for an acoustic coaxial system [7] and in the experimental results presented in the boundary layer discussion. These models all relate the inflow velocity to the convective velocity of the shed vortices and wave mode using parameters obtained by fitting to experimental data. Since the performance and modification of these prediction models from acoustically analogous systems are discussed in detail in Section 3.3 they are presented here without remark from Equation 1.2 [22], Equation 1.3 and Equation 1.4 [26]:

$$f = 0.52U_{\infty}(n - 0.25)/L_{ec}. \tag{1.2}$$

$$f_o = \frac{U_{\infty}}{U_c}(1 - c). \tag{1.3}$$

$$f = U_{\infty}\,(\mathrm{n} - \Upsilon)/(\mathrm{L_c}(1/\mathrm{K} + \mathrm{Ma})). \tag{1.4}$$

Equation 1.2 and 1.3 fail to predict the hydrodynamic frequency of the system over the range of depths and velocities present since they do not account for the free surface flow regime and associated feedback celerity of the cavity wave.

1.6.6 Shallow, intermediate, and deep water wave theory

The linearized frictionless wave equation for a horizontal bottom geometry is given by:

$$gh\left(\frac{\delta^2\eta}{\delta x^2} + \frac{\delta^2\eta}{\delta y^2}\right) = \frac{\delta^2\eta}{\delta t^2}. \tag{1.5}$$

In the above equation η represents the free surface position, g the gravitational constant, and h the water depth [18]. A solution to the wave equation modelling a standing wave is given as:

$$\eta = \left(\frac{H}{2}\right)\cos\sigma t \cos kx, \tag{1.6}$$

where H represents the peak to peak amplitude (wave height) of the wave, k the wavenumber, and σ the angular frequency of the wave. Nodes and antinodes form on standing waves as waves reflect on themselves leading to points of zero and maximum free surface height variation. The Airy model assumes incompressible, inviscid, irrotational flow and accurately describes the wave kinematics for small H/λ (deep) and H/h (shallow) and in addition can be used as a starting point for second order models such as wave energy density.

Closed-closed boundary conditions:

Since a boundary is formed at either longitudinal end of the cavity due to the cavity walls at the leading and trailing edges of the cavity the wave velocity in the horizontal direction (normal to the wall) must be zero at these locations. For a closed end condition, such as a rigid cavity wall, the incident wave is positively reflected. With the maximum longitudinal pressure variations, that is antinodes, occurring at these locations where $x = 0, L_c$ the solution to satisfy η(x,t) involves the boundary conditions $\sin kx = 0$ for $x = 0, L_c$ for which $kl = n\pi$ must be satisfied [18]. The number of nodes is represented by n and the wavelength λ can be determined by:

$$\lambda = \frac{2L_c}{n}. \tag{1.7}$$

Closed-open boundary conditions:

As will be addressed in the discussion, the commonly excited modes of the system occurred between the rigid wall at the trailing edge of the cavity and the pressure expansion occurring across the opening of the cavity. At this open boundary, longitudinal pressure must meet that of the surrounding medium that acts as a reservoir and is hydrostatic. At open boundaries the wave is negatively reflected and a node forms at this location which is largely affected by the added mass of the surrounding medium. For this closed-open boundary configuration the wavelength can be determined by:

$$\lambda = \frac{4L_c}{2n-1}. \tag{1.8}$$

However, as will be shown in the discussion the above formulas do not accurately predict the wavelengths for either case: the effects of added mass must also be accounted for. This can be partially accounted for by replacing L_c with L_{eff} obtained from a modified version of Altser's results given below without modification [27]:

$$L_{c,eff} = \left(1 + 0.48\frac{D}{L_c}\right)^{0.5}. \tag{1.9}$$

This result was obtained for the fundamental aero-acoustic mode of a circular duct with closed-open boundary conditions. While this result worked well with closed-open longitudinal cavity wave modes, closed-closed longitudinal modes were best predicted with $L_{c,eff} = L_c - L_{ec}$ and closed-closed lateral modes with $L_c = W_c$ as will be discussed.

The wave number k is the spatial frequency of the wave and can refer to units of [cycles/distance] or [radians/distance]. The angular, or circular, wave number given by radians per distance is expressed as $k = 2\pi/\lambda$. The dispersion relation describes the dependence of the wave number on the frequency. Since the angular frequency ω is given

by $\omega = 2\pi f$ the wave number can be expressed simply as $k = \frac{\omega}{c_{phase}}$ where c_{phase} is the phase velocity, or celerity, of the wave and is dependent on the water depth and the wavelength:

$$k = \frac{2\pi}{\lambda} = \frac{2\pi f}{c_{phase}} = \frac{\omega}{c_{phase}} . \tag{1.10}$$

Shallow water waves:

Shallow water waves, also known as long waves, are defined for conditions such that the depth h is less than half the wavelength or:

$$\frac{h}{\lambda} < 0.05 . \tag{1.11}$$

For a given frequency component of a wave, the phase velocity is the velocity at which the phase of this component travels. Shallow waves are unique in that they show no frequency dispersion, meaning that phase speed is independent of the wavelength. The wave celerity c is not proportional to the wavelength and can be expressed simply as the square root of the product of the depth and acceleration due to gravity:

$$c \cong \sqrt{gh} . \tag{1.12}$$

This approximation of the wave celerity is obtained from the linearized wave equation (Airy solution) of Equation 1.5 using the shallow water wave condition as previously given. The Merian formula given below in Equation 1.13 can be used to predict the standing gravity wave period for shallow water waves.

$$T = \frac{2L_c}{n\sqrt{gh}} . \tag{1.13}$$

The Merian formula is obtained from a simplification of the linearized wave equation that does not affect the results for shallow wave conditions and is derived from the resultant dispersion relation. The dispersion relation for shallow water waves is given by:

$$\Omega(k) = k\sqrt{gh} = \frac{2\pi}{\lambda}\sqrt{gh}. \quad (1.14)$$

When combined with the result for wavelength λ previously given and equating the result to the angular frequency we can obtain the Merian equation for closed-closed boundary conditions:

$$\Omega(k) = \frac{2\pi n}{2L_c}\sqrt{gh} = \omega = \frac{2\pi}{T} \rightarrow T = \frac{2L_c}{n\sqrt{gh}}. \quad (1.15)$$

Similarly, a closed-open boundary condition solution is obtained as:

$$\Omega(k) = \frac{\pi(n-0.5)}{2L_c}\sqrt{gh} = \omega = \frac{2\pi}{T} \rightarrow T = \frac{4L_c}{(n-1)\sqrt{gh}}. \quad (1.16)$$

Rockwell and Ekmekci have conducted investigations of the resonant coupling of shallow standing gravity waves and oscillating shear layers developing across the entrance of cavity flows and have observed the development of large scale vortical structures in the presence of a resonating flow for the closed-closed condition [1].

Deep water waves:

Deep water waves, also known as short waves, show frequency dispersion since the wave celerity is proportional to the wavelength. These deep water waves are found for conditions in which the depth is much greater than the half-wavelength or:

$$\frac{h}{\lambda} > 0.5\ . \quad (1.17)$$

Using the deep wave dispersion relation, again a simplification of Airy's solution, a result can be obtained for the wave period as follows. The dispersion relation is given by:

$$\Omega(k) = \sqrt{gk} = \sqrt{\frac{2\pi g}{\lambda}}\ . \quad (1.18)$$

Equating the dispersion relation with the angular frequency ω gives:

$$\omega = \frac{2\pi}{T} \rightarrow T = \frac{2\pi}{\sqrt{\frac{2\pi g}{\lambda}}} = 1/\sqrt{\frac{g}{2\pi\lambda}}. \tag{1.19}$$

The phase velocity c_p is given by $\sqrt{\frac{g}{k}}$ and wavelength λ by $\frac{gT^2}{2\pi}$.

Intermediate Water Waves:

For cases where 0.5> h/λ >0.05 the water wave is classified as having an intermediate depth and the dispersion relation is given by:

$$\Omega(k) = \sqrt{g\frac{2\pi}{\lambda}\tanh\frac{2\pi}{\lambda}h}, \tag{1.20}$$

where the phase velocity c_p is given by:

$$c_p = \sqrt{(\frac{g}{k})\tanh(kh)}. \tag{1.21}$$

The wavelength can be obtained by the solution to equating the dispersion relation with angular frequency for the given period after substituting for wave number k.

$$(\frac{2\pi}{T})^2 = \frac{2\pi g}{\lambda}\tanh\frac{2\pi h}{\lambda}. \tag{1.22}$$

Conversely, for a given possible wavelength the period and thus frequency of the cavity wave can be determined. For the closed-closed boundary condition this results in:

$$T = \frac{2L_{c,eff}}{n\sqrt{g\frac{2L_{c,eff}}{n\pi}\tanh\frac{n\pi}{L_{c,eff}}h}}. \tag{1.23}$$

Details of the derivation of shallow, deep, and intermediate waves are given in Appendix A and these expressions are based on Airy's solution which neglects surface tension (valid for width of cavity used in investigation) and are valid only for small wave amplitudes [22]. Work was completed by Rouse (1938) to account for non-linearities associated with large amplitudes for the shallow and deep-water wave equations respectively [28]:

$$c \cong \sqrt{gh}\left[1+\frac{3H}{2h}\right]^{0.5}. \quad (1.24)$$

$$c \cong \sqrt{\frac{g\lambda}{2\pi}}\left[1+\left(\frac{2\pi H}{\lambda}\right)^{2}\right]^{0.5}. \quad (1.25)$$

Wave frequency increases with wave amplitude under the conditions of interest to the experimental investigation but as can be seen in the discussion this correction did not fully account for the increase in measured cavity wave frequency with increasing inflow velocity. The frequency shift with wave amplitude does however provide a possible explanation to hysteresis seen in the system as addressed in the discussion.

1.6.7 Wave maker theory

For constant depth and shallow water the volume of water displaced by the wave maker is equal to the volume of water in the crest of the wave that will form as a reaction to the motion of the wave maker [29]. For a given wave, the volume of water in the crest can be obtained by integrating the representative periodic function over half of the wavelength:

$$V_{crest} = \int_0^{\lambda/2} \frac{H}{2} \sin kx \, dx \, . \quad (1.26)$$

A piston wave maker was selected due to the availability of an adequately powerful linear table and load cell configuration used in preliminary testing of the system. Additionally, in shallow water conditions piston-type wave makers are more efficient than their paddle-type counterparts and since resonant coupling was expected to break down in deep water conditions the piston-type would be most appropriate [18]. However, in deep water the paddle-type is more efficient as can be seen by plotting equations for the linear range of $k_p h$ corresponding to approximately $k_p h = 2$ for flap-type and $k_p h = 1.25$ for piston-type

wave makers [18]. The result as seen in Figure 1.6 is that a lower piston stroke is required to generate a given wave amplitude for the same shallow conditions of a flap-type wave maker.

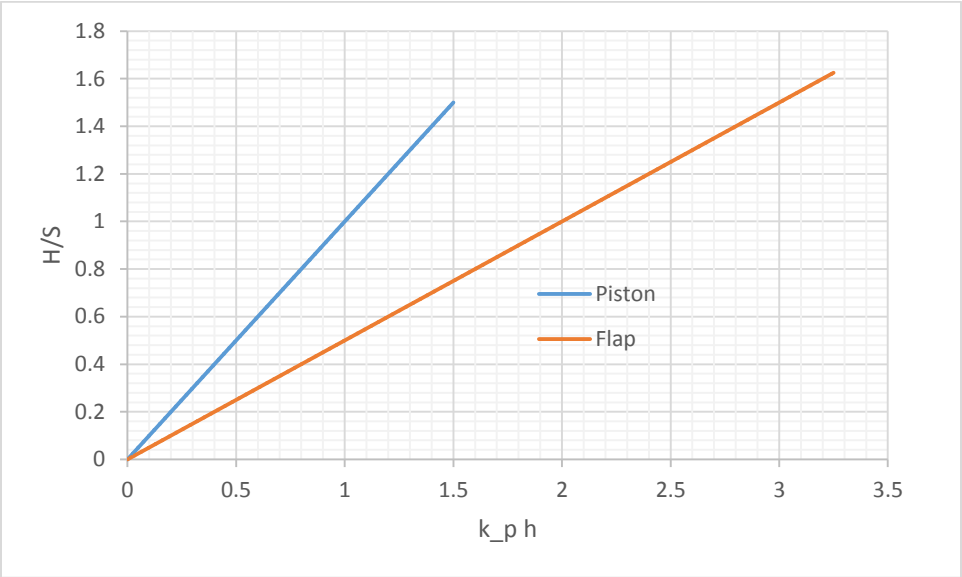

Figure 1.6: Height-to-stroke ratio for piston and flap type wave makers.

Assuming constant depth, the volume of water displaced V_d by a stroke S of the piston can be determined by:

$$V_d = Sh\,. \tag{1.27}$$

This gives that $\frac{H}{k} = Sh$ and with $k = \frac{2\pi}{\lambda}$ we obtain $Sh = \frac{H\lambda}{2\pi}$ to generate a given wave. For a given wave height, wavelength, and water depth the stroke required by the wave maker is given by:

$$S = \frac{H\lambda}{2\pi h}\,. \tag{1.28}$$

The relationship in Equation 1.28 is valid for shallow water where *kh<pi/10*. A more general relationship is given by:

$$S = \frac{H\sinh(2k_p h) + 2k_p h}{2(\cosh(2k_p h) - 1)}. \quad (1.29)$$

As will be discussed, resonant coupling does not inherently break down at deeper depths; however, a given cavity frequency approaches a maximum value at increasing depths and may not couple with higher hydrodynamic modes and increasing hydrodynamic frequency thus limiting the inflow velocity range for which resonant coupling could occur. Despite the occurrence of resonance for increasing depth, the wave absorber model remains in the approximately linear range for the tests conducted. The above model also makes a poor prediction, as shown in the data, of the generated wave due to the large expansion to the main channel present along the cavity opening and added mass characteristics of tangential and mean flow past the cavity.

1.6.8 Wave power calculation

The wave energy flux in units of [power/unit width] of a given wave can be determined from the relationship:

$$P = Ec_g, \quad (1.30)$$

where c_g is the group velocity of the wave, dependant of the depth classification of the wave, and E is the mean wave energy density (per unit of horizontal area [J/m^2]) given by the relationship in Equation 1.31 [30]:

$$E = \frac{1}{8}\rho g H_{SWH}^2 . \quad (1.31)$$

In this equation H_{SWH}^2 is the significant wave height and is determined by $4\sigma_\eta$ where σ_η represents the standard deviation of the peak surface elevation distribution.

The group velocity for each classification of water wave depth and the associated mean wave energy density relations are summarized in Table 1.1 below.

Table 1.1: Group velocities and wave energy flux by depth classification.

	Shallow Water Wave	Intermediate Water Wave	Deep Water Wave
Group Velocity c_g	$\sqrt{gh}$	$\frac{1}{2}\sqrt{\frac{g}{k}\tanh kh} * \left(1 + \frac{2kh}{\sinh 2kh}\right)$	$\frac{gT}{4\pi}$
Wave Energy Flux [W/m]	$\frac{1}{16}\rho g H_{SWH}^2 \sqrt{gh}$	$\frac{1}{32}\rho g H_{SWH}^2 \sqrt{\frac{g}{k}\tanh kh} * \left(1 + \frac{2kh}{\sinh 2kh}\right)$	$\frac{T}{64\pi}\rho g^2 H_{SWH}^2$
Standing Wave Energy [J/m] per crest width for one wavelength: ($H_{standing} = 2H_{prog}$) $E = \frac{\rho g (\frac{H}{2})^2 \lambda}{4}$			

For the case of the wave cavity resonator, conditions for which resonant coupling occurred were associated with wave amplitudes with low standard deviation. Non-locked-on cases were characterized by cycles of increasing followed by decaying wave amplitudes. From an energy conversion standpoint however, only the locked-on cases are of interest. Some locked-on configurations were associated with both lateral and longitudinal modes and thus had regular varying amplitude as did the cases where a cavity mode was coupled with an alternating 1^{st}-2^{nd} hydrodynamic mode. These two cases are the primary purpose of using the significant wave height. Energy harvesting under these two conditions would not be trivial due to the additional coupling of the system with the wave absorbing device. Progressive wave power calculations have been used to give an indication of relative power but actual wave absorber energy extraction would occur due to piston-wave interaction and hydrostatic effects and would be associated with much lower power. An array of cavities operating in phase and arranged

so that an adjacent cavity wave forms on the reverse side of the piston would lead to a significant free surface height difference and associated hydrostatic pressure difference across the piston.

The discussion within Chapter 2 gives an overview of experimental techniques employed and the construction and features of the wave cavity resonator apparatus itself.

2 Experimental System and Techniques

2.1 Experimental apparatus: Wave cavity resonator

While various configurations of side branches are possible for systems undergoing resonant coupling between shear layers and cavities a parallel side branch design was selected. Using theory for a shallow system and the experimentally obtained Strouhal number of St = 0.32 [1] an iterative optimization was completed for both a parallel and coaxial design. Constraints for this optimization were based on the operational and geometrical parameters of the flow facility. In addition, since the investigations are experimental in nature it is necessary to use a design that facilitates changing parameters; the parallel side branch design was most suited to adjusting cavity lengths and entrance widths.

2.1.1 Design layout

The wave-cavity resonator layout can be seen in the following assembly figures along with labeled features and components commonly referred to in this thesis. Details of the wave absorber are provided within Section 2.4.6 for which the wave absorber design is the focus. General system parameter definitions can be referenced in Figure 1.1 where they were presented in Section 1.4 along with the relevant theory.

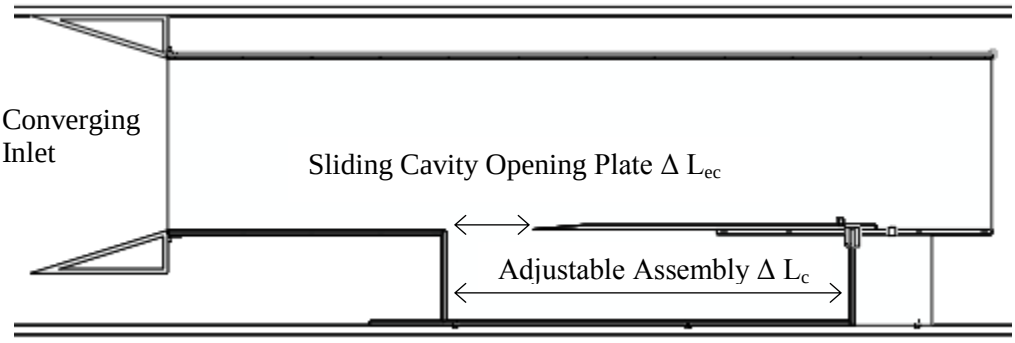

Figure 2.1: WCR component definitions and locations.

The converging velocity inserts used to tune the free stream velocity profile along with the sliding cavity opening plate, sliding cavity length plate, and other components can be seen in Figure 2.1 above. After initial testing it became apparent that the geometry of the converging velocity inserts as shown was too abrupt and resulted in flow separation. In addition, the inflow section itself was too short to allow adequate boundary layer growth upstream of the cavity. The inflow region was completely redesigned to include an elliptical convergent section to smooth the flow, a bottom plate, and an extended inlet section. The inlet section was constructed of a thin acrylic sheet heat formed to three ribs per side similar to the construction of an airfoil. The base plate was bolted along the outside of the lowest rib and the entire section was fused to thick 12.7 mm acrylic plates that acted as flanges for rigid attachment to the main apparatus. An upper support brace was also slotted and attached to the top of the inflow section to ensure rigidity. A secondary function of this brace was to allow tuning of the inlet section to ensure proper geometrical alignment. The finished section is shown in Figure 2.2 below along with the wave absorber configuration.

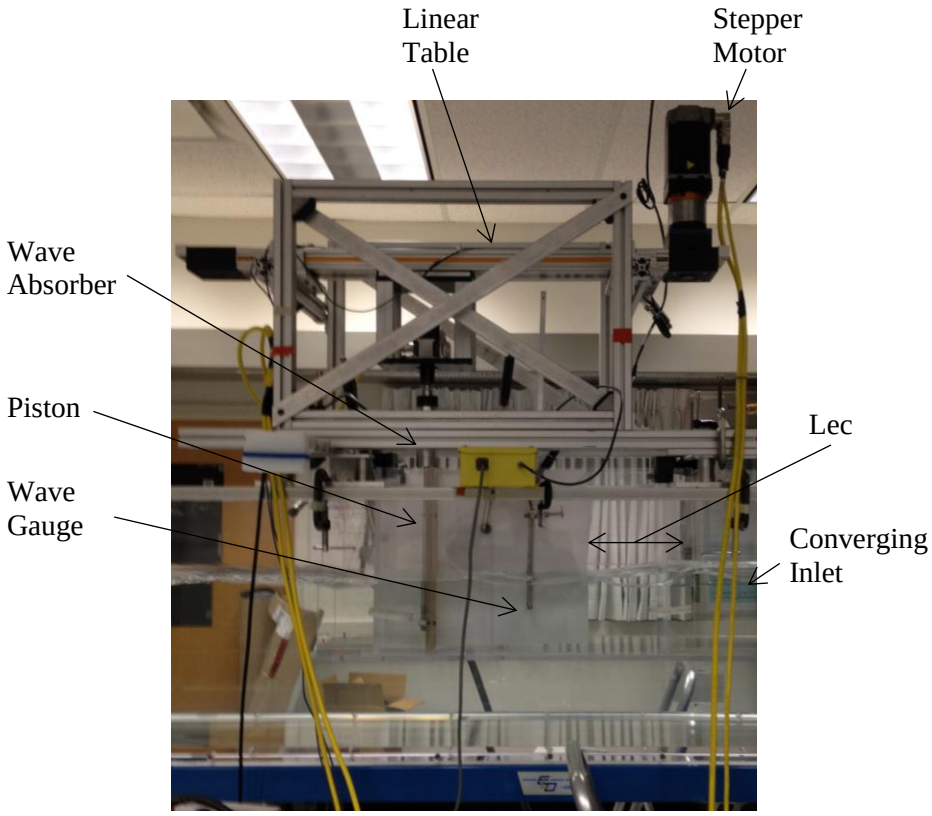

Figure 2.2: Experimental setup including wave absorber.

In the main section of the apparatus, brackets were used to support and locate the WCR components and allow for multiple geometric combinations. Threaded depth control cylinder mounts and the plates on top of the water tunnel were part of the initial design but were later replaced with shimming blocks on the main support beams to improve ease of use. As discussed in Section 1.6.4, a sufficient main channel length is present to allow the flow to become fully turbulent and developed before the leading edge of the cavity gap is reached. As can be seen in Figure 2.1, the camera view window for the PIV procedure is generally unobstructed and the acrylic sheets are continuous in this region to avoid erroneous intensity peaks that could be caused by internal reflections and introduce errors during correlation of intensity peaks between image pairs during data processing. The side of the WCR insert facing the laser is also continuous and unobstructed to allow for successful PIV investigations. Nevertheless, during a laser triggering-software error

the surface was reflective enough to burn the author's cornea and pigment layers of the retina.

2.2 Design features of selected configuration

The actual flow conditions resulting in resonant lock-on between shear layer oscillations were initially unknown. The system was therefore designed using theory and results from similar experiments and from analogous aero-acoustic theory. It was necessary to design the system to be flexible in terms of both geometric layout and flow conditions in order to find the optimum configuration. A number of features have been implemented in the design to address this system flexibility requirement. The material used for the walls and base plate is acrylic polymer and the parts were fixed using a welding process or stainless fasteners and threaded holes at spacing intervals of 0.15 m. Various brackets made of Delrin and aluminum were used to secure movable components. In addition, series of clamps and rods were installed to provide extra rigidity to adjustable walls since the bases of these movable plates could not be welded to the base plate. The cavity width W_c = 0.125 m corresponds to the lateral flow facility space remaining if a distance of $>2L_{ec}$ is left to ensure that the vortex does not interact with the opposite solid wall [14].

2.2.1 Sliding cavity gap plate

The plate that determines the cavity opening length (L_{ec}) is capable of being adjusted for a range of gaps from 0 to 0.3935 m. This is accomplished by using a “T-bracket” clamp to secure the top of the slider plate to the fixed cavity wall that determines the maximum value for L_{ec}. An “L-bracket” was initially used to locate and secure the base of the slider plate to the base of the main channel. Despite being designed with a low profile it was found to interfere with the main channel flow. Furthermore, even though this bracket was constructed from a transparent material to avoid blocking the viewing window of the high speed camera distortion of the flow field image occurred. Figure 2.3 demonstrates how

the sliding cavity gap plate and sliding cavity length plate can be used to provide different cavity and shear layer parameters without major modification.

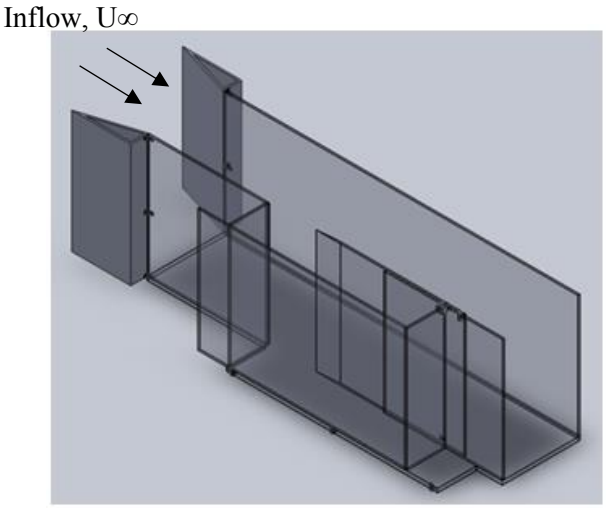

Figure 2.3: Schematic of multiple geometry configurations possible with WCR insert.

The sliding cavity opening plate was designed with a tapered leading edge to eliminate the effect that impingement geometry has on the formation of vortices as observed by Rockwell and Naudascher [6]. However, as discussed in Section 1.5.2 manufacturing of such geometry was not possible within a reasonable time frame and preliminary data was collected with the standard impingement geometry used for the entire investigation for consistency.

2.2.2 Cavity depth control

The nominal water depth is the same for the main channel and the cavity and can be adjusted by shimming the plates that are used to locate and the WCR insert support beams on the top mounting area of the water tunnel. In addition, the water tunnel can operate between depths of 0.25 m and 0.45 m and can also be used to control the nominal depth in the WCR. The effect of varying the depth of the water tunnel on the inflow velocity was investigated and found to have little effect within the range of tunnel depths

used. The support beams are made up of two 0.25” plates of extruded aluminum and span the width of the water tunnel. The beams are secured to the top of the water tunnel using slotted fasteners and the existing threaded holes to sets of support plates. The support plates must be slotted because the location of the threaded holes on the top of the water tunnel are dependent on the depth of water in the tank as a reasonable amount of deflection occurs between minimum and maximum water tank depths.

2.2.3 Cavity length control

The length of the cavity L_c can be adjusted using a “T-clamp” to secure the structure to the fixed cavity gap wall on one side and the cavity face at the leading edge. The side plate that makes up the cavity is welded to the back face of the cavity closest to the trailing edge of the gap so the two components can be adjusted simultaneously to create a cavity of different lengths ranging from 0.3935 m to 0.7065 m. At the base of this configuration an “L-bracket” was used to locate and secure the assembly but was later replaced with long-reach clamps so as to not interfere with the flow for the final data set.

2.3 Flow Facility

In the investigation an open channel 0.45 m x 0.45 m water tunnel capable of an inflow velocity range between 0.26 m/s and 1.25 m/s was utilized. The system was produced by Engineering Laboratory Design Inc. and is designed to provide a uniform inflow profile within the test section by use of a honeycomb section and engineered diffuser downstream of the 25 HP pump motor. The wave-cavity resonator structure, a 1.2 m long acrylic test section, was mounted within this 2.5 m working length of the water tunnel. The test section contained elliptical inflow inserts mounted 1 m upstream of the cavity to provide a smooth inflow to the test insert. Depth was varied by raising and lowering the

test insert with precise spacers secured under the spanning beams supporting the insert. Since the flow facility was used in the free-surface configuration it was necessary to add or remove water depending on the inflow velocity. Tests were carried out to determine the effect of the total depth on the inflow velocity for the depth and velocity range used in the investigation. Negligible instantaneous variation was found and the time-averaged PIV results were consistent.

2.4 Instrumentation

For each test the system was operated for 300 seconds before data collection began to ensure that steady-state conditions were reached based on initial observation of system changes. It should be noted that for cases where mode jumping occurred this could not be accommodated. Additionally, the system was started from a non-resonant state with zero flow for each test to limit hysteresis errors. Cases of hysteresis were observed wherein resonance could be reached for a range of inflow velocities but not for the same velocities when the system was reset by blocking the cavity opening length or when the velocity was reduced to zero and then increased to the value of interest rapidly. It was also observed that if a lower wave mode was allowed to resonate at a lower amplitude it could suddenly jump modes to a much larger amplitude.

2.4.1 Data acquisition

Data was collected using a National Instruments (NI) PXI-4472 sound and vibration measurement module with built-in anti-aliasing capabilities. This module allows 24-bit sampling of up to 8 analog channels at a rate of up to 102.4 KS/s [31]. For the optimized configuration result, a frequency of 3.26 Hz corresponding to the second hydrodynamic

mode was expected to be the highest measured frequency. To avoid aliasing and to ensure that the original waveform is recoverable the Nyquist criterion is used stating that [32]:

$$f_{sampling} > 2f_{measured} \, . \tag{2.1}$$

In this case, the minimum sampling rate for the investigation was set to 6.52 Hz. The sample rate used for the wave gauge channel was 1 kHz exceeding the required Nyquist sampling criteria. In order to avoid high-frequency noise from other oscillations in the system from aliasing below the critical frequency, a lowpass, eighth-order, Chebyshev filter with a corner frequency of 7 Hz was implemented using LabVIEW. Since the differential input configuration eliminates some degree of noise this filter was used primarily to preserve the signal from a sampling rate point of view. A 4^{th} order digital highpass IIR Butterworth filter with a cutoff frequency of 250 mHz was used to help supress the DC signal from the instrumentation system for purposes of viewing the frequency spectrum of the signal. Subtraction of the mean signal eliminated this issue and comparison of data sets with and without the highpass filter showed no variation so data was recorded with and without this filter. Noise from various potential sources within the system also exists from the blunt impingement plate, turbulent inflow, the lack of outlet expansion plates, and the effects of the elliptical inlet plates, in addition to flapping or vibration of the impingement plate and interactions between the radiative losses into the main channel. However, for the range of parameters used frequency analysis allowed these errors to be avoided and filtering was not required. A wave forming in the main channel for some cases with large values of L_{ec} was of similar amplitude and frequency to the cavity wave indicating it was the result of radiation. This can also been seen in

shadowgraphy of free surface variations where the wavefront is seen propagating out of the cavity. Since the mean flow in main channel is non-zero a Doppler shift of the wave occurs and explains the difference in frequency. Calibrations of the input signal were performed for increments of 0.05 m for 0.1675 m ranges centred within 0.015 m of the mean depth. In total 6 calibrations were carried out to satisfy the range of depths. Additional details surrounding the measurement of the free surface height are given in the next section.

2.4.2 Free surface height measurement

To observe the free surface wave within the cavity an RBR WG-50 capacitive wave-gauge was used and mounted on the downstream anti-node of the cavity at the midpoint of the cavity. This device can detect amplitudes of up to 0.15 m with a response time of only 2 ms and an accuracy of 0.4% [33]. Since the input voltage range is ±5.0 V the voltage increment with the 24-bit DAQ is found to be [32]:

$$\Delta V = \frac{5\ V - (-5\ V)}{2^{24}} = 5.96E - 7\ V$$

This corresponds to a spatial resolution of 1.675E^{-2} m/V or 9.983E-9 m, which is not utilized, as the accuracy of the WG allows for only a 1.2E-3 m resolution.

The WG was interfaced with the NI DAQ and using LabVIEW 9.1 with a differential input terminal configuration. This configuration requires the use of additional channels in comparison to RSE but allows for common mode noise rejection that may be present in the power source. For this reason the power phase used for the amplifiers was also used for the DAQ to ensure a common ground.

2.4.3 Flow imaging

A Photron AFX 30RS high-speed camera was used to track and record the free surface and associated wave modes with a 1024 x 1024 pixel resolution. Digital particle image velocimetry (DPIV) was utilized to observe the vortical structures forming across the cavity opening and convecting downstream and into the cavity. Illumination of 20 μm Ti_2O coated hollow glass spheres used as flow tracers was accomplished using a double-pulsed 25 mJ Nd:YAG laser. Associated flow images for intensity peak correlation were captured using the same Photron RS high-speed camera used in the free surface boundary tracking of the cavity free surface. The experimental setup is illustrated in Figure 2.4 with DPIV equipment scaled for simplified presentation.

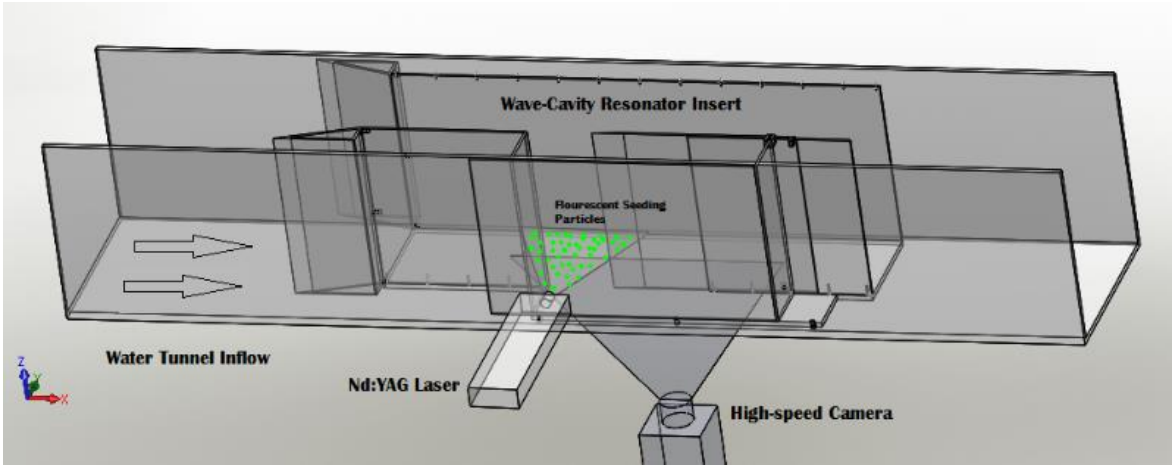

Figure 2.4: Schematic of the DPIV setup.

Image pairs were collected at a rate of 15 kHz with a time interval (dt) optimized to resolve the cavity opening length region resulting in a tracer intensity shift between image pairs of approximately 7 pixels [34]. This proved to be difficult at higher inflow velocities due to the high velocity gradient across the shear layer to the cavity and masking of a large cavity area was required for processing in some cases. Some images were also collected using a second PIV system at a rate of 5 Hz. Phase-resolved

background subtraction and a 528 nm band-pass filter were employed to reduce the effect of incident reflection from the free surface and internal reflections in the acrylic plates. Image processing was completed using LaVision's Davis 8.1.3 software using 1 pass of 32 pixel x 32 pixel interrogation windows with 50% overlap followed by 3 passes of 16 pixel x 16 pixel interrogation windows with 50% overlap.

The Stokes number is defined by the non-dimensional relationship:

$$S = \frac{\rho_s g d_s^2}{18\mu U}, \tag{2.2}$$

with d_s= 5-7μm, ρ_s= 0.0029g/cm^3, μ= 1.002x10^{-3}Ns/m^2, and U = inflow velocity in [m/s]. Using the parameters associated with the experiments the Stokes number used in the experimental investigation was within the range of 0.05 and 0.21. The Stokes number can be used to indicate how well a tracer particle follows the path of the fluid it is entrained in. For flow incompressible shear layers the slip velocity between the tracer and fluid particles for a Stokes number of 0.2 leads to only a 2% error [35]. For Stokes numbers <<50 compressibility has little effect on particle dispersion suggesting that a similar error could be expected at a given Stokes number for an incompressible shear layer [35]. Large scale vortical structures associated with organized shear layers, as observed in cases involving resonant coupling, can also introduce errors between tracer and fluid particle motion due to the density differences and associated centripetal forces. For incompressible shear layers, the tracer particles follow the path of large scale vortical structures for a Stokes number near 0.1 [36].

2.4.4 Free surface image tracking

In order to qualitatively assess the profile of the free surface, boundary tracking software was developed for use with the Photron AFX 30RS high speed camera and MATLAB. For surface profiles of interest a set of images was captured with a frame rate of 60 fps which satisfies the Nyquist Criterion from Equation 2.1:

$$f_{sample} > 2B$$

$$for\ B_{min} = 0.5\ Hz\ and\ B_{max} = 3.5\ Hz$$

$$2(0.5\ Hz) < f_{sample,range} < 2(3.5\ Hz).$$

Furthermore, nearly ten times these calculated values are used to provide high resolution of the waveform in addition to ensuring that anti-aliasing does not occur for future quantitative examination of the data. The greyscale images were converted to binary images after going through Gaussian filtering to enhance the contrast at the free surface boundary of the cavity wave. A starting position and search direction heading are input into the program to use as an initial search direction to find the boundary. The program then tracks the interface pixels along the free surface boundary and stores the locations in an array. The program was designed to allow a user to input the origin and two points to use as a spatial calibration scale for which the coordinates of the wave surface are stored in the output array. This program allows various modes of the wave to be stored and could even be used with future modification to determine the frequency spectrum at set points along the waveform: this is particularly useful for examining the effect of energy extraction caused by a wave absorber or the wave profile created by the wave maker. Because wave making/absorbing devices do not exactly match the motion of the wave, standing waves with decaying amplitudes form in a direction away from the paddle

causing non-linearities for non-shallow, higher amplitude waves [18]. For the analysis a Nikon AF Nikkor 24 mm lens was used settings summarized in Appendix D.

2.4.5 Wave maker power measurement

To measure the unsteady force on the wave maker and wave absorber paddle a Novatech F233-Z4346 load cell was used. The load cell was factory calibrated and balanced for up to 80 N along the x-axis with a force center of (x,y,z)=(0,0,335) mm and (x,y,z)=(58,0,335) mm. The paddle itself corresponded to an offset position in the x-direction of 0.02 m but by examining the output of the sensor for a range of offsets from 0.005 m to 0.14 m there was no variation seen: the construction of the load cell is such that there is no effect from deviating from the calibrated offset in the x-direction for the range used in this experimental investigation.

For the vertical offset however, there will be a variation in the output force due to the changing moment arm from the centre of load application on the paddle to the load cell earth end. This can be accounted for by subtracting out the mean output value caused by the static weight of the paddle from the final data in addition to compensating for the change in moment arm from that of the calibrated offset value during analysis of the data. The relationship between the offset distances in comparison to the calibrated value is linear over the range used for the experimental investigation. Calibration of the load cell was carried out in the lab to verify that the load cell had not sustained any plastic deformation to the cantilever strain gauge mounts or corrosion that would unbalance the bridge circuit and lead to offset errors. The load cell signals were amplified using Mantracourt Electronics SGA/A amplifiers that had been previously factory calibrated. The amplifiers used consisted of a factory-balanced Wheatstone bridge to avoid output

error with temperature variations. They also contained built-in analogue filters of a Butterworth topology with a series of switches with which the analogue cutoff frequencies could be selected. There was however significant high-frequency noise present of the order of ~1 N that was removed using digital filters during analysis. Comparison of the data with and without the analogue filters showed no effect on this noise so they were not utilized for the data set. While shielded with coaxial cables, this noise is most likely the result of the high-powered electrical supply for the linear table and water tunnel drive. The analogue filters also caused a slight delay in the load cell signal and slightly attenuate the spectral peaks of the data causing some error in the power calculations based on this data. The load cell measurements of x-direction and y-direction force and torque about the z-axis were recorded. While the x-direction was of primary interest and used for the power calculations the y-axis measurements were used to ensure that the data set was not compromised due to piston contact with the cavity walls resulting from misalignment or accidental lateral offset. Likewise, the torque data collected about the z-axis was used to verify that the piston face did not rotate and close the clearance gap or cause contact with the cavity wall: this was found to have a very significant effect on the measured power and resistance in the system. Load cell data was collected using the same NI PXI-4472 DAQ at a sampling frequency of 1 kHz, the lowest possible sampling frequency, while the linear table position was recorded using the Parker control system interface at a sampling frequency of 250 Hz.

2.4.6 Motion generation

A linear actuator produced by Parker Hannifin Corp (Model OSPE32-600L2-00680-PM2A6C) and Parker AR-XXAE Aries digital servo drive were used to provide the

motion that generated the path of the wave maker paddle at the required height to stroke ratio (H/S) and frequency. The onboard Parker ACR9000 controller allowed simultaneous uploading and recording of the rotary encoder position on the timing-belt-driven axis used at a given time step while also providing a feedback loop to follow a motion profile defined by a downloaded cam table. In order to provide a smooth motion profile, 101 points were used to interpolate the sinusoidal motion path and allow the frequency and amplitude to be scaled via user input data while running the motion generation code. These points were also scaled by a factor of 1000 to provide higher resolution to avoid jerk that can occur when the controller quantization results in rounding of cam table data to integer values during machine encoder unit conversion for controlling the encoder position. This motion profile is plotted in Figure 2.5 below and negligible variation is observed in comparison to the recorded position of the actual path.

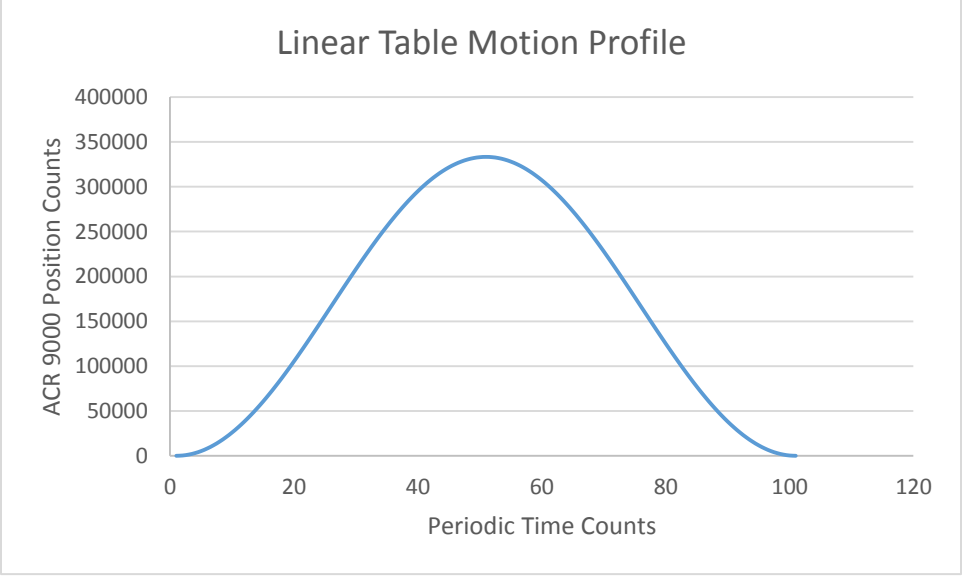

Figure 2.5: Profile for linear table encoder position.

The profiles started at the peak of the sine wave where acceleration is zero and jerk is infinite which provides a smoother profile. The program allowed the motion to start and

end at the same point to avoid hysteresis of the motion profile. The code running the motion profile of the linear table also triggered an output to start the LabVIEW virtual instruments that recorded the wave-gauge data and load cell data allowing synchronized values for analysis. This allowed direct comparison of the effect of the wave absorber/generator path on the standing gravity wave in the cavity and also the power required to generate such a wave with and without the presence of resonant coupling. In addition, recording of the 10 measured cycles did not start until after ramp up occurred to steady-state for a series of 10 proportional increases in amplitude. The paddle frequency was matched with the resonant cavity wave frequency measured during initial testing corresponding to 1.384 Hz and 1.538 Hz for the 0.102 m and 0.185 m depth cases respectively.

2.4.7 Post processing of data

Free surface height data collected by the wave gauge was processed using a custom MATLAB routine that calculated peak-to-peak amplitude over each wave period. The average peak-to-peak amplitude was returned along with the mean depth over the experiment. This allowed erroneous data to be detected in cases where average depth deviated from the experimental case by 10% or more. In addition, the mean peak-to-peak amplitude calculation allowed steady state oscillations to be distinguished from transient wave amplitude growth and decay that was commonly seen outside of the range of frequency lock-on. Further analysis was conducted to determine the power spectral density of the free surface height data in order to generate waterfall plots and contour plots for purposes of examining spectral peaks at lock-on and to determine empirical model parameters for predicting Strouhal frequency.

Power Spectral Density:

The power spectral density is useful for determining what frequency components of the cavity wave contain the most power. For the free surface height signal h(t) mean subtraction can be carried out to subtract the DC component of the signal. This allows the power spectra of the amplitude of the wave to be analyzed independent of the mean depth of the test case. Since each test consisted of a 30 second sample a finite signal that was much more periodic than transient was recorded. The truncated discrete Fourier transform was applied to the entire sampling interval of [0,tsamp]. Using the finite time series of the sample data $h_n = h[t = n*Tsamp]$ for the length of the sampling interval Tsamp (delta time between samples)and n-th sample of N total samples results in a power spectral density of:

$$S_{ff}(\omega) = \frac{Tsamp^2}{tsamp}\left|\sum_{n=1}^{N} h_n e^{-i\omega n}\right|^2 = \frac{Tsamp^2}{tsamp}\hat{h}_{truncated}(\omega)\hat{h}^*_{truncated}(\omega), \qquad (2.3)$$

where N is size of h[t], *tsamp = N*Tsamp* and $\hat{h}_{truncated}$ denotes the truncated FFT of the time series h[t] that was obtained by sampling the wave gauge signal capturing h(t) [37], [38]. The reduced spectral resolution as a result of this convolution is termed spectral leakage. To reduce spectral leakage, a Hanning window (w) is applied and a multiplier of 0.375 is applied to the denominator "tsamp" to compensate for the reduction in the signal's power due to the applied window reducing to:

$$S_{ff}(\omega) = \frac{Tsamp}{0.375N}\left|\sum_{n=1}^{N} wh_n e^{-i\omega n}\right|^2 = \frac{Tsamp^2}{tsamp}\hat{h}_{truncated}(\omega)\hat{h}^*_{truncated}(\omega)\,, \qquad (2.4)$$

since *tsamp = Tsamp*N*. The Hanning window offers better attenuation of distant side lobes in comparison to the Hamming window that provides superior attenuation at side

lobes closer to the primary peak. Since resonance occurs at integer values of the resonant frequency and higher modes are observed to have lower power the Hanning window is favourable: noise lobes far from the primary peak are attenuated whereas lobes that are closer to the primary peak and more likely to be harmonics are less distorted.

Wave absorber power:

Power calculations were performed using the linear actuator and x-axis load cell data but due to the difference in sampling rates between the two signals the x-axis signal was down sampled by first applying anti-aliasing filtering in decimating the data. This is necessary as down sampling the data can result in signal distortion due to aliasing of high frequency signal components [39]. A decimation factor of $M = 4$ was required to down sample from 1000 Hz to the sampling rate of the linear table encoder position of 250 Hz. To insure that no overlap of frequency components occurs during downsampling the cutoff frequency B must meet the following criteria [40]:

$$\mathrm{B} < \frac{1}{M} f_{Nyquist} = \frac{1}{8 f_{sample}}. \tag{2.5}$$

A second order lowpass digital filter of a Butterworth topology was used with a cutoff frequency of 7 Hz satisfying this requirement. The filter was applied with a zero phase shift approach where the data was first filtered in one direction then reversed in order and filtered again to reverse the phase shift. This was necessary since the piston position data obtained from the linear table at a sampling rate of 250 Hz needs to be in phase with the measured x-direction force obtained at a 1000 Hz sampling rate in order to provide accurate power data. The instantaneous power required to drive the piston in the x-axis can be determined from the relationship:

$$\dot{W}(t) = F_x * \frac{dx}{dt}. \quad (2.6)$$

The value of F_x was interpolated from averaging the value over the sampling interval corresponding to M*Fsamp centered about integer values of M. The paddle velocity was determined from the change in position of the paddle over the appropriate change in time also centered about integer values of M and numerical integration was completed to determine the average input power per cycle.

2.4.8 Errors associated with experimental data

Wave amplitude and Wave Gauge:

Wave gauge data was collected over a time interval of 30 seconds, which corresponds to a minimum of 10 full cycles and an average of 27 complete cycles. For locked-on cases, where waveforms were consistent, averaging of amplitude provides a good representation of the system. Where alternating hydrodynamic modes caused consistent alternating amplitudes or where growth and decay cycles of amplitude were observed significant wave height could be used to provide good representation of the data. In all cases, the system was run for 300 seconds to reach steady state, and hysteresis was eliminated by intentionally breaking down the shear layer coupling and allowing the cavity wave to decay to zero. Over an infinite number of cycles random noise should cause the processed data to fit a Gaussian distribution. For a finite number of cycles a t-distribution is appropriate and the relative error can be determined by finding the interval of comparison of the measured and expected mean values based on a given confidence interval (CI), standard deviation (σ) and number of cycles (n):

$$Relative\ Error = \pm z(n, CI)\frac{\sigma}{\sqrt{n}}. \quad (2.7)$$

The greatest standard deviation for a resonant case was found to be 0.0498 corresponding to a relative uncertainty of ±1.5% for a 95% confidence interval and 10 cycles. In reality, 38 cycles were measured giving a relative uncertainty of ±1.4%. This was for the highest inflow velocity for the deepest test case. The wave gauge itself has an accuracy of 0.4% as discussed previously and combined with lowpass filtering and adequate sampling frequency the results are reliable.

Power and Motion System:

Errors in the motion system correspond to backlash in the linear actuator and motor drive train, bias errors, and random noise errors. For each of the wave absorber tests 10 full cycles were collected after reaching steady state using 10 cycles of proportionally increasing amplitude. Bias error from zero error can be reduced by subtracting the static reading of the piston (eliminating a 21% to 31% bias error) and making a moment arm correction to account for the piston force centre offset in comparison to the calibrated force centre and calibration. The error from this offset without moment arm correction is limited to a maximum of ±0.24 % as measured [41]. Digital filtering applied to the signal eliminates distortion error due to aliasing and will attenuate high frequency noise components. Any random noise remaining can effectively be removed by ensuring that an adequate number of cycles are sampled for the average power calculation. Relative uncertainty for a confidence interval of 95% can again be calculated assuming that the random noise fits a t-distribution for a finite number of cycles. The standard deviations were found to be 0.1056 and 0.1451 for the 0.102 m and 0.185 m cases respectively resulting in relative uncertainties of ±5.6% and ±7.7% based on a 10 cycle average. These were the worst cases where maximum piston displacement occurred and EII was

dominant indicating that some degree of phase shift was present between the cavity wave and generated wave. Near the range of the peak efficiency measurements this error was of the order of ±1% for the 0.185 m case and ±0.25% for the 0.102 m case.

Flow visualization data:

As addressed previously in Section 2.4.3, the Stokes number can be used to give an indication of the discrepancy between the path of a fluid particle and a tracer particle and accounts for <2% error [35]. Masking of low- and high-speed regions of the flow was utilized to resolve the free shear layer and to optimize the pixel shift in correlated image pairs for this region. For a shift of 4-10 pixels a conservative RMS error of less than 0.05 pixels is present [34]. The tracer particle diameter itself is such that a near optimum diameter of 3 pixels is obtained for each of the interrogation windows and is associated with <0.1 pixel RMS error. Flow visualization results of the flow upstream of the cavity show that a uniform flow condition was present. This would indicate that the shear layer frequency and cavity frequencies are unaffected by the inflow. The authors of [6] concluded that distortions of the mean and unsteady approach flow result from the impingement geometry and must be considered for such geometries as slotted cavity openings. The effect on the inflow of a tapered impingement plate in comparison to the rectangular impingement used for the WCR was not investigated.

3 Response of Resonator

3.1 Overview of parameter ranges

Cavity wave amplitude data and qualitative free surface tracking results to identify cavity modes were obtained for the cases indicated in the following table.

Table 3.1: Experiments with inflow velocity variation (Lec = 0.161 m, Lc = 0.622 m).

h, m	Types of experiments
0.002	▲
0.036	▲ ■
0.040	▲
0.060	▲ ■
0.090	▲
0.120	▲
0.150	▲ ■
0.180	▲
0.200	▲
0.240	▲
0.270	▲ ■
0.300	▲ ■
0.330	▲ ■

▲ Measurement of amplitude, cavity
■ Free surface tracking

This data was used to determine appropriate relationships for predicting hydrodynamic frequencies, characteristics of free shear layer-cavity wave mode interaction, and effects of depth, amplitude, and added mass. Flow visualization of cases of interest provide further insight into shear layer-cavity mode interaction and the effects of depth for comparison to shallow results collected by Rockwell and Ekmekci [1] and Rockwell, Wolfinger, and Rozen [2]. Comparisons to systems undergoing resonant coupling of acoustic waves in air with cavity frequencies are also made.

Tests at a fixed inflow velocity of 0.97 m/s were also carried out with varying cavity opening length as summarized in Table 3.2.

Table 3.2: Experiments with cavity opening (Lec) variation without power absorber (U_∞= 0.97 m/s, L_c 0.622 m).

h, m	L_{ec}, m
0.036	0.03-0.21 in 1 cm increments and 0.385
0.040	0.03-0.18 in 3 cm increments, 0.161 and 0.195, 0.210
0.060	0.03-0.18 in 3 cm increments,0.161 and 0.195, 0.210
0.090	0.03, 0.06, 0.07, 0.09, 0.12, 0.135, 0.145, 0.15, 0.161, 0.165, 0.180, 0.195, 0.210
0.120	0.03, 0.06, 0.075, 0.09, 0.105, 0.12, 0.15, 0.161, 0.18, 0.195, 0.21
0.150	0.03-0.21 in 3 cm increments minus 0.06, and 0.161
0.180	0.03-0.21 in 3 cm increments minus 0.06
0.200	0.03, 0.05, 0.07, 0.09- 0.21 in 1 cm increments
0.240	0.03-0.21 in 3cm increments, 0.161, and damping for 0.18 and 0.21
0.270	0.03-0.21 in 3cm increments and 0.161
0.300	0.03-0.21 in 3cm increments and 0.161

The data collected for the tests listed above provides insight into the cavity opening threshold that must be exceeded in order for excitation of a cavity wave to occur in addition to supporting the depth effect observations of the former data sets. In addition, these results allow the empirical model for prediction of hydrodynamic frequency to be further validated. For larger L_{ec} configurations paired with smaller L_c lengths significant radiation losses were observed in preliminary testing when the wave was not confined to the cavity and propagated out into the mean flow. While these combinations have been avoided they should be considered in any future prototype design.

Wave absorber tests were completed for depths of 0.102 m and 0.185 m at the inflow velocities for which peak amplitude occurred as determined by an initial evaluation. The tested piston strokes in Table 3.3 and denoted as the variable "S" were calculated based on predicted wave height to stroke ratios of H, H/2, H/4, H/6, H/8, H/10.

Table 3.3: Experiments with h and S variation (Lec = 0.218 m, Lc = 0.516 m).

h, m	S, m
0.102	0.004, 0.005, 0.0067, 0.01, 0.02, 0.04, 0.08
0.185	0.005, 0.00625, 0.00833, 0.0125, 0.025, 0.05, 0.10

Average power required to drive the wave absorber was calculated to give insight into the sensitivity of resonant coupling to net positive or negative contributions from the piston and determine peak efficiency. The tests were accompanied by video recording for purposes of qualitative analysis and identification of possible future research efforts.

3.2 Effects of depth and inflow conditions leading to peak wave amplitude

The velocity variation datasets collected at constant depth and summarized in Table 3.1 for a cavity of fixed length of L_c = 0.622 m and cavity opening length of L_{ec} = 0.161 m are analysed in the current section. The effect of depth on primary cavity frequency is presented in Figure 3.1. Frequency data is obtained from the primary spectral peak of the power spectral density for each velocity test regardless of resonant coupling.

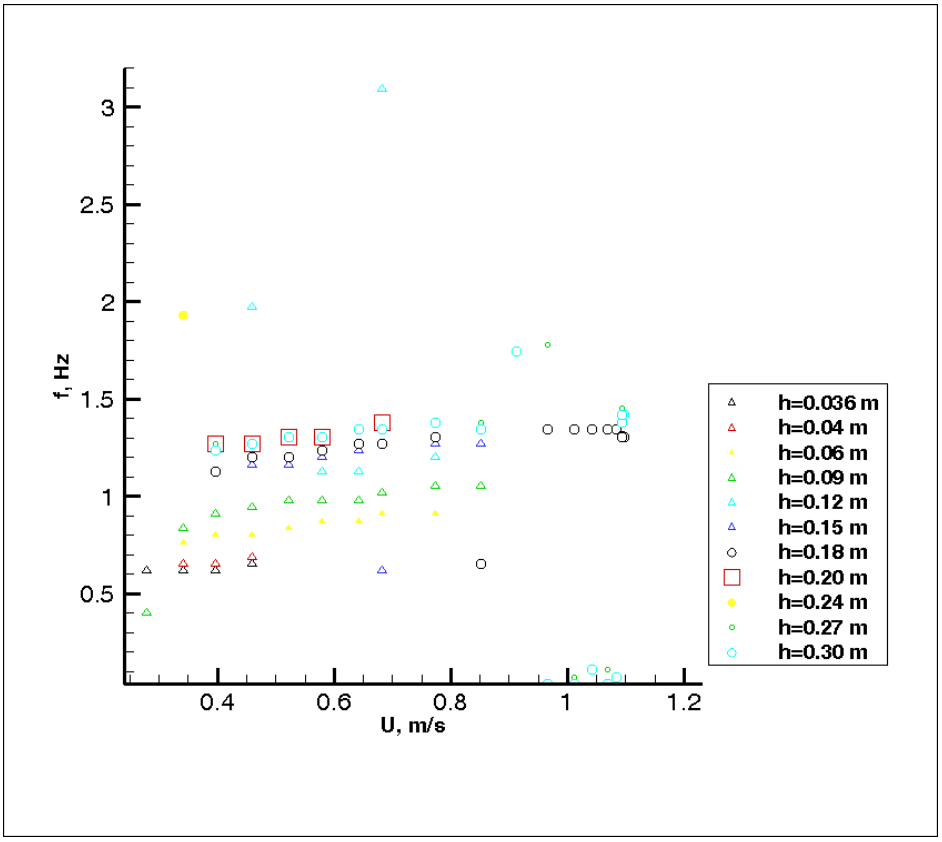

Figure 3.1: Frequency of the predominant spectral peak of wave amplitude for various depths for an inflow velocity range between 0.278 m/s and 1.120 m/s.

Secondary or tertiary peaks were observed for many of the deeper datasets ($h > 0.12\ m$) due to increasing non-linearities with increased depth, excitement of lateral cavity modes, and non-resonant broadband excitation of various cavity modes. These effects can be seen in the complete contour plots of each depth case that are included in Appendix C.

It can be seen that the fundamental resonant frequency of the cavity asymptotically approaches ~1.3 Hz with increasing depth as expected since water waves behave independently of depth above a threshold value of $h/\lambda > 0.5$. Data deviating from this trend is associated with non-locked on conditions where low-amplitude resonance with a system mode outside of the scope occurred. The slope of the f-U results characterizes the increase in frequency observed with increased inflow velocity that is addressed in Section 3.3.

Significant non-linearities appear to be observed at increased depth for a fixed range of inflow velocity. This is evident in the contour plots of the PSD for such cases. In particular, the 0.27 m and 0.30 m depth cases have a secondary spectral peak that is of the order of the primary peak as seen in the waterfall plot for the h = 0.27 m and h = 0.30 m cases. However, examination of the frequency spectra shows that these frequencies can correspond to 4^{th} modes of the cavity accounting for non-linearities associated with large amplitude waves or 1^{st} or 2^{nd} lateral modes of the cavity. For non-locked on cases the reflected and incident waves are out of phase leading to a cycle from a well-defined cavity wave to a very three-dimensional wave to a travelling wave.

Similarities to acoustically-coupled systems:

Longitudinal modes of resonance were observed, as seen by Rockwell et al for an acoustic coaxial side branch system, most often for the second cavity wave mode with open-closed boundary conditions [8]. As will be shown in Section 3.5, the higher modes were observed to be more complex but not necessarily of lower power than lower modes in contrast with the results of Oshkai and Yan for an acoustic coaxial side branch system [16].

Maximum observed cavity wave amplitude:

A maximum average cavity wave amplitude of what appears to be a locked-on case was obtained at a depth of 0.27 m and inflow velocity between 0.77 and 0.85 m/s using a cavity opening length of 0.161 m. The maximum cavity wave amplitude observed overall was for a depth of 0.15 m and an inflow velocity of 1.1 m/s. Contours of the PSD results for the 0.15 m test are given alongside cavity wave amplitude measurements in Appendix C; however, it can be seen that the excitation mechanism (the curve of hydrodynamic

frequencies) does not correspond well with the cavity mode present for this wave amplitude.

It is also unlikely that the secondary peak of this unexplained mode is excited due to the large cavity wave present since a secondary peak is also observed for cases with lower amplitudes ~1 cm (see h = 0.12 m case and h = 0.27 m case where this secondary peak actually corresponds to a lateral mode). Further inspection shows that a large range of frequency responses is measured with low Q-factors. Since the cavity acts as a fluid resonator with a distributed mass there are an infinite number of modes that can be excited. Broadband excitation of some of these modes is likely the cause: the measured maximum cavity wave amplitude is not attributed to resonant coupling and can be discarded. It does however show the cascading effect on amplitude of exciting multiple cavity modes suggesting that an energy harvesting device would be more effective with multiple excitation modes so long as geometry results in these frequencies being integer multiples.

Examining these data shows that theoretical cavity frequencies underestimate the locations at which resonance occurs for all but the second mode. This effect can be partially attributed to increased wave celerity with large wave amplitudes that are not incorporated into the intermediate water wave model. Improvement can be seen by examining the C4 Amp data series for h = 0.15 m based on the deep water wave model that does include the effects of large wave amplitudes in comparison to the standard small amplitude model of the C4 data series. Due to the cavity width used (0.125 m in the base setup), for some inflow conditions (for example 0.67 m/s and 0.78 m/s at h = 0.30 m) transverse standing wave modes were also excited and are seen as higher frequency

components that do not correspond to the streamwise modes that scale on the length of the cavity. In cases where this occurs or when another mode of the system is excited the resultant frequency of the cavity wave is a combination of these frequency components. One such resultant frequency can be predicted by substituting the appropriate wave celerity model c into the following relationship [22]:

$$f_R = 0.5c * \left[\left(\frac{n}{L_{c,eff}} \right)^2 + \left(\frac{m}{W_c} \right)^2 \right]^{\frac{1}{2}}, \tag{3.1}$$

where m denotes the lateral wave mode and W_c the width of the cavity.

The error associated with assuming small wave amplitudes can be estimated by using the appropriate predictive models obtained by Rouse (Equations 1.24 and 1.25.) A maximum increase in wave celerity of +9.5% due to wave amplitude for shallow cases occurred at depths of 0.06 m and 0.09 m and corresponds well with the under predicted cavity frequencies. For intermediate depths the more conservative shallow water model was selected limiting the frequency increase to <7%. Analysis of the deep water cases gave <+1% error for the first mode, <+3.4% for the second mode (h=0.27 m at max inflow velocity), a third mode maximum of +9.3% (h=0.27 m) with other results <+5%, and a fourth mode maximum of +17.5% (h=0.27 m) with other results <+10%. The second mode error for deep cases did not correspond well with the data as the cavity frequency model over predicted the cavity frequency. However, these cases were associated with lock-on and strong resonant coupling which may pull the cavity frequency to match the hydrodynamic frequency. This was observed during the experiments but has not yet been associated with definitive trends.

A trend of under-predicting the frequency of the cavity modes was observed for the cases of higher depths (especially for h = 0.27 m and 0.30 m) and can be attributed to the fact that the theoretical model addresses a closed-box solution for intermediate water waves. Adjusting the cavity length and switching from closed-closed to closed-open boundary conditions above shallow depth classification provides much more accurate cavity wave frequency prediction and supports the hypothesis that the closed-box solution under-predicts the frequency of the cavity modes as will be seen in the corrected contour overlays that follow.

PSD waterfall plots for the deeper cases at cavity depths of 0.27 m and 0.30 m (Figure 3.2 and Figure 3.3) show a unique attribute of the existence of a secondary peak with a magnitude of up to 25% of the primary peak near U =0.64 and 0.77 m/s respectively. The spectral peak of the dominant frequency component increases to a maximum value at peak resonance (U = 0.82 m/s) and then subsequently decays when the inflow velocity is increased further.

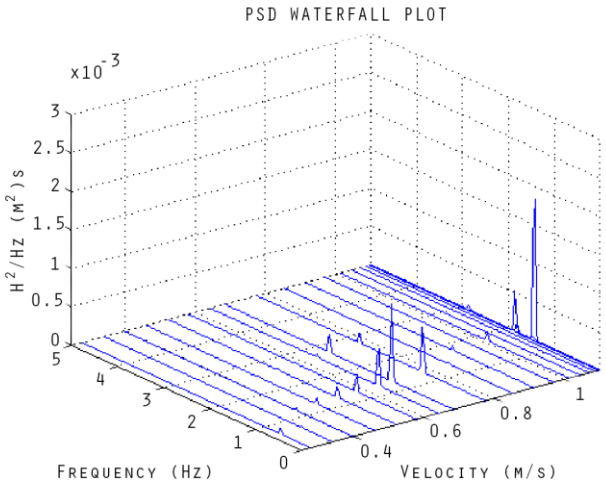

Figure 3.2: Waterfall plot of power spectral density data for fixed cavity opening length h=0.300 m.

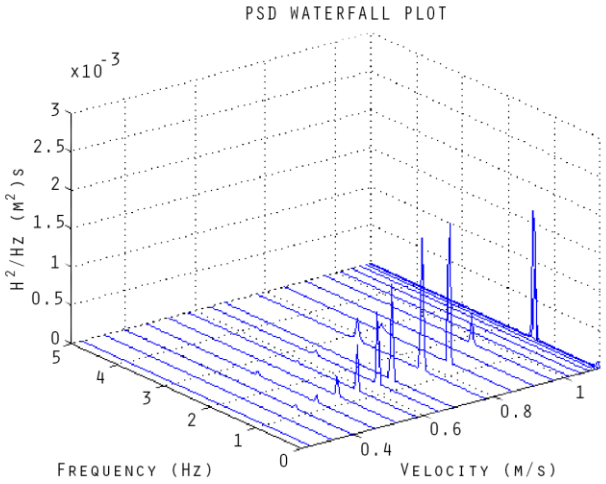

Figure 3.3: Waterfall plot of power spectral density data for fixed cavity opening length h=0.270 m.

It is of interest to note that the cavity wave amplitude at the lock-on condition (0.78 m/s ≤ U ≤ 1.1 m/s) for depths of 0.30 m and 0.15 m are within 12 % and 18%, respectively, of the 0.27 m case (where the overall maximum amplitude was observed) despite the fact that the depth has nearly doubled between the 0.15 m and 0.27 m cases. Notice the broadband excitation present in the case of h = 0.15 m seen as the large spectral peaks with low Q-factor near maximum inflow velocity for which a wave of amplitude 0.037 m is observed (Figure 3.4).

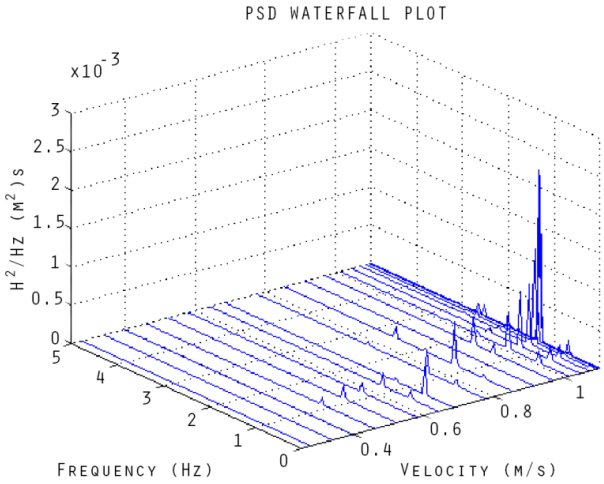

Figure 3.4: Waterfall plot of power spectral density data for fixed cavity opening length h=0.150 m.

Two spectral peaks were found to be associated with large amplitude resonant coupling of the shear layer and cavity wave. Even for non-locked-on cases as seen in the h = 0.120 m waterfall plot in Figure 3.5 the frequency component at ~1.2 Hz and secondary peak were associated with a significant cavity wave.

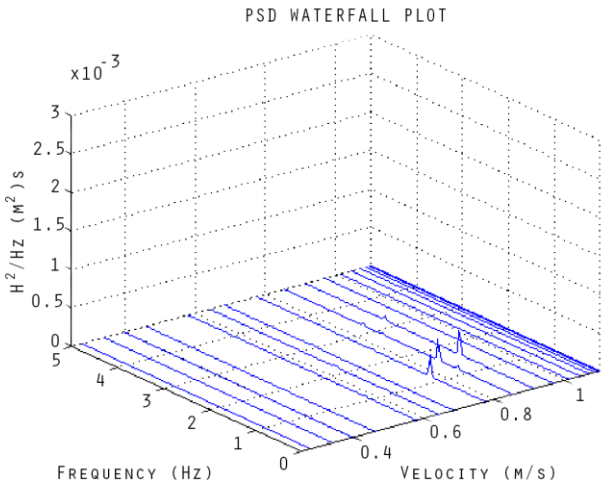

Figure 3.5: Waterfall plot of power spectral density data for fixed cavity opening length h=0.120 m.

For this case, shear layer organization occurred, but lock-on of the shear layer and cavity coupling was not maintained. Rather, the vortex impingened on the trailing edge of the

cavity, and the amplitude of the wave for all related cases was found consistent with the depth of the free surface depression associated with the vortex. As the depth was increased, the frequency signature at ~1.3 Hz in Figure 3.5 was observed for an increasingly lower band of inflow velocities. In other words, the given primary spectral peak frequency could be obtained for a lower inflow velocity at a deeper depth. The following figure presenting the peak frequency data as a function of depth is also of interest.

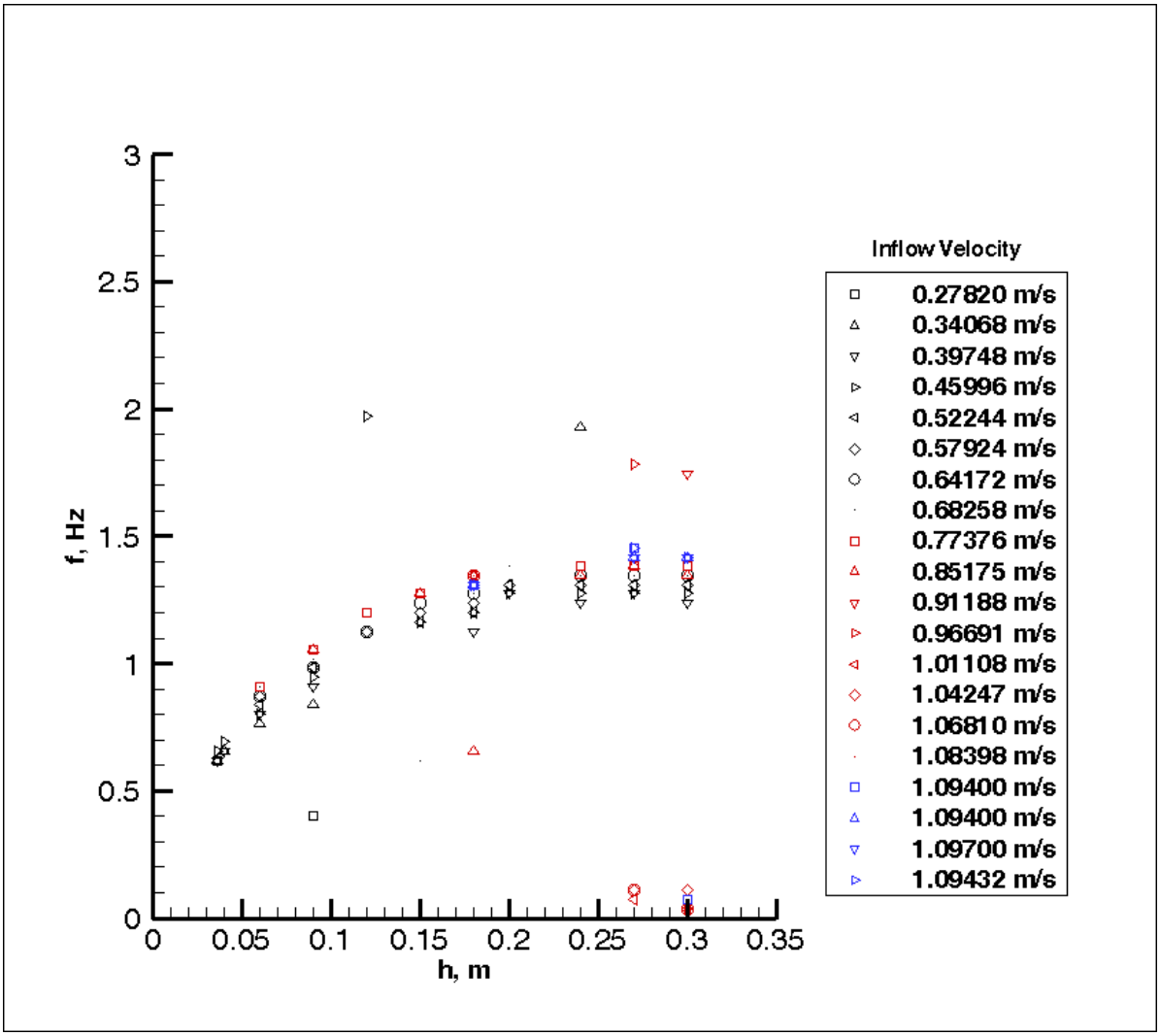

Figure 3.6: Frequency of the predominant spectral peak of wave amplitude at a given depth for inflow velocities between U = 0.278 m/s and U = 1.120 m/s. The outliers correspond to modes other than the streamwise modes that scale on the length of the cavity.

Notice that in Figure 3.6 the 0.64 m/s cases fall almost exactly along the midpoint of the frequency data points for the range of depths showing that lock-on occurs near the middle of the frequency range corresponding to a frequency lock-on between the hydrodynamic and cavity frequencies. In cases where hysterisis was observed (specifically when the velocity was increased incrementally between tests rather than resetting the system), this velocity band was shifted up vertically and skewed since peak lock-on still occurred around the original midband points: the upper limit on the velocity for which resonance would occur increased since the frequencies could be shifted to stay locked-on when velocity was increased incrementally from an already locked-on state

In summary, as the water depth was increased for the cases of L_{ec}=0.161 m and L_c=0.622 m, transitions occurred in terms of whether primary, secondary or tertiary modes were excited. For the cases of L_{ec}=0.161 m and L_c=0.622 m the system obtained higher self-sustained oscillations with increasing depth due to a closer matching of streamwise cavity wave frequencies with hydrodynamic frequencies.

A detailed discussion documenting characteristic spectral properties and analysis and identification of secondary and tertiary system modes as the system depth is increased is presented in Appendix C. In the current discussion these trends are summarized and the frequency predicting formulas are examined.

3.3 Prediction of fundamental hydrodynamic frequencies

The initial hypothesis of the analogy between the resonant free-surface waves and flow-induced acoustic resonances was shown to be invalid for the range of parameters outlined in Section 3.1.

While the resonant coupling was initially thought to be sub-critical, in which case compressibility and radiative effects are negligible, it soon became apparent that a more complex model was required. One such model, determined independently and later found to already exist, is outlined in the following discussion.

The fundamental frequencies for the hydrodynamic mode can be estimated from empirical data for a cavity of a similar L/D ratio based on experiments performed by Rossiter for air given in Equation 3.4 as [26]:

$$f = U_\infty \, (\mathrm{n} - \Upsilon)/(\mathrm{L_c}(1/\mathrm{K} + \mathrm{Ma})). \tag{3.4}$$

For a geometry of L/D=4, where $L=L_c$ and $D=W_c$, the constants Υ and K correspond to 0.25 and 0.67 respectively where K represents the ratio of the free-stream velocity to that of the convective velocity of the shed vortices both in relation to the cavity opening length [26]. While the Mach number (Ma) was used by Rossiter for the aero-acoustic system it had no implications on the free-surface system at hand. The model used above for compressible air experiments is analogous to the case of vortex shedding coupled with free surface oscillations. In this situation the hydraulic Froude number, given by $Fr=v/(gh)^{-0.5}$, is the dimensionless parameter that relates the speed of the pressure feedback (due to wave celerity) in comparison to the relative velocity dominating the system (for this case the inflow velocity) and is modified to:

$$f = U_\infty \, (\mathrm{n} - \Upsilon)/(\mathrm{L_{ec}}(1/\mathrm{K} + \mathrm{Fr}/\mathrm{K})). \tag{3.5}$$

Parameters of Y=0.25, K1=0.62, K2=0.33, and K3=0.38 fit all data sets except the 0.27 m and 0.30 m depths, where the Kn notation uses n to denote the hydrodynamic mode. For these cases the parameters best fitting the data differed only with K2=0.49. The results can be seen most easily by examining the overlay of this frequency prediction with contour plots of the power spectral data (Figures 3.7 - 3.9) obtained from free surface height measurements. The hydrodynamic frequencies correspond with the spectral peaks for most cases with the exception of the low frequency component on the h=0.30 m, h=0.18 m and h=0.15 m cases where an external mode or noise may be the excitation mechanism. The cavity wave, caused by pressure fluctuations from impinging vortices or vortex path at the trailing edge of the cavity, causes pressure fluctuations at the leading edge of the cavity that affect vortex formation: this situation is analogous to that observed by Rossiter for acoustic radiation [26]. Based on this acoustic analogy a series of pressure fluctuations caused by the leading and trailing edge interactions would have frequencies lying within (n- ϒ) and would cause resonance when one of the frequencies falls within a threshold of the resonant frequency of the cavity.

In Equation 3.5 above L_c was replaced by L_{ec} for the system at hand. The model used to predict $L_{c,eff}$ presented in the background theory as Equation 1.9 is modified by replacing L_c by L_c-L_{ec} and resonator diameter D by the hydraulic diameter resulting in:

$$L_{c,eff} = \left(1 + 0.48\frac{D_H}{L_c - L_{ec}}\right)^{0.5}. \tag{3.6}$$

This model predicts wavelengths of un-driven (does not work with larger energy contribution via wave generator than shear layer contribution) cavity waves within 6% of the measured wavelengths for the 2nd, 3rd, and 4th modes. The 1st mode of was less accurately predicted within 10% of the measured wavelength and in some cases this

frequency component was best predicted by a closed-closed model. The value of $L_{c,eff}$ calculated from the measured wavelength was lower by 10% for the first mode, 6% for the second mode, and 2% lower for the third mode. However, using L_c rather than L_c-L_{ec} under-predicted the cavity frequency by a degree similar to that predicted by accounting for wave celerity increase with significant wave amplitudes. Examining the PSD contours in Appendix C shows that resonance can occur by shifting of either the cavity frequency (change in λ) or the hydrodynamic frequency. This is also supported by a shift in wavelength when the power contributions for a wave generator were greater than those of the shear layer indicating that the system frequencies may shift in favor of the dominant energy contribution. Since cavity wave frequency is a function of wave height and the wave height is a function of the degree of lock-on, which as just mentioned is not limited to cavity frequency shift, the prediction of the cavity frequency is not trivial. An improved model may be obtained if the inherent coupling of the effective cavity length and shear layer organization, mode, and magnitude can be incorporated. Once again, it is stressed that this model does provide a degree of accuracy for purposes of initial design.

The model was further validated by showing that the wavelength is predicted well for the L_{ec} variation tests within 6.5% of the predicted wavelengths. The L_{ec} variation also allows the hydraulic diameter to be confirmed as a function of cavity width and depth rather than cavity opening length and cavity depth where the W_c model better predicted cavity frequencies. Using W_c resulted in only a 2% improvement and had little effect on the results in general. For cases with shifted wavelengths however it was difficult to distinguish which model worked best. The open-closed boundary conditions allow the lower frequency components to be explained as 1^{st} cavity modes and resulted in close

prediction of cavity wave wavelengths. The prediction of cavity wave frequencies using this model became more accurate with increased depth with error of 26 % at 0.09 m, 11 % at 0.15 m and 7 % at 0.30 m. The model was also tested at a fixed inflow velocity of 0.91 m/s for varying depths and values of L_{ec} as summarized in Section 3.6.

The hydrodynamic frequency prediction models are overlayed with theoretical cavity frequencies and experimental results for cavity wave amplitude and associated power spectral density above a threshold value of 3.6x10-5 m^2s. The model does not account for the effects of viscosity and assumes a constant convective velocity. For low Froude numbers this assumption regarding the convective velocity was reasonable. However, at higher Froude numbers or when mode mis-matching or large amplitude waves were present the vortex path varied widely. In some cases the vortex was ejected into the mean flow where it accelerated or convected into the cavity where took various paths including attachment near the trailing edge.

The natural frequency of the cavity using the intermediate depth water wave formulations for a basin with open-closed boundary conditions and a corrected cavity length obtained from in Equation 3.6 are denoted C1, C2, and so on. Similarly, hydrodynamic frequencies predicted by Equation 5 using the cavity opening length as the critical dimension are denoted H1, H2, and H3. Where resonant lock-on occurs between a cavity mode and hydrodynamic mode the corresponding threshold peaks in the PSD and cavity wave amplitude data are linked and denoted P1, P2, and so on. The same convention is used in the more detailed discussion in Appendix C with some additions noted at the beginning of that section.

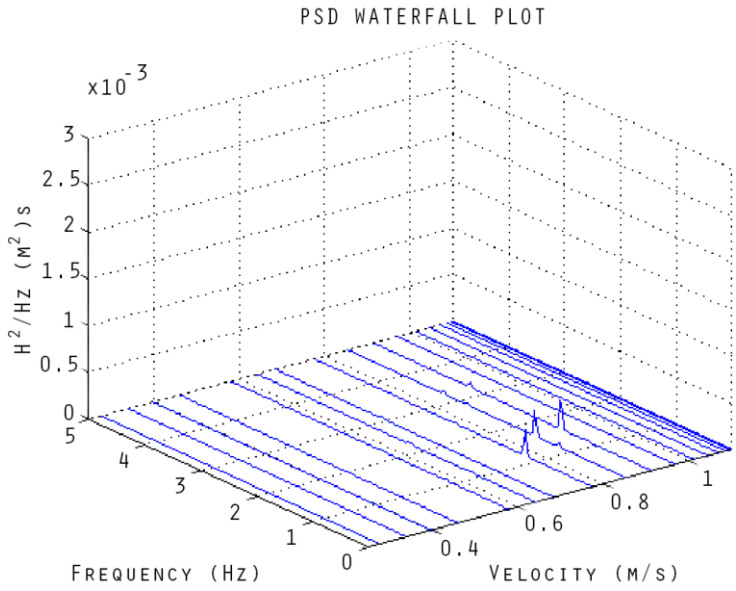

Figure 3.7: Water fall plot showing power spectral density peaks for h = 0.12 m, Lc = 0.622 m, Lec = 0.161 m, U= 0.278 to 1.1 m/s.

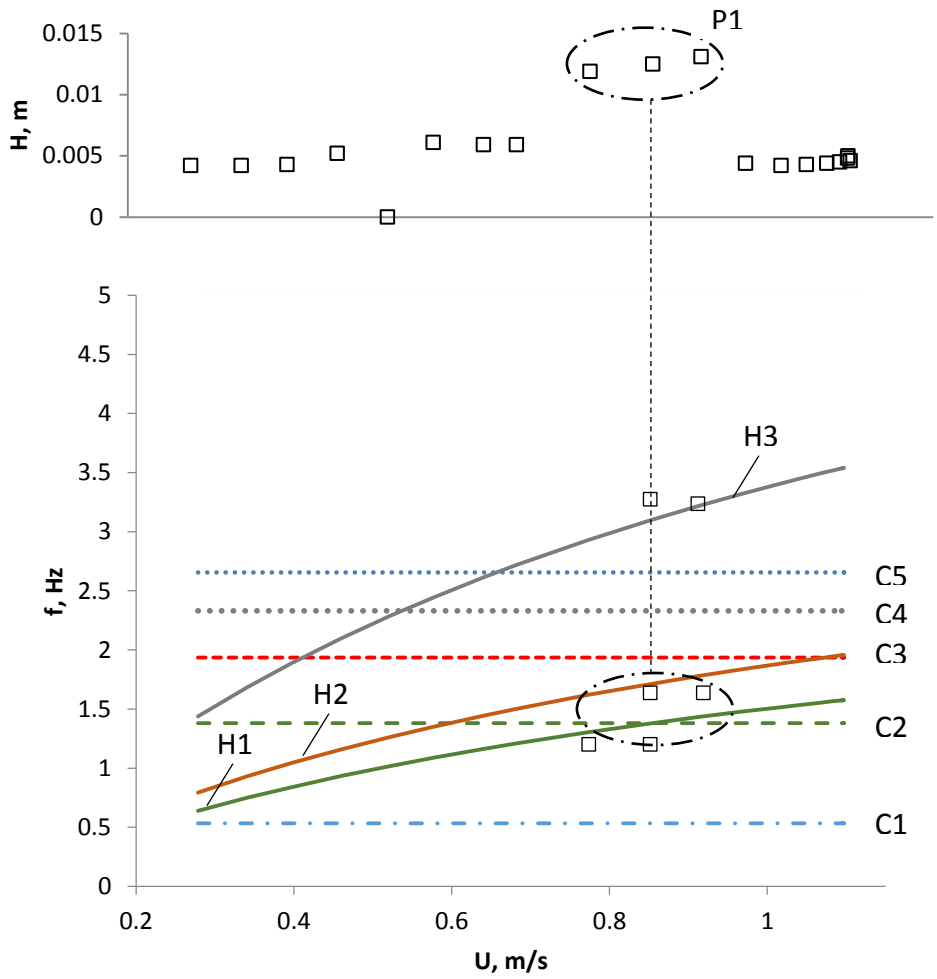

Figure 3.8: Overlays of cavity frequency for intermediate water depth and corrected cavity length and hydrodynamic frequency with Froude number correction corresponding to wave amplitude and power spectral density peaks for h = 0.12 m, Lc = 0.622 m, Lec = 0.161 m, U= 0.278 to 1.1 m/s.

For a fixed depth of 0.12 m and cavity opening length of 0.161 m experimental data is presented in Figure 3.7 and Figure 3.8 above. In this case we see that a peak amplitude of 0.0131 m occurs where the third cavity mode (calculated using open-closed boundary conditions and corrected cavity length) matches the second hydrodynamic mode of the separated shear layer. A significant high frequency component occurs near H3 and the second lateral mode of the cavity at inflow velocities of 0.85 and 0.91 m/s. This high

frequency component corresponds to a deep water wave lateral mode of the cavity with $L_{eff}=W_c$ and closed-closed conditions. Using the appropriate conditions a frequency for this lateral mode of 3.53 Hz is predicted and is within +10% of the measured component. More details are given in Appendix C where comparison to harmonics and mode jumping is also discussed. Lesser PSD peaks that do not exceed the threshold value are observed corresponding to interactions between the second hydrodynamic mode and second cavity mode and between the primary hydrodynamic mode and second cavity mode. However, it is apparent that the cavity frequency of the third cavity mode is over predicted by the theoretical model for the maximum amplitude case. A significant wave amplitude is not present, suggesting that non-linear effects on wave celerity due to wave height do not explain this disparity as simply the second cavity mode when correcting for wave amplitude using Equation 1.25 although a second mode wave is occasionally observed. This may demonstrate that a strong second hydrodynamic mode has pulled the cavity frequency by shifting the wavelength.

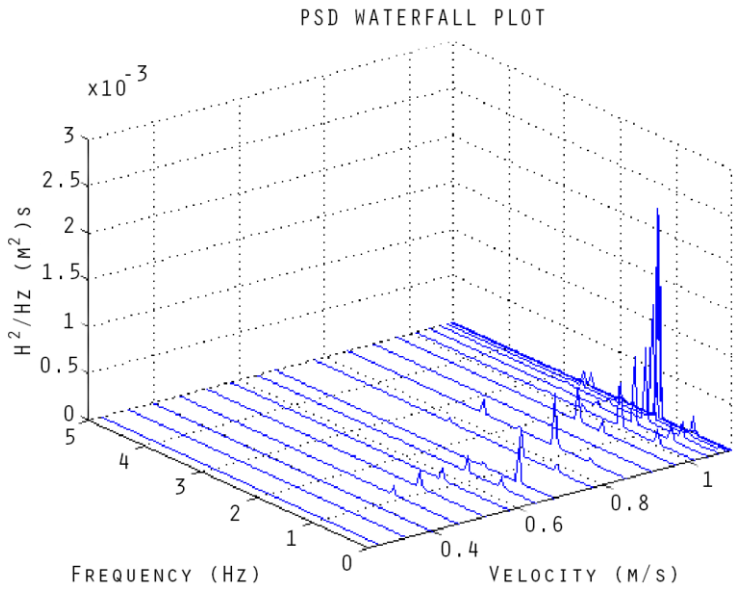

Figure 3.9: Waterfall plot showing power spectral density peaks for h = 0.15 m, Lc = 0.622, Lec = 1.161, U= 0.278 to 1.1 m/s.

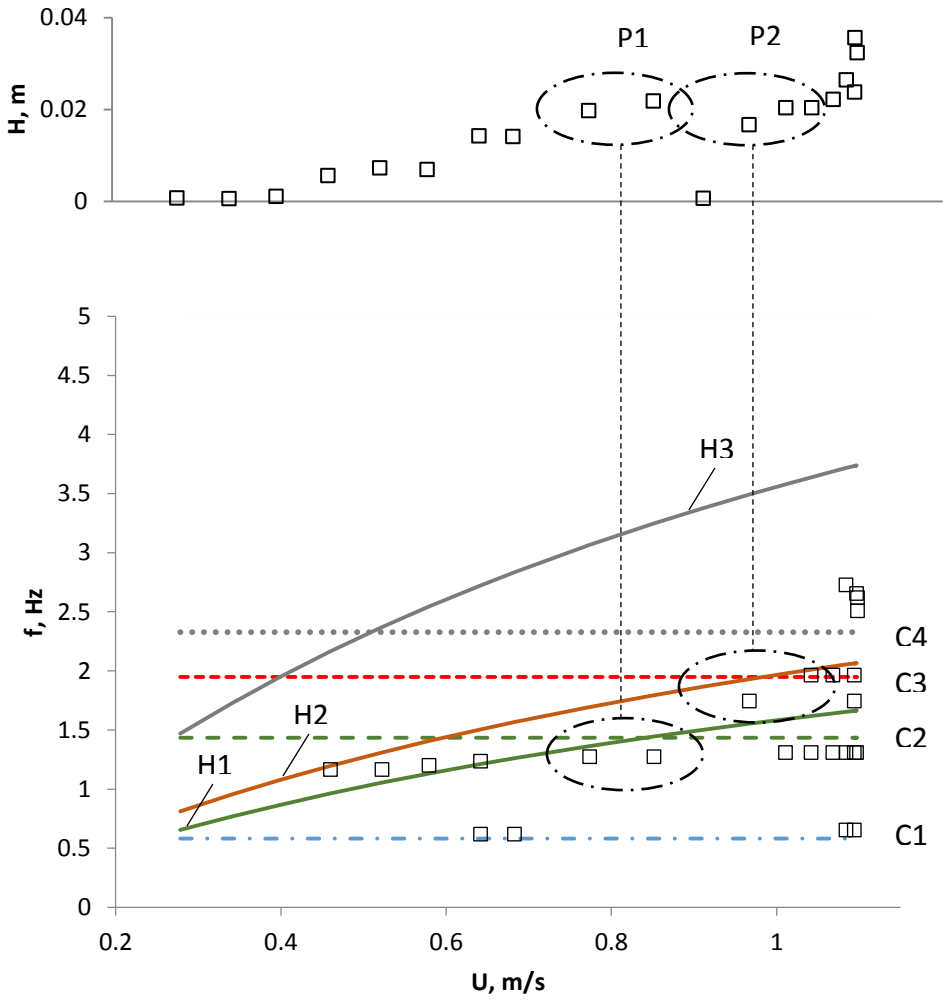

Figure 3.10: Overlays of cavity frequency for intermediate water depth and corrected cavity length and hydrodynamic frequency with Froude number correction corresponding to wave amplitude and power spectral density peaks for h = 0.15 m, Lc = 0.622, Lec = 1.161, U= 0.278 to 1.1 m/s.

The results for the h = 0.15 m case are given in Figure 3.9 and Figure 3.10 and are perhaps the most interesting of the tests in that a very three-dimensional wave with significant lateral and longitudinal modes is observed. A maximum amplitude of 0.0356 m is observed at the maximum inflow velocity but the data set is unable to capture the peak amplitude due to the limitations of the flow facility in an open channel configuration where pressurization is not possible. In any case, the spectral peaks at maximum inflow

velocity do not correspond well with interactions between the free shear layer and a cavity mode. While a second hydrodynamic mode and third cavity mode interaction occurs near maximum inflow velocity the main frequency components are observed near the second and primary cavity mode frequencies. The wide range of frequencies observed without corresponding interactions and poor Q-factor indicates broadband excitation of cavity modes rather than excitation from a shear layer mode of interest. In this case primary hydrodynamic mode and second cavity mode (P1) and second hydrodynamic and third cavity mode (P2) interactions are observed and correspond to resonant coupling. The low frequency component occurring at the primary cavity mode frequency near 0.64 to 0.68 m/s, however, is also not explained by the hydrodynamic model. Additional insight is given in Appendix C.

It is apparent that a highly complex system can be excited requiring careful consideration from an energy harvesting perspective; while potentially providing additional power contributions to the wave, the many frequency components would require special consideration in terms of matching phases of the net power harvested from the system to these contributions to avoid breaking down the coupling. This may prove impractical due to the further complication of shifting frequencies depending on wave amplitude height and standing waves and phase shifts caused by the motion of wave absorbers discussed in Section 2.4.6.

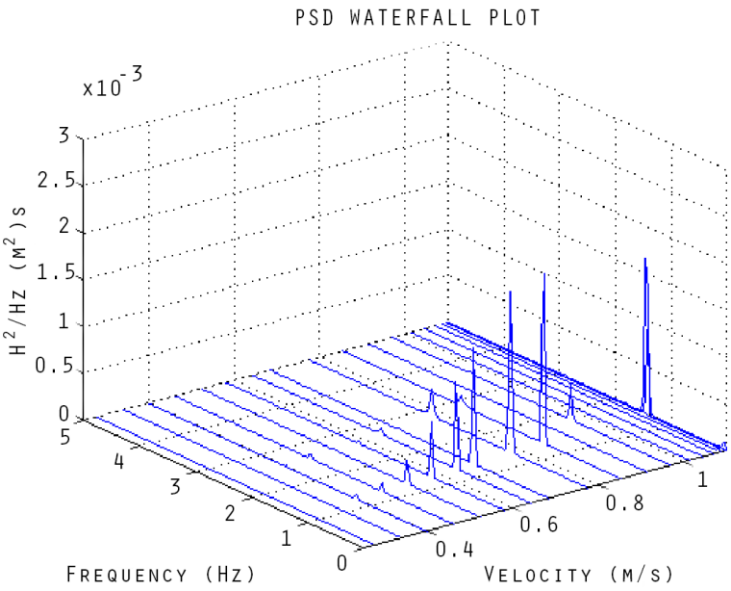

Figure 3.11: Waterfall plot showing power spectral density peaks for h = 0.27 m, Lc = 0.62, Lec = 0.161, U = 0.278 to 1.1 m/s.

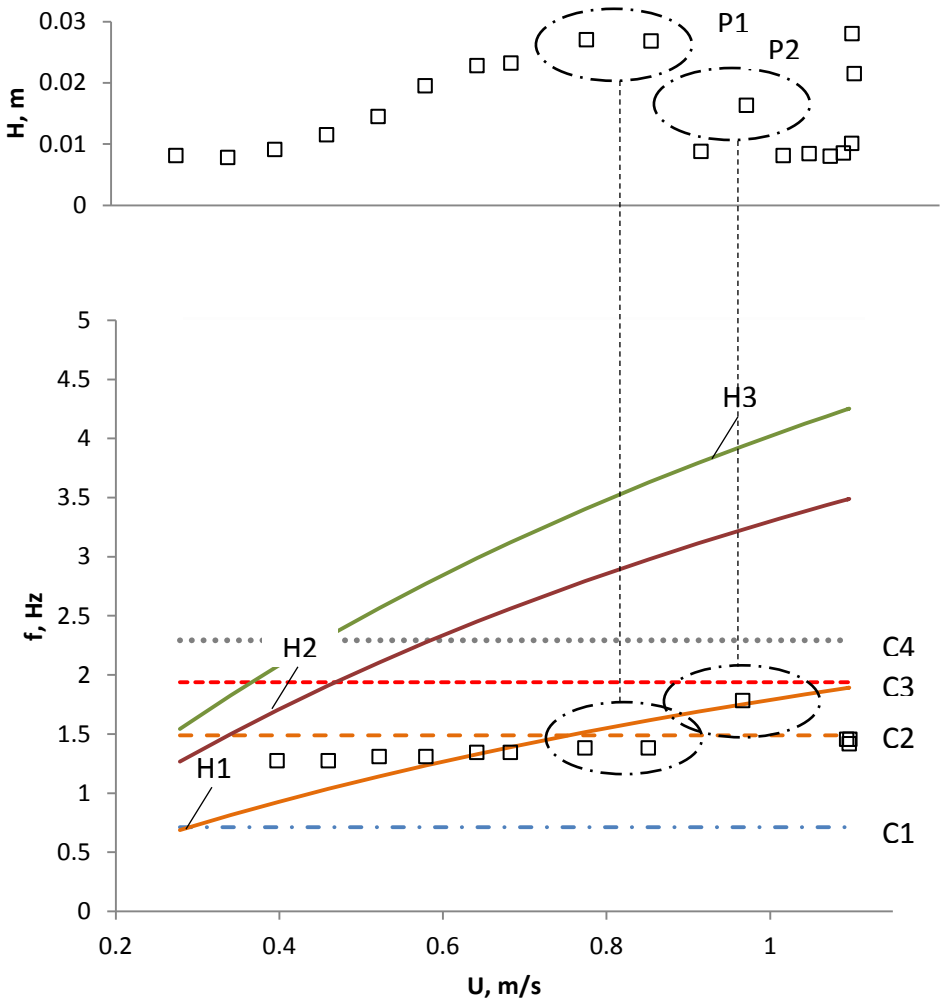

Figure 3.12: Overlays of cavity frequency for intermediate water depth and corrected cavity length and hydrodynamic frequency with Froude number correction corresponding to wave amplitude and power spectral density peaks for h = 0.27 m, Lc = 0.62, Lec = 0.161, U = 0.278 to 1.1 m/s.

At a depth of 0.27 m the maximum peak cavity wave amplitude of any test was found to be 0.027 m at an inflow velocity of 0.77 m/s. The results are presented in Figure 3.11 and Figure 3.12 above. Non-linearities are once again observed in the form of significant secondary spectral peaks and resonance broke down after 0.91 m/s until the end effects occurred. As the inflow velocity is increased the primary hydrodynamic frequency

approaches the over predicted second cavity mode frequency, the wave amplitude and spectral peak increase, and lock-on occurs at P1. Increasing the inflow velocity past peak resonance results in decreased amplitudes and eventual break down of the resonant coupling as seen in the wave amplitude and waterfall plot data.

An amplitude peak at P2 also occurs with an interaction between the primary hydrodynamic mode and third cavity mode near 0.97 m/s and then decays. The system parameters are matched well enough that a cavity wave is observed with a minimum of 0.008 m wave amplitude for the lower velocity ranges. This is seen in the contour plot as a very wide band spanning the data set. The very large peak amplitude and spectral peaks observed at peak inflow velocity occurs near the second cavity mode frequency but is not within range of a hydrodynamic mode. The wide range of frequency responses across the cavity modes is not observed as it was for the 0.15 m and 0.18 m cases where broadband excitement near the upper regions of the flow are observed. However, this interaction is still considered outside of the scope of the investigation and is attributed to external excitation perhaps by lock-on with a mode that was previously causing the broadband excitation at lower depths.

System Hysteresis

The effect of wave amplitude on wave celerity reached a maximum of 17.5% for the fourth cavity mode as would be expected. This can provide insight into the hysteresis observed since the celerity of higher modes at deeper depths is affected more by wave amplitude than for lower modes. Therefore at inflow velocities at which higher hydrodynamic modes can be generated, interaction at lower hydrodynamic and cavity modes can cause wave amplitude to increase the effectively higher cavity mode

frequencies within range of a hydrodynamic mode and organization of the shear layer can be influenced by this higher wave mode and lead to mode jumping. The large wave amplitude can effectively help the system jump to higher mode interactions to maintain resonance whereas restarting the system for each test will result in eventual decoupling when the hydrodynamic and cavity frequencies diverge with increasing velocity and collapse of resonance is observed. This is as seen at the U=0.97 m/s data point in Figure 7.18 of Appendix C where PSD contours rather than data markers above a threshold value are shown. It should be noted that this higher mode interaction near the third cavity mode did not occur for nearly 20 seconds after reaching the correct inflow velocity. The previous point at U=0.91 m/s was recollected twice before leaving the system for 120 seconds without any observed resonance. When the system was not restarted however, both the 0.91 m/s and subsequent points resonated and the frequency spectrum was more continuous.

3.4 Effect of hydrodynamic mode on cavity wave for intermediate and deep water conditions

The hydrodynamic mode had a strong effect on the mode of the free surface at any depth tested and yielded similar results in comparison to shallow investigations [1]. A few points of contrast will be discussed alongside qualitative analysis. Qualitatively, non-linearities with increased depth were observed in that the shed vortex impinging on the trailing edge of the cavity deformed when entering the cavity. The vortex funnel occupied the top (scaled with depth, ~40% for the deep case) of the cavity and entered the cavity while the bottom stayed stationary near the point of impingement.

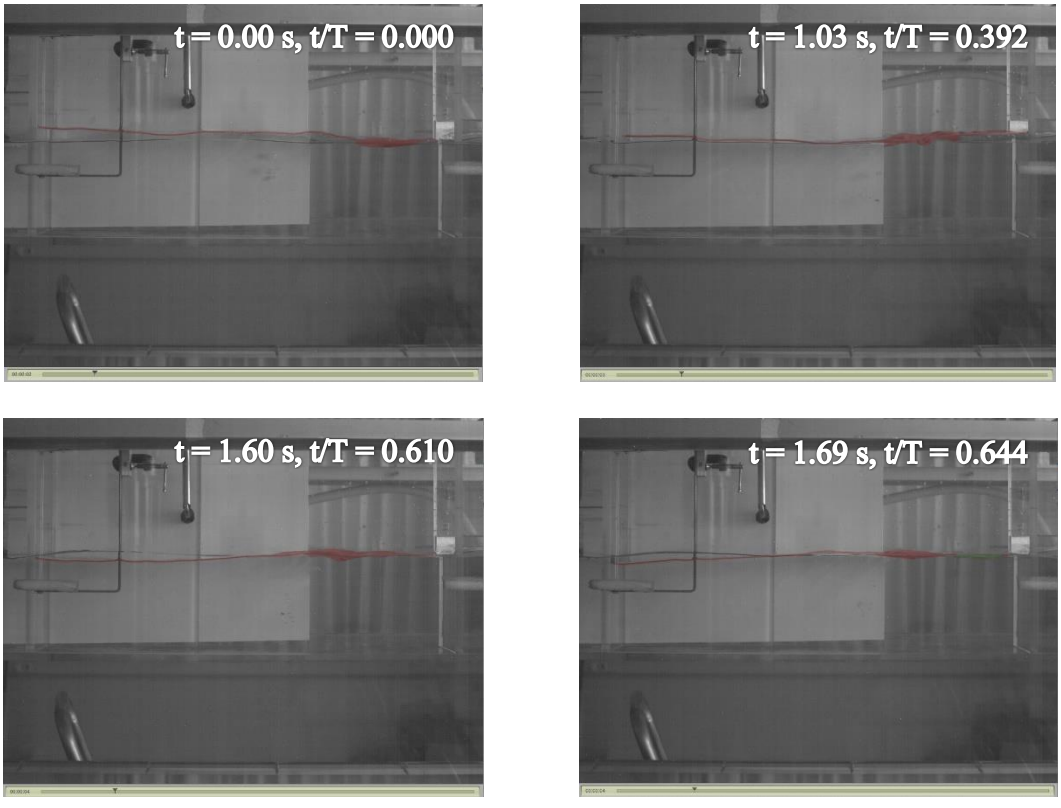

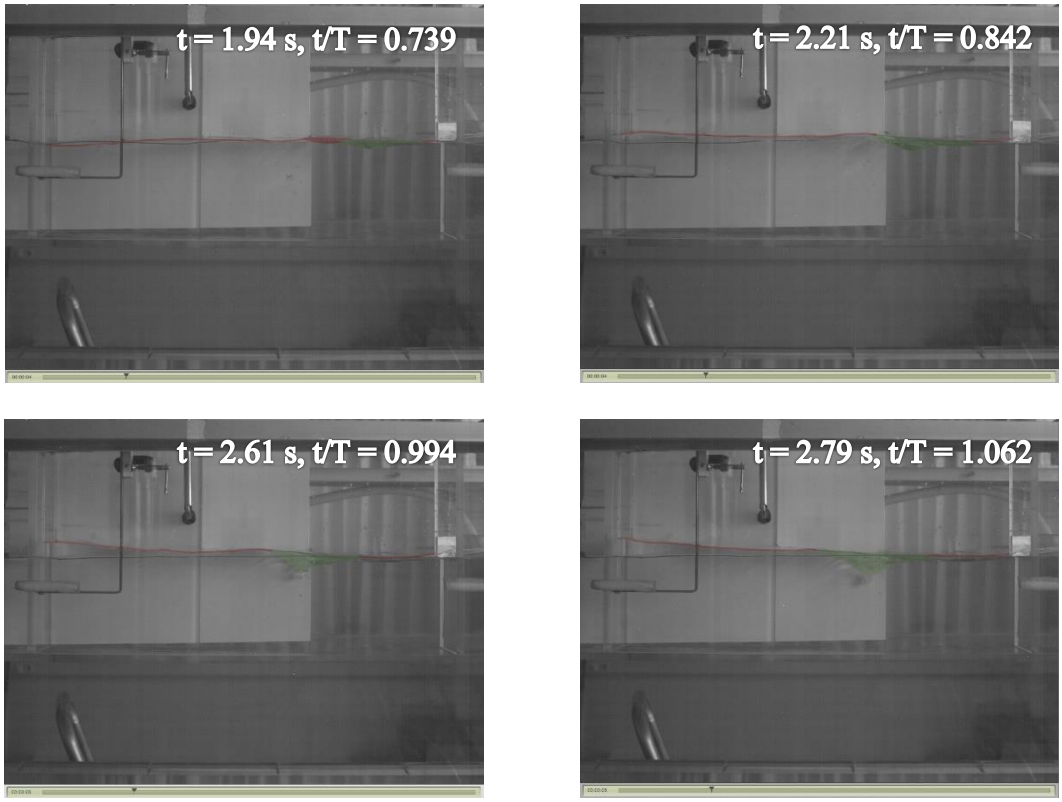

Figure 3.13: Vortex-cavity interaction with free surface-undulations corresponding to the primary (red) and the secondary (green) vortex and cavity wave period T. U=0.85 m/s, Lec=0.151 m, h=0.12 m, Lc=0.69 m.

Note in Figure 3.13 the presence of two vortices forming in the cavity gap (2^{nd} hydrodynamic mode) and also the stationary position of the vortex base in the vicinity of the impingement plate as seen by air bubbles entrained in the vortex.

In some cases where stronger resonance occurred the vortex base would convect into the cavity along a longer path but this was not typical. A possible explanation of this is that as the wave becomes a deep water wave, the water particles follow a nearly circular motion and the fluid particles near the bottom have little motion. If the ejection and intake of fluid into the cavity is due to the pressure variations caused by the free surface wave it would not occur at the lower region where the wave effects are negligible. To this

system it is as if resonant coupling is not occurring in that the vortex centre near the base of the vortex does not alternate about the cavity but rather impinges. Test cases of greater depth also had a tendency to stay close to the cavity wall rather than taking a path through the large scale circulation of the cavity as was observed with some intermediate depth cases. For shallow depths the vortex mostly impinges and collapses a short distance inside the cavity. Oddly matched modes of the free surface wave and the shear layer were sometimes compatible and in these cases shed vortices could be ejected into the mean flow at the trailing edge of the cavity due to the pressure variations of the free surface wave.

3.4.1 Effect of Depth

Similar to the trend of the amplitude data, the cavity wave amplitude approached a common maximum value as the wave approached a deep water wave regime. Above the deep water wave condition, assuming that compatible conditions leading to resonant coupling occur, this may represent the maximum energy that can be transferred from the mean stream flow. Increasing the depth past this point may lead to a decrease in wave amplitude due to increased wave damping and the limited region for which the shear layer can couple with the oscillating regions of the deep water wave to cause locked-on resonant coupling. This may be seen in that the deepest dataset (0.30 m) has slightly reduced amplitude in comparison to the 0.27 m depth case: data collected at larger depths could confirm this trend. However, as long as the ratios of the cavity geometry are controlled, a larger cavity and increased inflow velocity may be all that is required to obtain a larger wave amplitude as it is reasonable to expect that there is an optimum cavity geometry for a given inflow velocity.

3.4.2 Quantitative flow patterns

For a non-locked on case, small-scale vortical structures formed as a result of Kelvin-Helmholtz instability in the shear layer along the cavity entrance. In the impingement region, structures of a slightly larger diameter can form upon interaction with the trailing edge of the cavity and subsequent periodic large-scale vortex formation can occur. While these structures convect past the trailing edge of the cavity at symmetrical angles it can be seen that the majority of the structures do not enter the cavity but rather convect downstream with the main channel flow (positive x-direction). No periodic organization of these structures is observed and inspection of the velocity field data of the cavity shows large-scale circulation without periodic and sudden ejections or influxes of fluid into the cavity.

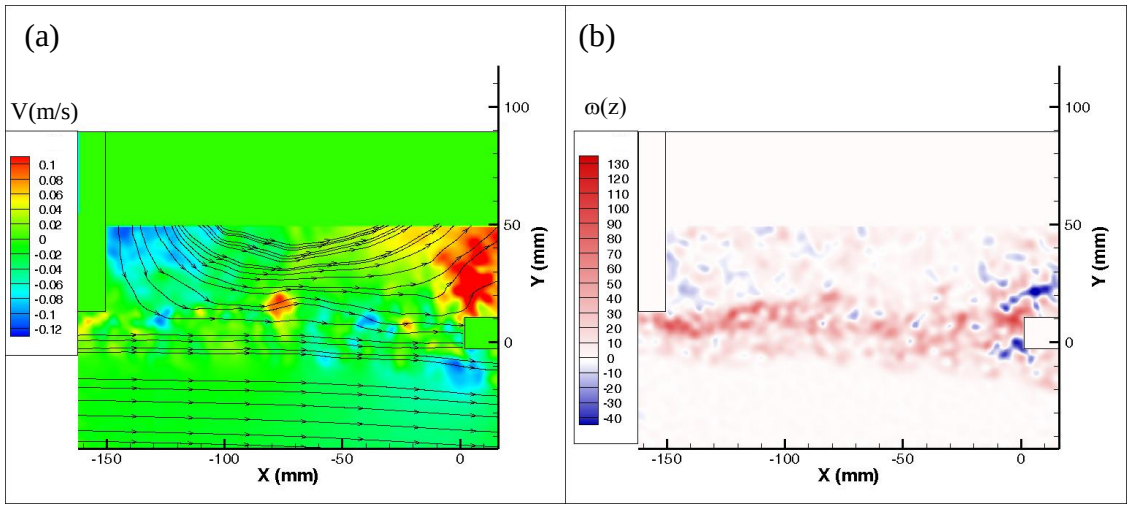

Figure 3.14: Instantaneous velocity field streamlines and [j] component contours(a) and contours of out-of-plane vorticity (b) in the absence of cavity standing gravity wave. U=0.65 m/s, Lec=0.155 m, h=0.185 m, Lc=0.69 m.

Adjusting the inflow velocity such that a locked-on state occurs results in the formation of large-scale vortical structures across the shear layer. These structures cycle through impingement on the trailing edge of the cavity, downstream convection into the main

flow, and convection into the cavity region itself. For cases of strong resonance, the vortex follows a path alternating escaping or entering the cavity. The shear layer oscillates in phase with the standing gravity wave in the cavity and greatly affects the cavity mode observed [18]. The shape, or hydrodynamic mode of the oscillating shear layer, and frequency correspond to the shedding frequency and number of large scale vortices shed from the leading edge. The primary hydrodynamic mode and associated low amplitude primary cavity wave mode are seen in Figure 3.15 below.

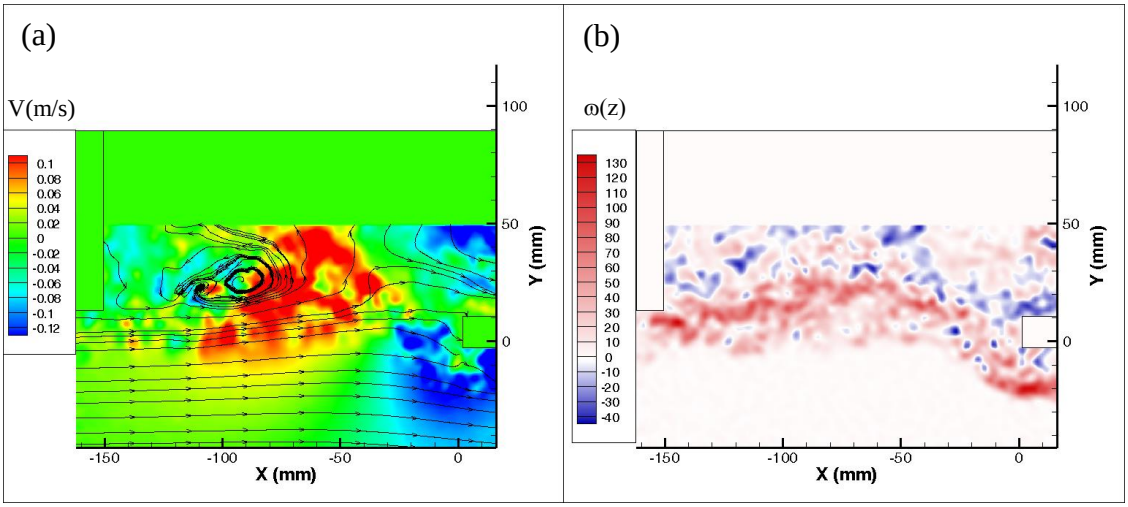

Figure 3.15: Instantaneous velocity field streamlines and [j] component contours(a) and contours of out-of-plane vorticity (b) corresponding to first hydrodynamic oscillation mode. Lc=0.69 m, Lec=0.151 m, U=0.85 m/s, Lec=0.151 m, h= 0.185 m, Lc=0.69 m.

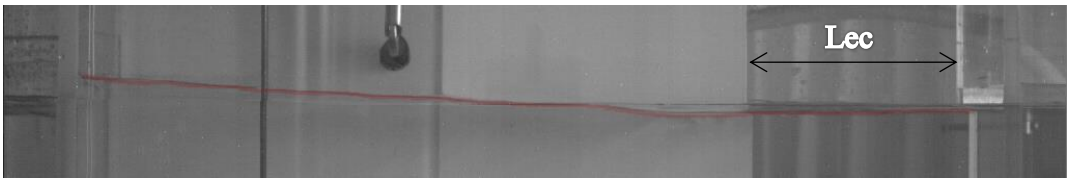

Figure 3.16: Instantaneous free-surface position corresponding to the plots shown in Fig. 3.12. Notice closed-open boundary conditions for the wave where the left cavity boundary is a wall (closed) and the right boundary occurs at the expansion across the cavity opening length that acts as a pressure reservoir (open).

Under these conditions a single, large-scale vortex is observed within the free shear layer and the free shear layer takes on a mode similar to that of a vibrating string fixed at both ends. Furthermore, the formation of large-scale vortical structures formed as a result of Kelvin-Helmholtz instability is aided by resonance and observed for deep flows just as observed for shallow flow cases [1]. However, for increasingly deeper cases these structures were less elongated in comparison to the results of the shallow investigations indicating that the depth regions of the cavity not affected by the wave my inhibit the shear layer growth. This qualitative result is logical, since as the water depth is increased and the cavity wave approaches a deep water wave condition, interaction between the shear layer, cavity floor, and cavity wave vary widely across the degree of depth.

The second hydrodynamic mode corresponds to two large-scale vortices within the cavity entrance and is associated with a second mode cavity wave. This is the most common coupling observed and was the dominant mode in cases where 3rd or 4th mode low amplitude waves were initially observed.

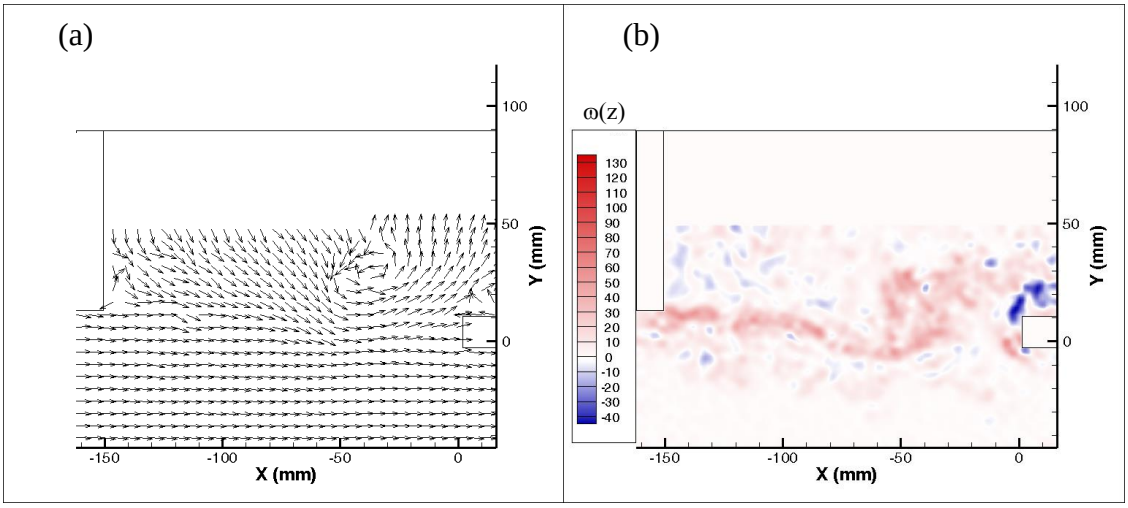

Figure 3.17: Instantaneous velocity field (a) and contours of out-of-plane vorticity (b) corresponding to the second hydrodynamic oscillation mode. U=0.43 m/s, Lec=0.155 m, h=0.167 m, Lc=0.690 m.

In Figure 3.17, a vortex can be seen convecting into the cavity region and large-scale circulation in the cavity can also be observed.

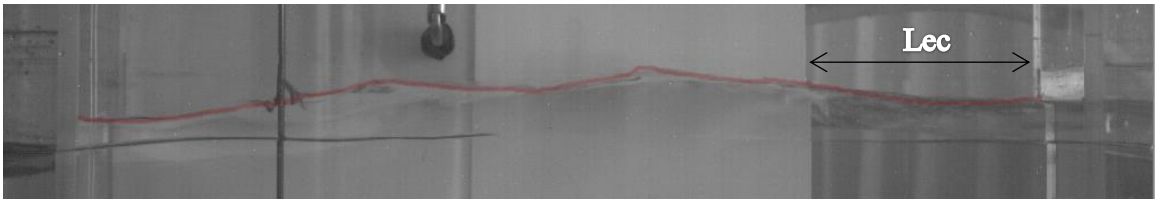

Figure 3.18: Free-surface displacement corresponding to the second hydrodynamic oscillation mode. U = 0.43 m/s, Lec = 0.155m, h=0.167 m, Lc = 0.69m.

For locked-on cases fluid injection and ejection into and out of the cavity occurs as observed by Wolfinger et al. (2012) for very shallow cases and see in the following figures for a much deeper cavity.

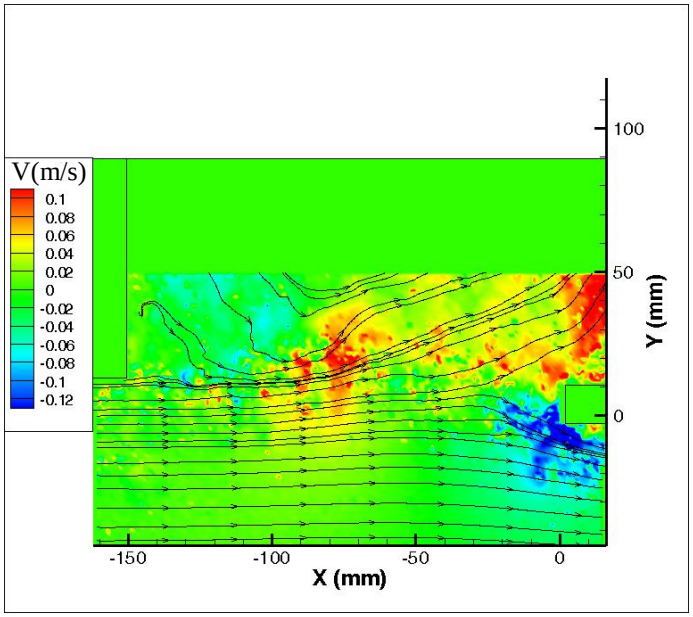

Figure 3.19: Instantaneous velocity field streamlines and [j] contours in the presence of cavity standing gravity wave showing mass exchange with cavity. U=0.43 m/s, Lec=0.151m, h=0.185 m, Lc=0.69 m.

The corresponding contour plot of the out-of-plane vorticity field follows in Figure 3.20. The location of the laser sheet used to obtain the qualitative flow images discussed in this section was fixed at 0.1135 m from the bottom of the cavity. This was necessary as

significant reflections from the free surface occurred without a sufficient offset between the laser sheet and the trough of the cavity wave.

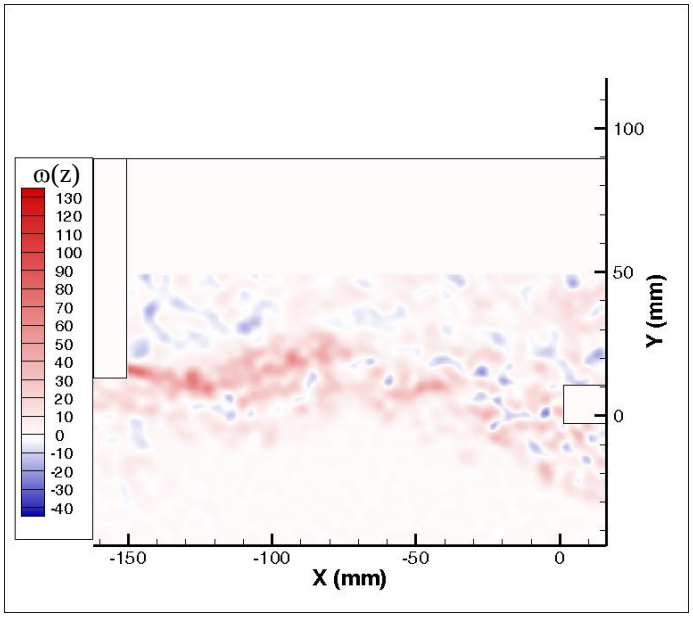

Figure 3.20: Instantaneous contours of out-of-plane vorticity in the presence of cavity standing gravity wave. U=0.43 m/s, Lec=0.151 m, h=0.185 m, Lc=0.69m.

The 1st three cavity wave modes with closed-open boundary conditions are shown in Figure 3.21 and correspond to spectral peaks of Figure 7.11. The n-th mode has n nodes and n anti-nodes. These modes were not observed consistently, as mode jumping (when the system alternates between higher and lower modes) occurred as the system was allowed to reach steady state. They do, however, correspond to the hydrodynamic mode at which they were generated in general. This correspondence is not exclusive as the interaction of different modes can cause the wave to oscillate at another mode entirely and probably due to a more favourable matching of frequencies between the modes.

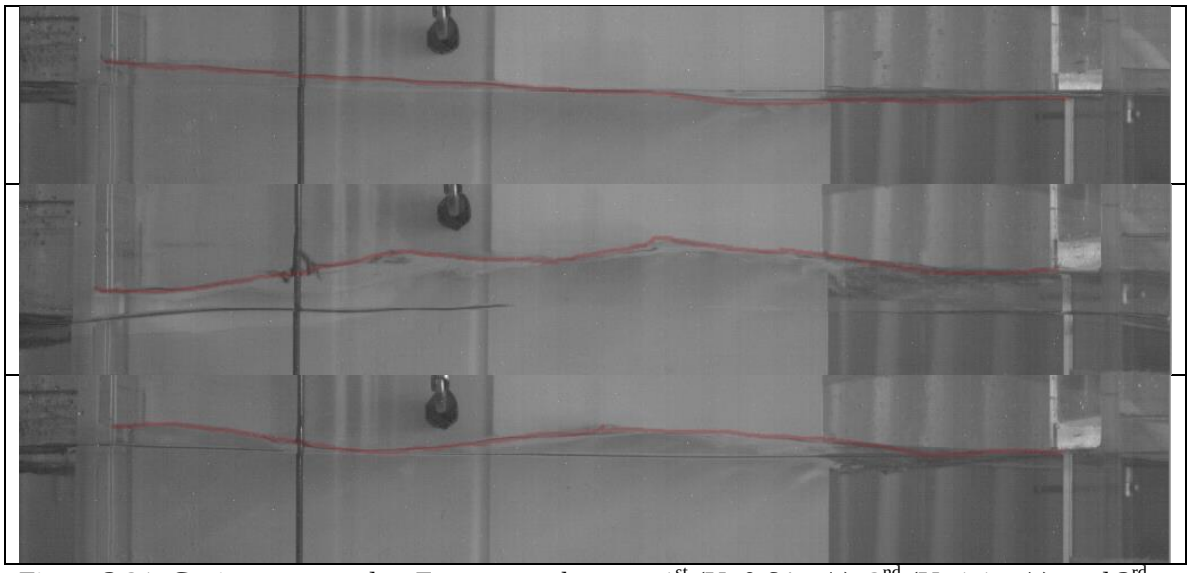

Figure 3.21: Cavity wave modes. From top to bottom: 1st (U=0.64 m/s), 2nd (U=1.1 m/s), and 3rd (U=0.85 m/s) open-closed modes. Lec=0.161 m, h=0.18 m, Lc=0.69 m.

3.5 Hysteresis and effects of added mass and tangential flow past cavity

Measured resonant frequency increased with increasing tangential flow velocity consistent with Anderson (1977) for an acoustic Helmholtz resonator in air [42]. In some cases, effective length was seen to decrease (possibly due to decreasing wavelength, although not uniformly for strongly resonant cases) and is attributed to reduced added mass at the open basin end. This was seen to occur above reduced velocities of $U_\infty/(f_R D_H)$ $\approx$ 2.5 in contrast to Anderson's value for the acoustic Helmholtz resonator of 10. However, due to the orientation of the parallel side branch resonator certain phases of the shear layer result in mean through-flow in addition to tangential flow. With the added complexities of large-scale circulation and non-linear celerity relations with increased wave amplitudes the details of this observation have been left for future work. However, increased wave celerity with larger cavity wave amplitudes and resulting frequency increases do not seem to account for significant portions of the frequency increases since both resonating and non-resonating cases followed a similar trend. This trend can be seen

in Figure 3.22 below demonstrating increased primary cavity frequency for increased velocity for a given depth.

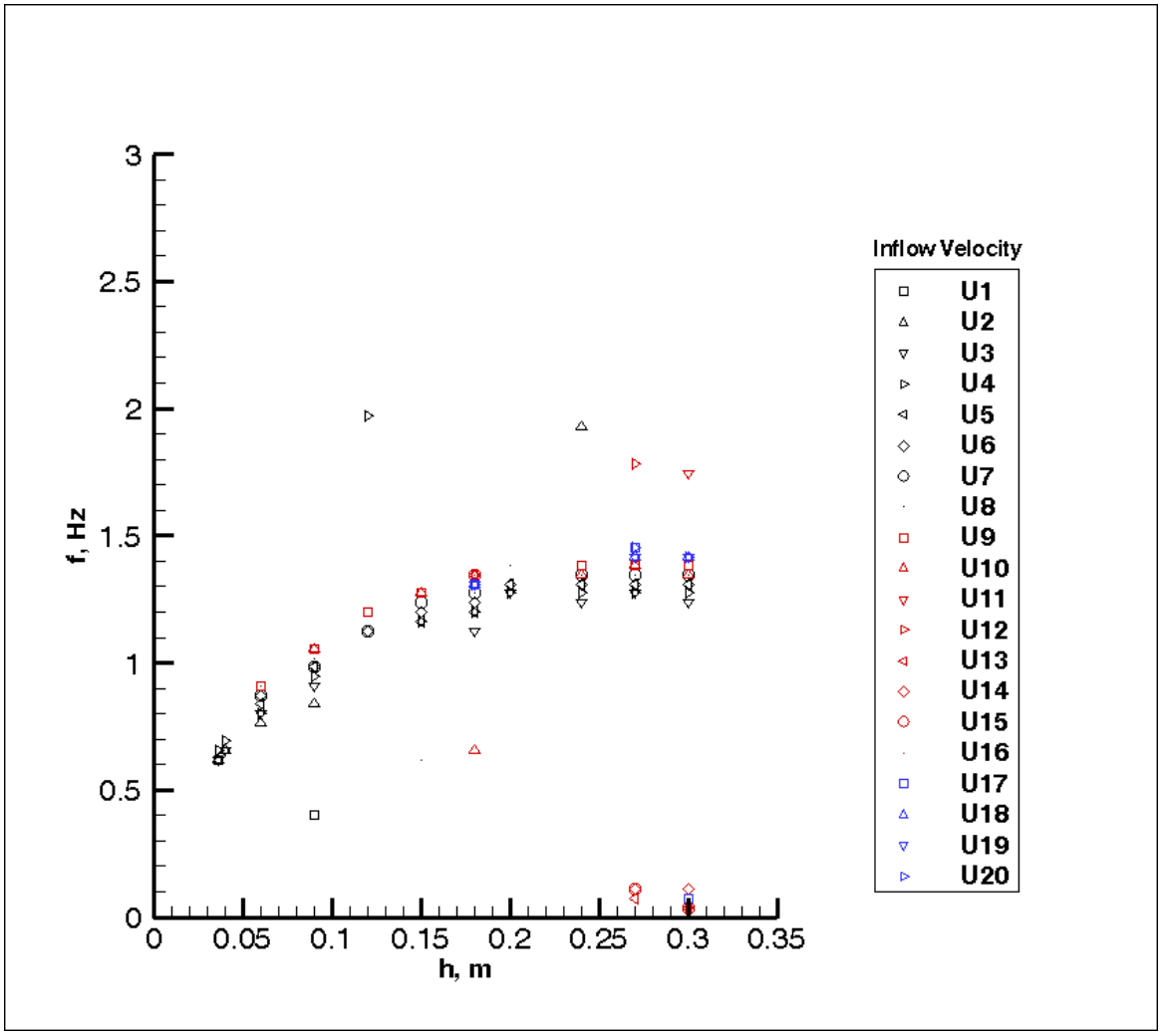

Figure 3.22: Frequency of the standing wave in the cavity as a function of cavity depth for various values inflow velocity.

The frequency increase was quantified at 0.76 Hz/m/s and was observed for all tests for which a sufficiently wide band of frequency response could be analyzed in the associated PSD plots.

Cases of hysteresis were also observed wherein resonance could be reached for a range of inflow velocities but not for the same velocities when the system was reset by blocking the cavity opening length or when the velocity was reduced to zero and then increased to

the value of interest rapidly. It was also observed that if a lower wave mode was allowed to resonate at a lower amplitude it could suddenly jump modes to a much larger amplitude. Mode jumping and hysteresis were discussed in Section 3.2 (h = 0.27 m) and are documented in Figure 3.23 showing that more complex modes are not necessarily at a lower power.

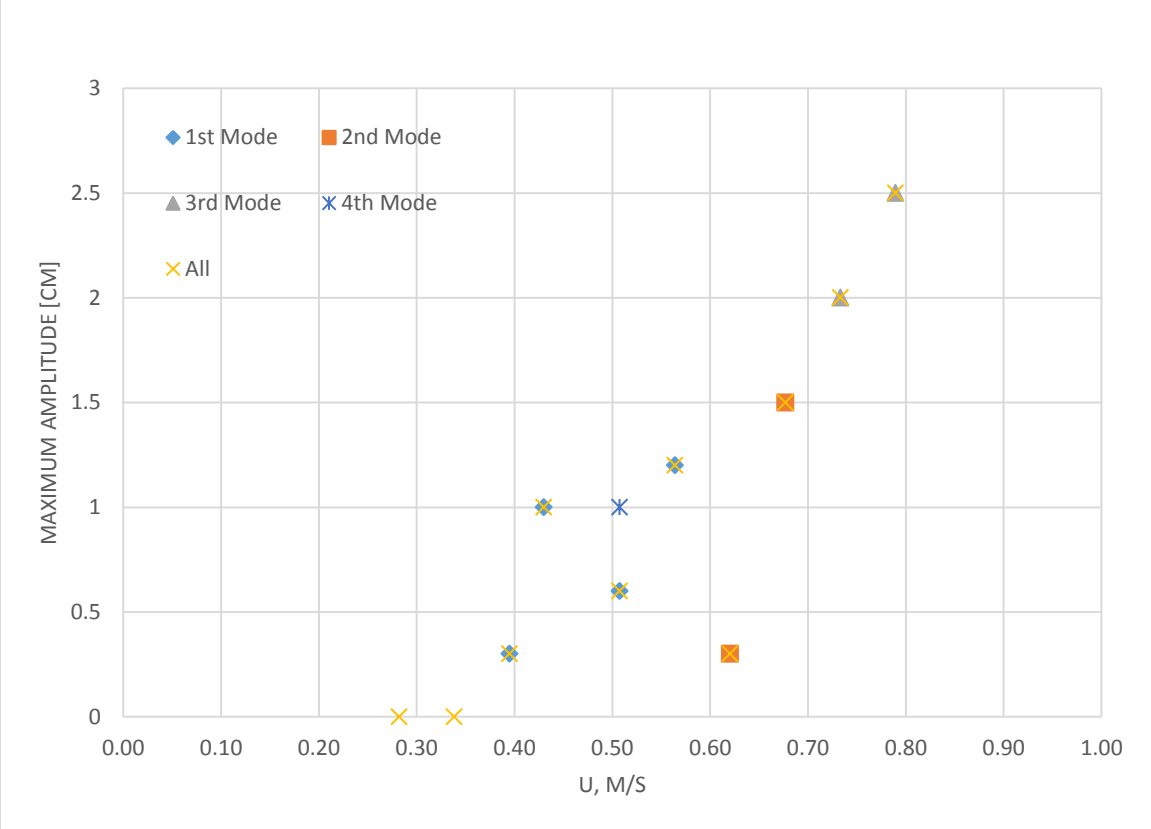

Figure 3.23: Maximum amplitude of the standing wave as a function of the inflow velocity. h = 0.185 m, L_{ec} = 0.155, L_c = 0.69 m).

Cases of hysteresis can be explained due to two primary mechanisms:

1. Decreased added mass with increasing velocity.
2. Increased frequency with large amplitudes.

These were observed for an IIE system under different conditions by Rouse, Anderson, and Worraker [28], [42], [43]. For both cases an increase in cavity wave frequency allows the system to reach the threshold for lock-on with the hydrodynamic frequency that is typically higher than that of the cavity mode or allows the system to lock-on to higher modes with increasing velocity in a continuously resonating status rather than breaking down between modes. If left for long enough the dominant interaction prevailed and eventually pulled the frequencies to lock-on in the more favorable range at the cavity mode that is most agreeable with the shear layer mode. Applications of this to an alternative energy device in which this resonance is favorable would be to jump-start the resonance by use of a plunger or other device for a number of cycles to help the frequencies lock-on. However, matching frequency by actively shortening the cavity would be more robust.

3.6 Effect of cavity opening length

Examination of the effect of cavity length was also conducted and the PSD waterfall plots along with cavity wave height have data been included. Depending on the inflow velocity a certain L_{ec} threshold had to be exceeded in order for vortex shedding to occur at a suitable frequency; this occurred for a reduced velocity of $U_\infty/(f_R L_{ec}) \approx 4.5$ The data with varying cavity length provides insight into another plane of the three dimensional surface of parameters determining hydrodynamic frequency that is a function of both inflow velocity and characteristic length for vortex shedding (L_{ec}). The data can also be used to validate the model parameters used for the hydrodynamic frequency prediction as was done for a fixed cavity opening length with varying velocity in Section 3.4.

The most insightful cases of variable entrance length data sets were for the h=0.09 m depths to h=0.27 m depths and are presented in Figure 3.24 and Figure 3.25 along with the cavity wave amplitude data.

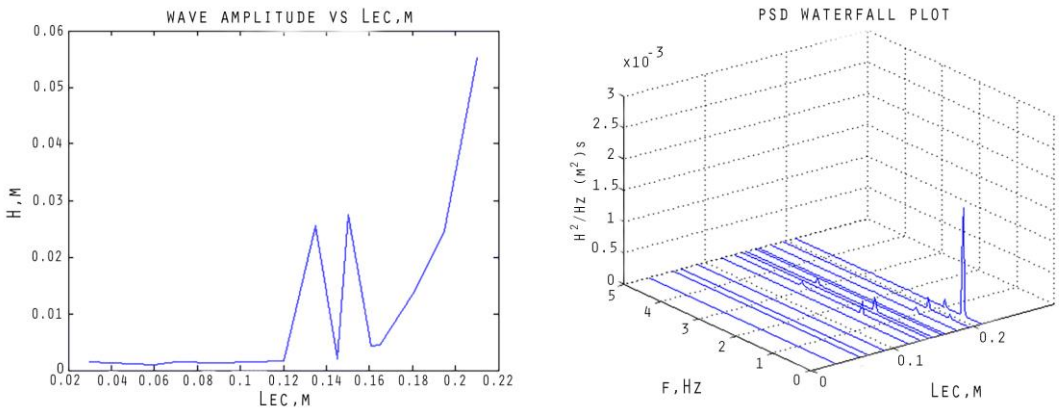

Figure 3.24: Wave height (left) and the PSD (right) as functions of the cavity opening length. h=0.09 m.

The primary cavity mode is excited for the h=0.09 m depth at a cavity opening length of 0.2 m and with depth increased to h=0.12 m the second cavity wave mode is excited. At a depth of h=0.09 m and cavity opening of 0.145 m there was no significant resonance; however, when the system was not restarted between these two data points a continuous amplitude peak could be observed but was also prone to breakdown and decay to zero amplitude.

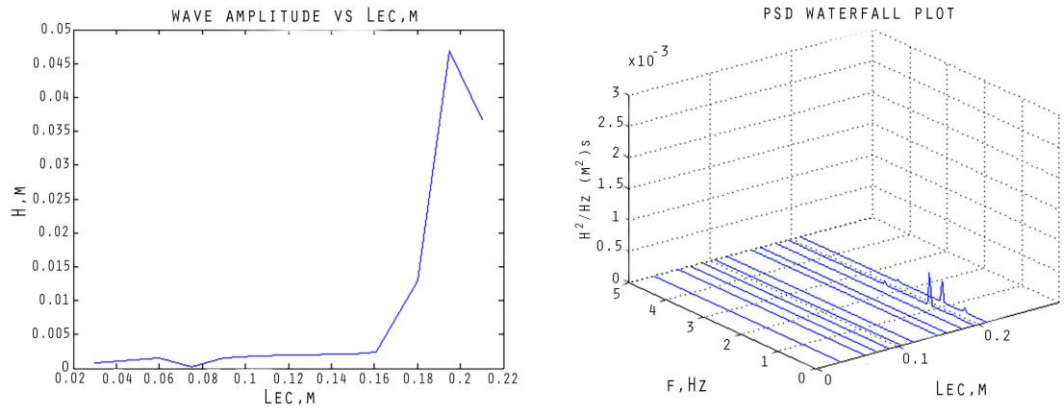

Figure 3.25: Wave height (left) and the PSD (right) as functions of the cavity opening length (h=0.12 m).

The shear layer frequency at a depth of h=0.15 m is sufficiently close to the cavity frequency and a significant wave is excited for 0.16 m< Lec <0.21 m. Maximum cavity wave frequency occurs at the first cavity wave mode in contrast to the second mode observed with the velocity sweep tests. The decrease in amplitude for the highest cavity opening length can be attributed to a less optimum matching of cavity wave frequency and hydrodynamic frequencies; such a system is less efficient at transferring energy to the cavity wave.

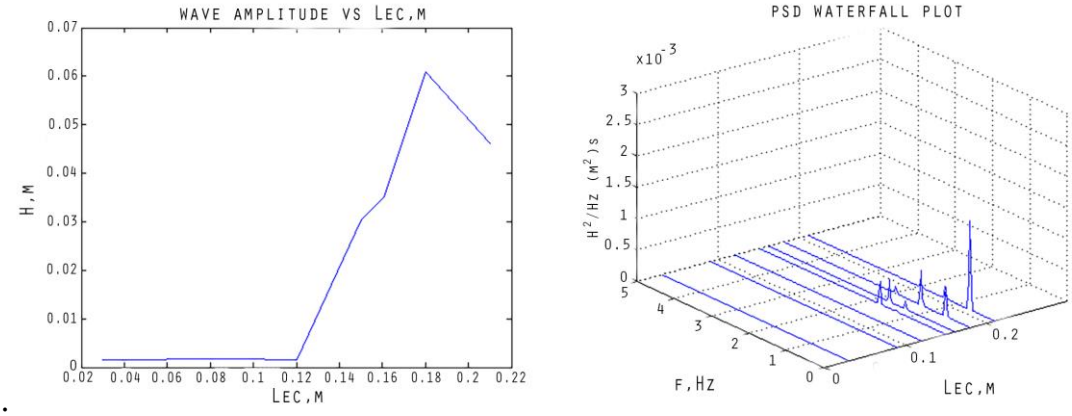

.

Figure 3.26: Wave height (left) and the PSD (right) as functions of the cavity opening length (h=0.15 m).

Dual mode excitation is observed for the h=0.15 m and h=0.18 m cases and is consistent with the results from the velocity sweep along with the excitation of lateral cavity modes.

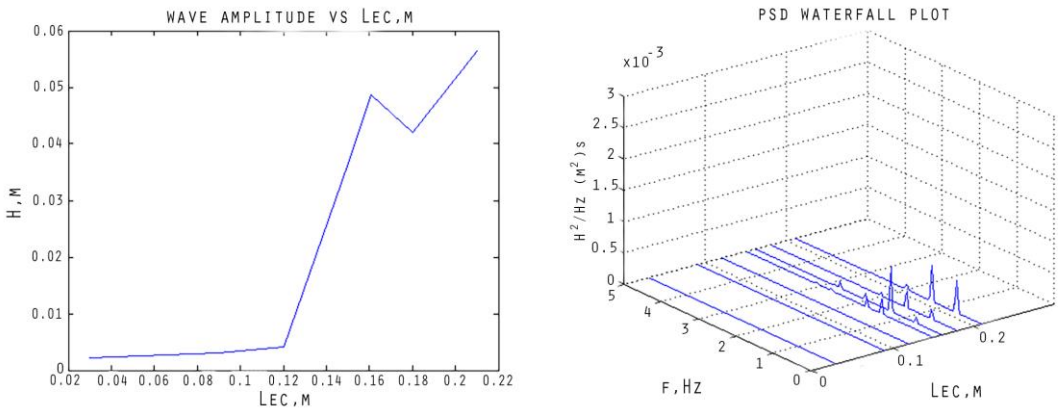

Figure 3.27: Wave height (left) and the PSD (right) as functions of the cavity opening length (h=0.18 m).

The 0.20 m depth also results in significant cavity wave amplitude and clearly shows the frequency response of the cavity with a dual mode excitation. This can be explained since the parameters affecting the hydrodynamic frequency are such that mode jumping between Strouhal modes occurs due to the frequency shifting effect of the cavity wave. The largest peak which occurs at the primary cavity frequency is not predicted by one of the hydrodynamic modes and may be attributed the effects of radiation that were observed for large cavity opening lengths.

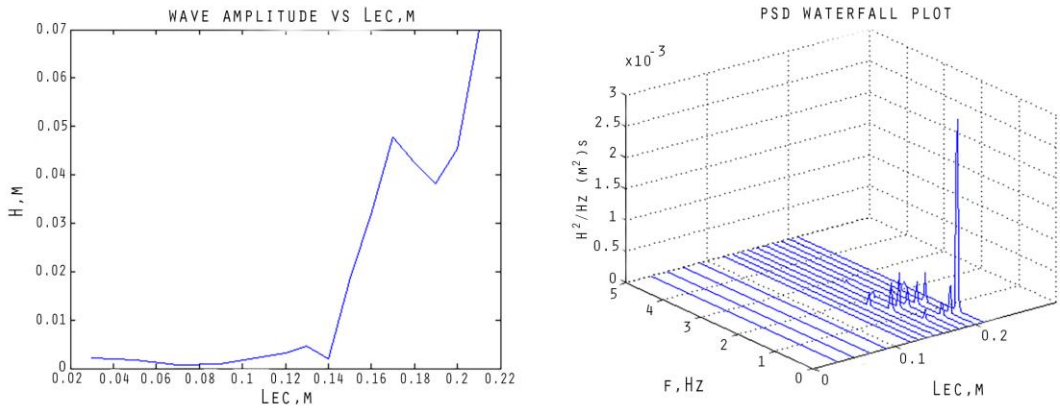

Figure 3.28: Wave height (left) and the PSD (right) as functions of the cavity opening length (h=0.20 m).

When the depth is increased further to h=0.24 m an interaction between the primary hydrodynamic mode and secondary cavity mode is dominant with the trend continuing for the h=0.27 m test as seen in Figure 3.29 and Figure 3.30.

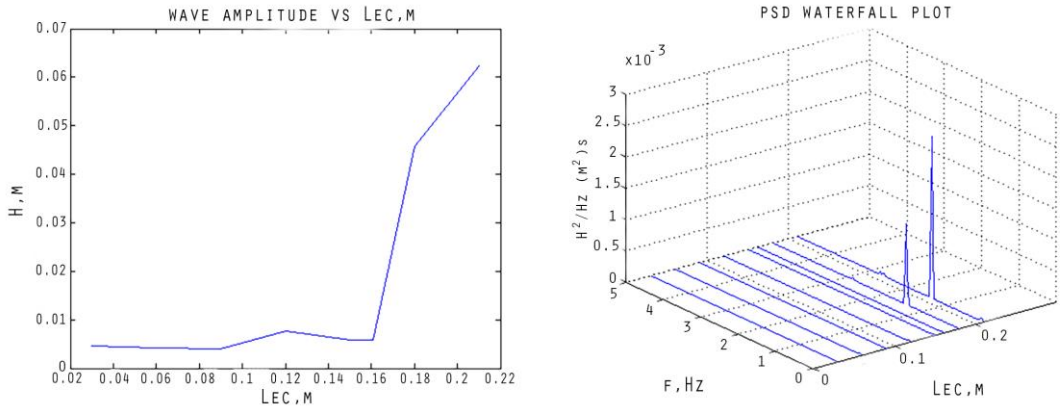

Figure 3.29: Wave height (left) and the PSD (right) as functions of the cavity opening length (h=0.24 m).

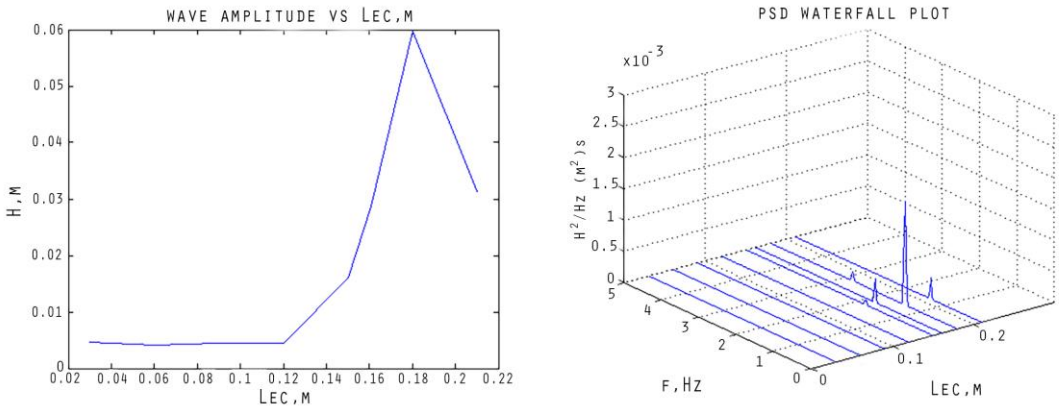

Figure 3.30: Wave height (left) and the PSD (right) as functions of the cavity opening length (h=0.27 m).

Error associated with hydrodynamic frequency prediction

The hydrodynamic frequency prediction model (Equation 3.5) is valid for variation of L_{ec}, as it was for the inflow velocity variation as would be expected from the physics describing vortex shedding frequency. Nevertheless, this result provides support for the proposed model and parameters. With the exception of the h=0.20 m case the 1st mode was predicted within 2% of the spectral peak and the 2nd mode was within 6% of the spectral peak with no interaction with the 3rd mode for comparison.

3.7 Cavity wave absorber and wave energy

A number of interesting observations were made during experimental study of the resonant coupling in the presence of a wave maker/absorber. For cases where the shear layer energy contributions to the wave were dominant, an IIE case, the cavity wave wavelength was as predicted by the $L_{c,eff}$ model. However, when contributions from the piston were greater EIE became dominant and the wavelength shifted. Comparison of data collected from running the wave generator with and without flow shows that there is a significant coupling between the shear layer and cavity wave in terms of the motion of the piston. Furthermore, EIE cases showed poor statistical data in terms of recorded wave

heights and calculated phase shifts show that in some cases the piston wave interacts destructively with the resonant cavity wave.

To determine the effect of a wave absorber on a locked-on system a piston was introduced into the cavity. Since the piston face translates the cavity geometry changes instantaneously but was fixed by a mean position measurement equivalent to L_c=0.516 m. Depths of 0.185 m and 0.102 m were investigated and piston frequency was matched to the locked-on frequency of the system obtained by tuning the system with the piston face fixed. The peak lock-on frequencies were determined to be 1.538 Hz and 1.384 Hz respectively for the 0.185 m and 0.102 m depths and were verified again after completion of the tests to ensure repeatability of the test. During each test the stroke of the piston S was varied while keeping the mean cavity length constant. A ramp-up procedure of ten cycles was implemented to allow the system to reach the mean cavity length operation point from each unique starting position. The measured wave height was obtained from wave gauge data recorded for each stroke test and is summarized in Figure 3.31 below.

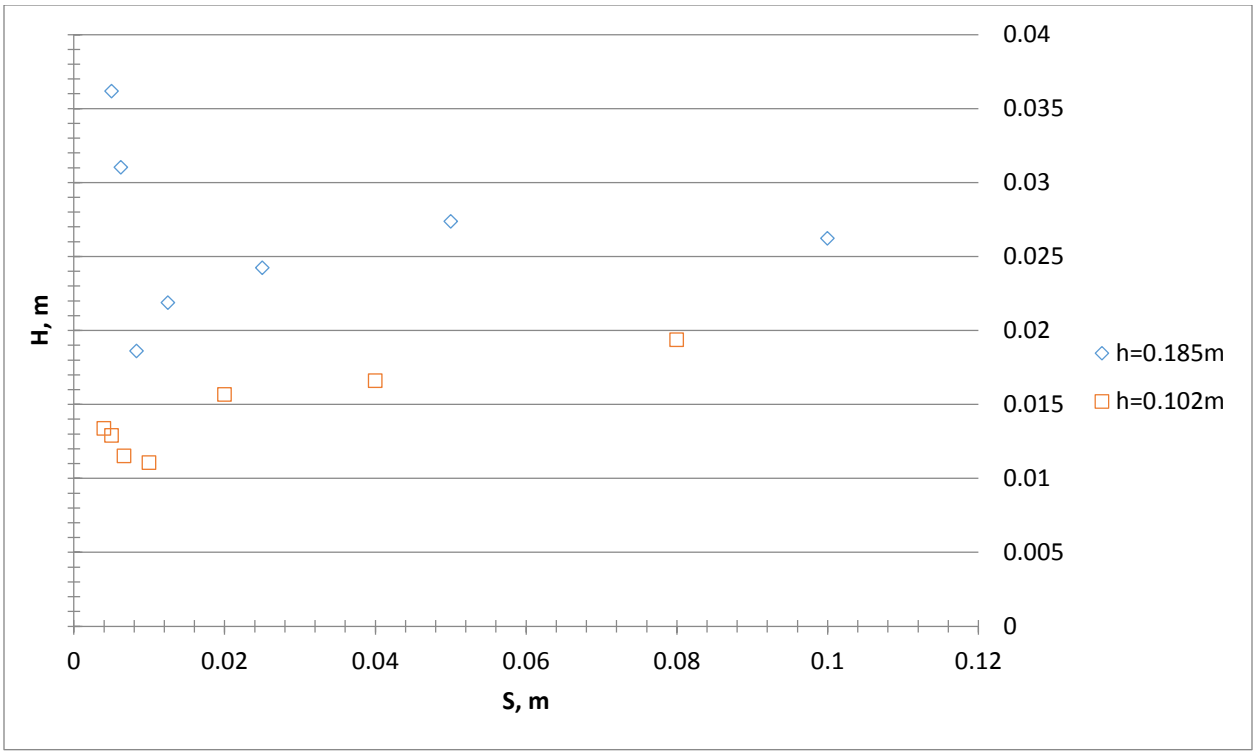

Figure 3.31: Cavity wave height (H) as a function of piston stroke (S). U = 0.92 m/s at h = 0.185 m and U = 0.96 m/s at h = 0.102 m.

The wavenumber is given as $k_h=2*\pi/\lambda$ or 12.6 rad/m and the values of $k_h h$ are therefore 1.28 and 2.32 for the 0.102 m and 0.185 m tests respectively. According to Dalrymple this corresponds to an H/S ratio of approximately 0.6 and 1 respectively [18]. A larger stroke is therefore required to generate a given wave amplitude at a shallower depth than for the same amplitude to be generated at a deeper depth. For the same frequency then more power would be required at the shallower depth to generate the same wave height. Conversely, more energy will be absorbed by a wave absorber at a shallower depth for the same stroke. In this case however, the frequencies are not identical and since the cavity is open to the channel the H/S ratios are less split than predicted by theory and comparison of the wave maker power shows that for a given stroke the shallower depth requires less power.

As expected, for large values of piston stroke, net energy was contributed to the cavity wave from the piston as seen in the results for cases where S>H for the 0.185 m case. Likewise, below a threshold the wave amplitude was greater than that of the stroke and H>S. Wave amplitude was smallest for a stroke of 1.1 cm and 1.86 cm for the 0.102 m and 0.185 m cases. One explanation for these minima is that energy extraction is occurring at the most efficient parameters for the given case: the energy required to move the piston over a cycle of motion is matched most closely with the energy input into the system via the shear layer over a wave cycle. The effect of moving the piston a stroke less than this amount means that energy will build up in the wave since it is being added at the resonant frequency of the system: this is seen in an increased wave amplitude. The limit of this amplitude is due to an increasing visco-thermal dampening loss that eventually matches the energy transferred from the mean flow to the gravity wave via the shear layer oscillations.

The position of the piston throughout the motion was recorded using the servo-drive interface and used along with the load cell data to give power readings. While there was a large amount of frictional and inertial resistance on the motion of the piston net power was generated for the three smallest piston stroke tests for the 0.102 m test and the smallest piston stroke of the 0.185 m test. This can be visualized by the data in the next figure.

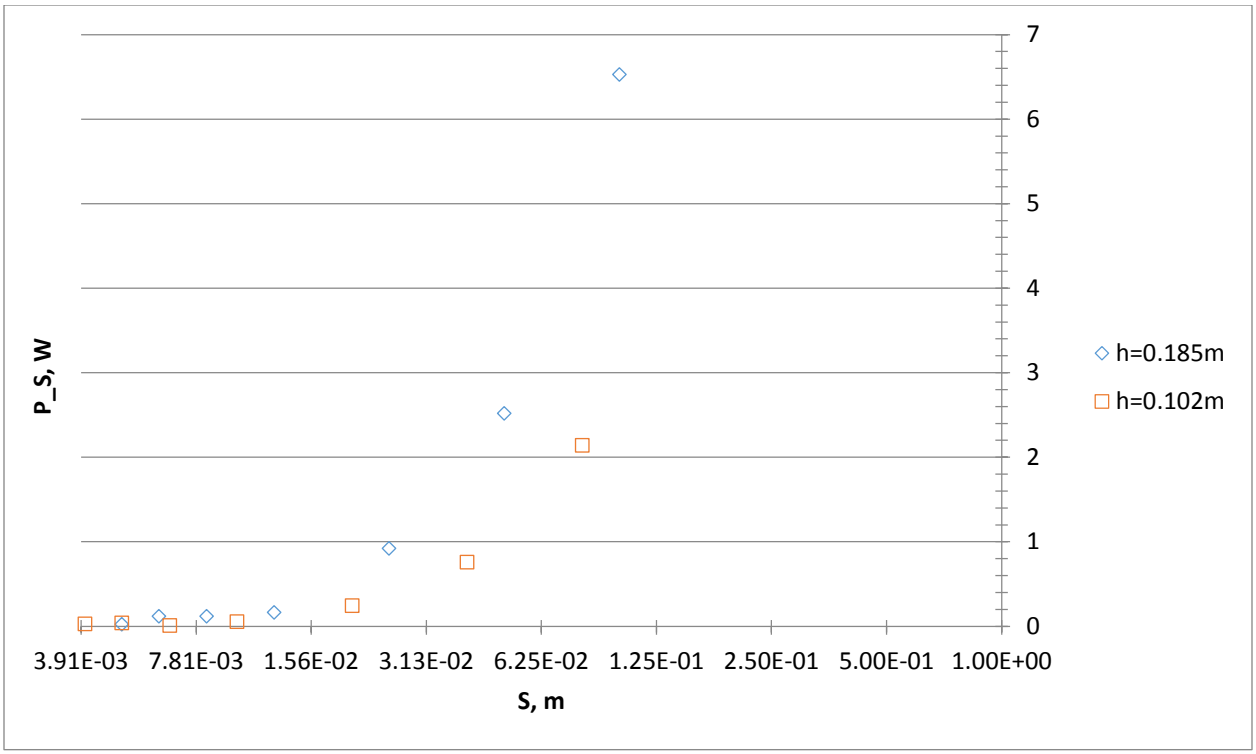

Figure 3.32: Wave maker power as function of piston stroke length (U=0.92 m/s at h=0.185 m, U=0.96 m/s at h=0.102 m).

The offset in the point where the 0.102 m case uses close to zero power before the 0.185 m case in terms of stroke length may indicate that the shallower depth is more efficient. This offset is also seen in Figure 3.31 in terms of the local minima occurring at a higher value of piston stroke. It can be seen in Figure 3.31, as previously presented, that the wave present in the 0.185 m case without piston motion is much larger than that of the 0.102 m case.

3.7.1 Effect of depth on wave energy absorption

With increasing cavity depth, it would be expected that piston-type wave absorbers would become less efficient taking the path of the water particles into consideration with the definition of deep and shallow water waves. Examination of Figure 3.32 shows that greater power was required to drive the piston for the deeper test case. However, the

parameters for peak resonance obtained at 0.92 m/s case at the h=0.185 m depth and 0.96 m/s for the h=0.102 m depth and frequencies of 1.538 Hz and 1.384 Hz indicate that in terms of energy contributions from the shear layer the deeper case would be expected to be more powerful. This is supported by the larger wave height observed from the deeper case with small piston motion in Figure 3.31 and the measured wave of H=0.053 m in comparison to H=0.041 m with no piston motion. Qualitative analysis of the vortex path during piston motion shows that the impingement vortices are much more uniform with depth: the three-dimensional effects discussed in section 3.4 have been reduced and the problem becomes more two-dimensional. This was observed for both the vortex near the impingement plate and at the leading edge of the cavity while the latter is not definitive. This coupling of the piston motion with the shear layer organization effectively shifts the hydrodynamic frequency while forcing a given cavity wave frequency and may in some cases have a positive or negative effect on the resonant coupling. It was observed that for some tests more power was required to generate a given wave in a system with resonant coupling than for cases where resonant coupling was not occurring. On the other hand, small piston strokes could help the system lock-on to resonant coupling, decrease the time required to reach steady state operation, or act as a buffer to keep the system locked-on for variable inflow conditions.

3.7.2 Effect of piston stroke on phase and mode of excitement

The motion of the piston had an effect on system power and this was subsequently seen in the mode of excitement of the cavity wave. For cases where energy contributed by the piston was greater than that of the shear-layer contribution over the cycle, the face of the piston acted as a node and the wave crests and troughs oscillated with the motion

of the piston. For cases where the shear-layer contribution dominated the piston face acted as an anti-node as was observed with all test cases without piston motion. As the piston stroke was increased past the optimum value (when stroke corresponds to minimum cavity wave height) the piston motion and cavity wave became out-of phase. This is due to the change in primary mode of excitement from instability-induced excitation (IIE) to movement-induced excitation (MIE) and the subsequent change in effective cavity length that occurs with the MIE case favoring the closed-closed boundary conditions and thus differing cavity frequency in comparison with that of the closed-open conditions occurring with the IIE cases. This phase shift was observed both in terms of a phase angle calculated from the shift in wavelength and in the poor statistical quality of the data collected at large strokes due to a large phase shift and the effects of standing waves setup by a mismatch between piston and wave motion [18]. Since there is resonant coupling between the oscillating shear layer and cavity wave the vortex shedding is affected and interactions detrimental to the IIE resonance can occur. Fluid is expelled from the cavity to the main flow at the leading edge and the reverse is true at the trailing edge of the cavity as also observed by Wolfinger et al for shallow cases [2]. It would be logical to assume then that if the cavity wave is larger than that which would naturally occur due to the resonance the frequency of vortex shedding would be affected. This was qualitatively observed by examining free surface undulations caused by vortices along with entrained air bubbles and is perhaps due to separation of rolled up vortices on the leading edge of the cavity when fluid is expelled here by the cavity wave. This change in frequency would result in a phase difference between the cavity wave and piston motion as observed. The conclusion is that complex coupling is present since vortex shedding

occurs at points of minimal hydrostatic pressure, as also mentioned by Dequand et al [13], which is subsequently dependant on the wave and coupled with the motion of the piston.

3.7.3 Max energy flux from system before resonant breakdown occurs

Initially, it was expected that after removing a threshold amount of energy greater than the net energy flux transported to the cavity wave from the free stream flow over a given cycle resonant coupling would break down. This was based on the results of acoustically analogous cases and the observation that coupling was very sensitive. This sensitivity was seen when for the range of test cases investigated simply inserting a small plate across the cavity gap would cause the wave height to decay immediately and break down the coupling. It was then expected that such a sensitive system would not be robust enough to maintain resonant coupling in such an extreme case as a moving boundary. However, flow visualization data clearly shows that the location of impingement of the convecting vortices is critical in that if impingement occurs at a point that is not bounded downstream by a wall (i.e. at some structure at the midpoint along the cavity entrance rather than at the impingement plate) the nature of the influx and expulsion of the fluid is altered [2]. It would follow then that perhaps the insertion of the plate at the midpoint of the cavity entrance would affect the coupling as a more extreme case than that of a moving boundary would. From the case of the wave absorber it was demonstrated that values of piston stroke that would otherwise produce waves greater than the amplitude of the resonant cavity wave resulted in a nodal inversion as seen in Figure 3.33 below.

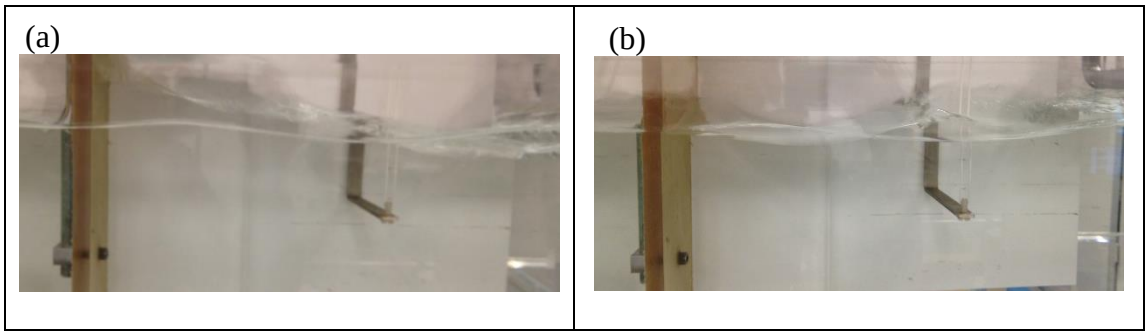

Figure 3.33: Nodal boundaries for a) IIE and b) MIE dominant cases.

When the piston stroke contributes more energy to the cavity wave over a cycle than the shear layer does a form of movement-induced excitation may exist. While the system is an instability-induced excitation of a fluid oscillator the hysteretic nature of the nodal inversion is more suggestive of an MIE case [22]. If MIE by definition ceases when body motion stops and positive energy contribution to the body occurs over the cycle two qualitative observations can support a hybrid MIE-IIE case:

1. If piston motion dominates the energy transfer than it can no longer be argued that the impinging shed vortices are the primary excitation method: although IIE with modified vortex shedding occurs due to body motion, this motion is the dominant energy contribution.
2. The nodal inversion, that affects flow patterns dependant on body motion ceases when the body motion is taken away or is not large enough to be the dominant energy contributor.

Since having piston motion as a primary energy contributor also indicates that the body cannot obtain a net positive energy contribution the inherently IIE case is most accurate but with an interesting aspect in that nodal inversion occurs and affects the vortex shedding.

Since the resonance does not break down with large piston motion (bordering on MIE) it would be expected that the vortical structure would be modified in comparison to small piston stroke or zero piston stroke cases. The resonant status between the shear layer and cavity wave is indicated by the observation of no decay in wave height and a measured wave height greater than that predicted for the wave generated by purely the piston stroke. Future work could quantify this by examining the nature of the vortical flow structures under the above conditions.

3.7.4 Wave power analysis

Based on the maximum cavity waves observed of H=0.041 m for the h=0.102 m and H=0.053 m for the h=0.185 m case the wave energy flux can be estimated. An intermediate water wave classification is obtained for the h=0.102 m depth since $h/\lambda=0.37<0.5$ and requires the use of the intermediate wave celerity relation of Section 1.6.6. The measured wavelength of 0.275 m for the h=0.185 m case is within -12% of the wavelength predicted using the effective cavity length and hydraulic diameter. For the 0.102 m case the wavelength is only predicted within -3% of the model. The h=0.185 m case is classified as a deep water wave and the appropriate celerity relation must be used as presented in Section 1.6.6.When the power contribution from the piston becomes greater than that of the IIE source the cavity is excited simply by $L_{eff}=L_c-L_{ec}$ with closed-closed end conditions. The expansion to the main channel has little effect on the added mass since the wave is generated across the entire face of the piston rather than in the vicinity of the impingement plate as for the IIE case. The wavelength of the second mode is predicted at 0.349 m by the theoretical model and is associated with an error of -1.7% in comparison to the measured 0.355 m wavelength acquired during the experiment at

h=0.102 m. For the 0.185 m case an error of 10% is associated with the model in comparison to the measured wavelength of 0.316 m.

The measured wave height of 0.0186 m for 0.185 m case shows a wave height difference of 0.0344 m in comparison to a wave height of 0.053 m obtained during resonance without the wave absorber. The net wave energy flux associated between these two values is found to be 1.48 W/m and represents the upper limit on wave energy absorption. In reality, energy flux to additional radiative losses due to the presence of the absorber and destructive interference of the shear layer with standing wave modes generated by phase shifts between the wave absorber and incident wave will reduce this quantity. Additional losses will occur in the actual conversion of the wave energy into electrical energy of a usable frequency as well. In the same way, a maximum wave energy flux for the 0.102 m case of 1.04 W/m is associated with the 0.0111 m wave in comparison to the initial 0.041 m wave. Based on the wave area of the cavity of 4.44E-2 m^2 using the cavity width and enclosed cavity length the current system produced 114.9 mW at the 0.185 m depth and 69.1 mW at a depth of 0.102 m in terms of net power contribution to the wave absorber. (22-18% efficiency approximately)

3.7.5 Comments on design for energy harvesting

Due to the high level of system losses in the linear table and the strong coupling between piston motion and shear layer organization it can be seen that use of the current system as an energy harvester is not practical. As mentioned, for deeper flows paddle-type wave absorbers work more efficiently than piston types. However, paddle-type absorbers may be best suited for use with magnetic damping systems. The viability of these systems has been demonstrated by Abiru and Yoshitake for an energy harvesting application with a

flapping foil [44]. A bank of permanent magnets could be fixed above a copper plate and used as a magnetic damper in parallel with a spring or oppositely coupled wave on the reverse side of the paddle. The damping coefficient could be matched to the parameters of the resonant system to extract energy from the flow without causing breakdown.

For a paddle or piston configuration a dual-source prototype could be constructed to allow the cavity wave to be excited simultaneously by shear layers on either side of the cavity a wider cavity width could be employed. Given a wave energy of 5.18 W/m^2 with a cavity width of 0.250 m, considered reasonable as it is double the result calculated for the single source system, there would be a potential to extract 480 mW from such a system. While additional added mass may play a negative role on the system itself, the friction and resistance in the system is not expected to double with twice the piston face. Perhaps even a quad-source configuration could be built that would produce standing waves on the back side of the same pistons at an appropriate phase shift. However, even with a high efficiency for electrical conversion unless resonance of a similar degree and frequency can be obtained for wider and longer cavities the application of such an energy harvester is likely limited to the powering of instrumentation such as fish counters, flow meters, or wave gauges. Investigations on a downstream series of resonators showed promising results in that the individual waves were in-phase and that the excitation was globally organized [5]. Up-scaling the system in terms of geometry in contrast to setting up an array of systems is not an unreasonable option as resonant free surface oscillations can occur at an immense scale. Depth is not as critical since after deep water wave conditions occur the frequency of the wave is determined by the length of the cavity with natural frequency decreasing with larger cavity lengths. Since the frequency of vortex

shedding increases with increasing inflow velocity it may be necessary to couple higher cavity wave modes if inflow velocity and cavity length are to be scaled together. In most cases it is likely that area of the cavity would be increased rather than increasing inflow velocity and this presents are more difficult problem. As cavity width is increased the wave will become more three-dimensional and the likelihood of exciting lateral modes increases. In addition, visco-thermal dampening also increases and must be considered. The path of the vortex and therefore the pressure disturbances across the cavity opening may also be altered which may make lock-on more difficult. The inflow conditions, such as the boundary layer thickness at the leading edge, could be controlled by the upstream geometry. If the entire system geometry is scaled and the inflow velocity is increased this results in the formation of large scale vortical structures that can form naturally in tidal and river flows [45]. The extent of the free surface profile dip at the centre of the vortex is proportional to the square of the radius of the vortex: a larger vortex will result in a larger free surface dip. Since this dip was observed to be proportional to the amplitude of the initial cavity wave at the onset of lock-on it is expected that even larger amplitude resonant waves could exist for larger systems. However, since a longer cavity length results in lower natural frequency it may be necessary for lock-on to occur at the higher cavity wave mode in order for lock-on with a hydrodynamic mode to occur. It may be necessary to excite the system mechanically during start up to allow the organization of shear layer structures that are coupled with the desired cavity wave frequency.

4 Conclusions

Experimental investigation of a wave cavity resonator was conducted to determine predictive models of system parameters and evaluate the performance of the system as an energy harvesting device. Based on the quantitative and qualitative results of the investigation it has been shown that a highly complex coupling between the shear layer and cavity wave occurs. This coupling is extremely sensitive to perturbations within the free shear layer and may take time to develop to a steady state of operation and in some cases will jump between modes. Hysteresis in the system can be observed as a widened range of inflow velocities at which a wave is excited or by mode jumping between PSD peaks between which resonance would break down. This hysteresis is due to the effect of wave amplitude on the wave celerity and therefore frequency of the wave, particularly for higher cavity wave modes in addition to the effects of tangential flow on the cavity frequency. This increase in frequency was quantified as 0.76 Hz per m/s and appears to occur for reduced velocities above ≈2.5 but needs confirming as this is near the low end of the capability of the flow facility. For fixed inflow velocity and variation of cavity opening length a reduced velocity threshold for resonance of ≈4.5 was observed

Predicting the effective length of the cavity and wavelength showed that open-closed boundary conditions provided the most accurate results in comparison to experimental measurements. The length of the cavity was found to correlate with the enclosed region of the cavity only, that is $L_{cavity} = L_{total\ cavity} - L_{cavity\ entrance}$, and the effective cavity length based on this dimension was determined from modifications to an acoustical model by Alster where the hydraulic diameter of the cavity based on the cavity width and depth was used. Using results for the entrance length variation tests it was shown that the

hydraulic diameter was indeed based on the cavity width rather than the entrance length: the parallel side branch WCR system behaves essentially as a coaxial side branch.

Prediction of the hydrodynamic frequency was achieved using a model similar to that presented by Rossiter for use with acoustically coupled systems and model parameters were found that match experimental results across the range of system tests. Exceptions to this include unexplained low frequency PSD peaks for two cases and slightly modified second mode parameters for the two deepest cases. The predicted frequencies matched experimental data well for variation of inflow velocity and variation of cavity opening length: two critical system dimensions. Flow field data obtained from PIV techniques and qualitative free surface results obtained from free surface video tracking show that the cavity wave mode is highly dependent on the hydrodynamic mode; however mis-matching of modes is was also observed leading to alternative vortex paths and waveforms. Three dimensional effects in the shear layer attributed to the nature of deep water waves were observed for increasing depths.

Maximum efficiency of a piston-WCR system was achieved near similar values of piston stroke for depths of 0.102 m and 0.185 m but additional coupling of the resonant mechanisms with the piston motion show the system is much more complex. In some cases resonance was strengthened by the piston motion and in other cases the system became out of phase. An IIE case dominated when shear layer energy contributions were dominant and an MIE case occurred when wave generator energy contributions dominated. The MIE case is associated with a phase shift and change to closed-closed boundary conditions using a different effective cavity length. Cases where IIE was dominant still corresponded to open-closed boundary conditions as for the regular tests

where a wave absorber/generator was not used but the effective length did not correspond as well as in the general cases and is attributed to the additional coupling and elimination of the three dimensional effects on the shear layer.

A maximum wave energy flux of 1.48 W/m and 1.04 W/m were measured at the optimum stroke conditions of 1.86 cm and 1.10 cm for the 0.185 m and 0.102 m depths respectively. Total power contribution for these cases based on the geometry of the tested system were 114.9 mW for the 0.185 m depth and 69.1 mW for the 0.102 m depth. It is possible that a dual-source configuration could provide 480 mW and the possibility of a quad-source configuration could bring this to the order of 1 W. However, energy losses in the conversion to more utilized power would reduce this figure. A magnetic damper system may be more suitable due to the high energy losses of the current system. Nevertheless, the piston system has provided insight into the effects of the added coupling and potential of the WCR as an energy harvester. Despite this, unless very large scale prototypes can be implemented the operation of such an energy harvester is likely limited to the powering of small instrumentation equipment. This novel device is however a step in the right direction in terms of exploring alternative energy sources for future power generation; in addition, up-scaling the system is not unreasonable.

4.1 Recommendations for future work

While not completed in the work of this thesis future research efforts could focus on developing predictive model of wave power based on shear layer analysis. This would provide a valuable tool for the design and study of future WCR prototypes and has been done previously to predict acoustic source power in analogous acoustically coupled

systems [13]. Similar to an acoustic system the particle velocity replaces the acoustic velocity to predict time-averaged source power over one period:

$$\langle P_{source} \rangle = -\rho_o \int_V^{\cdot} (\underline{w} \times \underline{v}) \cdot \underline{u}'_w dV. \quad (4.1)$$

For a two-dimensional shallow case $\omega_x = \omega_y = 0$ and ω_z can be adapted from Dequand et al as:

$$\omega_z = \Gamma_n(t)\delta(x - x_\Gamma(t))\delta(y - y_\Gamma(t)), \quad (4.2)$$

where the circulation at a given time is $\Gamma_n(t) \approx 0.5 U_\infty^2 g_n(t)$ with $g_n(t)$ being a function of the Heaviside function [13]. The term $x_\Gamma(t) = U_\Gamma(t - t_n)$ and approximation $U_\Gamma \approx 0.4U_\infty(t - t_n)$ with $t_n = (n-1)T$ are also given by the result of Dequand et al with T representing the period and n the nth vortex. Unlike the acoustic case however, the quantity undergoing integration in Equation 4.1 has a non-zero wave velocity in the y-direction and is coupled with the motion of the shear layer during vortex shedding. The source power is given by the same equation used to predict wave energy flux for the wave absorber and the group velocities can be determined from the wave celerity relation appropriate for the water wave depth relationship. The wavenumber required in the deep group velocity formula can be estimated from the predicted wavelength using the results of this thesis leaving only the wave height term unsolved. Correlating the time-averaged PIV data with the final equation using the substitutions outlined above would allow the wave height and subsequently the wave energy flux to be predicted.

Future work into the possible scaling of the WCR to produce larger wave amplitudes could be conducted. For example, at a depth of 2.5 m an amplitude of 0.5 m could be obtained scaling the wave amplitude with depth. For a cavity with effective length calculated using the models of this this thesis a frequency of 0.7 Hz would be obtained

with a cavity area of 1.54 m^2. For a measured Strouhal number of 0.33, obtainable by design of the upstream geometry and possibly active boundary control mechanisms, the cavity wave and hydrodynamic frequencies would match for an inflow velocity of U_∞ = 1.66 m/s. Using the same approach as for the results in this thesis a wave energy of 341 W/m^2 could be obtained for a single-source configuration corresponding to a potential 0.525 kW. With potentially less of an environmental impact in comparison to tidal turbines there is some potential for power generation but at a much lower yield in comparison to a tidal turbine. Future work to predict source power based on flow field data would therefore be valuable in evaluating the feasibility of this example configuration.

Bibliography

[1] A. Ekmekci and D. Rockwell. Oscillation of shallow flow past a cavity: Resonant coupling with a gravity wave. *Journal of Fluids and Structures*, vol. 23 (6), no. p. 809-838, 2007.

[2] M. Wolfinger, C.A. Ozen, and D. Rockwell, "Shallow flow past a cavity: Coupling with a standing gravity wave," *AIP Physics of Fluids,* vol. 24 (10), no. doi: 10.1063/1.4761829, 2012.

[3] B.A. Tuna, E. Tinar, and D. Rockwell, "Shallow flow past a cavity: globally coupled oscillations as a function of depth, "Experiments in Fluids, vol. 54 (10), no. doi: 10.1007/s00348-013-1586-3, 2013.

[4] B.A. Tuna and D. Rockwell, "Shallow flow past a cavity: attenuation of oscillations via a bed perturbation," *Environmental Fluid Mechanics*, vol. 15 (1), no. p. 179-206, 2014.

[5] B.A. Tuna and D. Rockwell, "Self-sustained oscillations of shallow flow past sequential cavities," *Journal of Fluid Mechanics,* vol. 758, no. p. 655-685, 2014.

[6] D. Rockwell and E. Naudascher, "Self-sustained oscillations of impinging free shear layers," *Annual Review of Fluid Mechanics,* vol. 11, no. p. 67-94, 1979.

[7] J.C. Bruggeman, A. Hirschberg, M.E.H. v. Dongen, and A.P.J Wijnands, "Self-sustained aero-acoustic pulsations in gas transport systems: Experimental study of the influence of closed side branches," *Journal of Sound and Vibration* vol. (11/1991) 150(3), no. p. 371-393, 1990.

[8] D. Rockwell, J.-C. Lin, P. Oshkai, M. Reiss, and M. Pollack, "Shallow cavity flow tone experiments: Onset of locked-on states," *Journal of Fluids and Structures* vol. 17 (3), no. p. 381-414, 2003.

[9] Howe, "Lectures on the theory of vortex-sound," *Lecture Notes in Physics* vol. 586, no. 31-111, 2002.

[10] I. Sobey, "Oscillatory flows at intermediate Strouhal number in asymmetric channels," *Journal of Fluid Mechanics* vol. 125, no. p. 359-373, 1982.

[11] D. Rockwell and E. Naudascher, "Review-- self-sustaining oscillations of flow past cavities," *Journal of Fluids Engineering* vol. 100, no. p. 152-165, 1978.

[12] P. Kriesels, M. Peters, A. Hirschberg, A. Wijnands, A. Iafrati, G. Riccardi, R. Piva, and J. Bruggeman "High amplitude vortex-induced pulsations in a gas transport system," *Journal of Sound and Vibrations* vol. (1995) 182(2), no. p. 343-368, 1994.

[13] S.M.N. Dequand, S.J. Hulshoff, and A. Hirschberg "Self-sustained oscillations in a closed side branch system," *Journal of Sound and Vibration* vol. 265(2), no. p. 359-386, 2003.

[14] P. Oshkai, T. Yan, A. Velikorodny, and S. VanCaeseele "Acoustic power calculation in deep cavity flows: A semiempirical approach," *Journal of Fluids Engineering* Vol. 130(5) no. doi: 10.1115/1.2907413, 2008.

[15] P. Oshkai, D. Rockwell, and M. Pollack, "Shallow cavity flow tones: Transformation from large- to small-scale modes," *Journal of Sound and Vibration* vol. 280(3-5), no. p. 777-813, doi: 10.1016/j.jsv.2003.12.054, 2004.

[16] P. Oshkai and T. Yan "Experimental investigation of coaxial side branch resonators," *Journal of Fluids and Structures* vol. 24(4), no. p. 589-603, doi:110.1016/j.fluidstructs.2007.10.008, 2008.

[17] D. Tonon, A. Hirschberg, J. Golliard, and S. Ziada, "Aeroacoustics of pipe systems with closed branches," *International Journal of Aeroacoustics* vol. 10, no. p. 201- 276, 2011.

[18] Dean and Dalrymple, "Water wave mechanics for engineers and scientists," Advanced series on ocean engineering vol. 2, 1991.

[19] K. Hourigan, M. C. Thompson, E. Brocher, and A. Andrianantoandro, "Coupling of vortex shedding with the fundamental resonant mode of a resonator tube," *Noise Control Engineering Journal* vol. 41 (2), no. p. 331-337, 1993.

[20] D. Tonon, J.F.H. Willems, and A. Hirschberg, "Self-sustained oscillations in pipe systems with multiple deep side branches: Prediction and reduction by detuning," Accepted for Publication (*Journal of Sound and Vibration*, 2011).

[21] X. Liu and J. Katz, "Vortex-corner interactions in a cavity shear layer elucidated by time-resolved measurements of the pressure field," *Journal of Fluid Mechanics* vol. 728, no. p. 417-457, doi:10.1017/jfm.2013.275, 2013.

[22] E. Naudascher and D. Rockwell, Flow-Induced Vibrations: An Engineering Guide, Rotterdam: A.A. Balkema Press, 1994.

[22] E. Naudascher and D. Rockwell, Flow-Induced Vibrations: An Engineering Guide, Mineola, New York: Dover Publications, Inc., 1994.

[23] V. Sarohia, "Experimental investagation of oscillations in flows over shallow cavities," *American Institute of Aeronautics and Astronautics Journal* vol. 15, no. p. 984, 1977.

[24] S. Ethamboboaglu, "On the fluctuating flow characteristics of in the vicinity of gate slots," Division of Hydraulic Engineering, Norwegian Institute of Technology, Trondheim, 1973.

[25] S. Ethembabaoglu, "Some characteristics of unstable flow past slots," *American Society of Civil Engineers Journal of Hydraulics Division* vol. 104(HY5) no. p. 649, 1978.

[26] J. Rossiter, "Wind-Tunnel Experiments on the Flow over Rectangular Cavities at Subsonic and Transonic Speeds," Aeronautical Research Council Reports and Memoranda, London, 1966.

[27] M. Alster, "Improved calculation of resonant frequencies of Helmholtz resonators," *Journal Sound and Vibration,* vol. 24, p. 64, 1972.

[28] H. Rouse, Fluid mechanics for hydraulic engineers, Dover Publ., 1938.

[29] C. J. Galvin, "Wave-height prediction for generators in shallow water," *U.S. Army Coastal Engineering Research Center,* vol. Mar, no. Tech Memo 4, 1964.

[30] O. Phillips, The dynamics of the upper ocean, Cambridge University Press ISBN 0-521-29801-6, p. 39, 1977.

[31] National Instruments (NI) PXI-4472 User Guide.

[32] W. Ganji, Introduction to engineering experimentation, New Jersey: Prentice Hall, 1996.

[33] R. P. Instruments, "Wave Height Gauge User's Manual," October 2007.

[34] M. Raffel, C.E. Willert, S. Wereley, J. Kompenhans, Particle Image Velocimetry: A Practical Guide, New York: Springer, 2007.

[35] M. Samimy and S.K. Lele, "Motion of particles with inertia in a compressible free shear layer," *Physics of Fluids A, Fluid Dynamics,* vol. 3, no. 8, p. 1915, 1991.

[36] C.T. Crowe, J.N. Chung, and T.R. Troutt, "Particle mixing in free shear flows," *Progress in Energy and Combustion Science,* vol. 14, no. 3, pp. 171-194 1263, 1988.

[37] D. Ricker, Echo Signal Processing, Springer ISBN 1-4020-7395-X, 2003.

[38] R.G. Brown and P.Y.C Hwang, Introduction to random signals and applied Kalman filtering, John Wiley and Sons ISBN 0-471-12839-2, 1997.

[39] L. Milic, Multirate Filtering for Digital Signal Processing, New York: Hershey, 2009.

[40] J.G. Proakis, Digital Signal Processing: Principals, Algorithms and Applications (3rd ed.), India: Prentice-Hall. ISBN 8120311299, 2000.

[41] N. M. Limited, "Calibration Certificate," 2013.

[42] J. Anderson, "The effect of an air flow on a single side-branch Helmholtz resonator in a circular duct.," *Journal Sound and Vibration,* vol. 52, no. 3, p. 423, 1977.

[43] W. Worraker, "Grazing flow effects on the impedance of cavity liners," Institute of Sound and Vibration Research, University Southampton Memo No. 600, University Southampton, 1980.

[44] H. Abiru and A. Yoshitake, "Experimental study on a flapping wing hydroelectric power generation system," in *American Society of Mechanicl Engineers Power Conference,* Volume 2, Denver, Colorado, USA, 2011.

[45] D. Rockwell, "Vortex formation in shallow flows.," Physics of Fluids, vol. 20, 2003.

[46] University of Victoria, "Free-Surface Wave Cavity Resonator". Patent 2847-85585-01, 2 July 2010.

[47] J. Reaume, "Wave-Cavity Resonator Theory and Preliminary Design Report," Mech 499 Project, University of Victoria, 2011.

[48] J.A. Uijttewaal, "Shallow Flows," Delft, The Netherlands, 2003.

[49] D. Chen and G.H. Jirka, "Experimental study of plane turbulent wake in a shallow water layer," *Fluid Dynamics Research* vol. 16, no. 1, p. 11-41. 1995.

[50] G.H. Jirka, "Large scale flow structures and mixing processes in shallow flows," *Journal of Hydraulic Research* vol. 39, no. 6 pp. 567-573, 2001.

5 Appendix A
Derivation of cavity wave frequency equations

Airy wave theory gives a linear approximation to the wave equation and is valid for small amplitude waves with the assumptions of:

1. Smooth bottom conditions with a horizontal orientation (BBC).
2. Constant pressure across the entire free surface (DFSBC).
3. Medium is homogeneous and incompressible (Conservation of mass).
4. Inviscid wave, which is true except for small regions of wave vortices near free surface (Potential theory).

From potential theory we have:

$$u = -\frac{\partial \emptyset}{\partial x}; v = \frac{\partial \emptyset}{\partial y}; w = -\frac{\partial \emptyset}{\partial z}. \quad \text{(A.1)}$$

Where u and v represent the longitudinal and lateral velocities and the lateral velocity for 2D wave propagating in the x-direction is equal to zero.

According to conservation of mass we have:

$$\nabla^2 \emptyset = \frac{\partial^2 \emptyset}{\partial x^2} + \frac{\partial^2 \emptyset}{\partial z^2} = 0. \quad \text{(A.2)}$$

This leads to:

$$\frac{\partial^2 \emptyset}{\partial x^2} + \frac{\partial^2 \emptyset}{\partial z^2} = u^2 + w^2. \quad \text{(A.3)}$$

According to conservation of energy we have:

$$\frac{\partial \emptyset}{\partial t} + \frac{p}{\rho} + \frac{1}{2}(u^2 + w^2)^2 + gz = 0. \quad \text{(A.4)}$$

Boundary conditions can be applied to the Laplace equation and conservation of energy equation to obtain a solution. These include the Bottom Boundary Condition (BBC), Kinematic Free Surface Boundary Condition (KFSBC), and the Dynamic Free Surface Boundary Conditions (DFSBC).

BBC for z=-h:

$$w = -u\frac{dh}{dt}. \quad \text{(A.5)}$$

KFSBC for z=η:

$$w = \frac{d\eta}{dt} + u\frac{d\eta}{dx}. \quad \text{(A.6)}$$

KFSBC for z=0 with small wave amplitude (H/2) + η ≈ η:

$$w = \frac{d\eta}{dt}. \tag{A.7}$$

DFSBC for z=η:

$$\frac{\partial \emptyset}{\partial t} + \frac{1}{2}\left(\left(-\frac{\partial \emptyset}{\partial x}\right)^2 + \left(-\frac{\partial \emptyset}{\partial z}\right)^2\right) + g\eta = 0. \tag{A.8}$$

DFSBC for z=0 with small frequencies:

$$g\eta - \frac{\partial \emptyset}{\partial t} = 0. \tag{A.9}$$

Solving the conservation of energy equation with DFSBC gives:

$$\emptyset = C \cos kx \cosh k(h+z) \sin \sigma t. \tag{A.10}$$

The arbitrary constant C can be eliminated by applying DFSBC where:

$$C = \frac{Hg}{2\sigma \cosh kh}. \tag{A.11}$$

Free surface height η can then be determined using KFSBC and ∅ to obtain Equation 1.6 in thesis:

$$\eta = \left(\frac{H}{2}\right) \cos \sigma t \cos kx. \tag{A.12}$$

The result for C can be combined with the result for ∅ to find the velocity potential from separation of variables of the Laplace equation:

$$\emptyset = \frac{\mathrm{Hgcosh}\, k(h+z)}{2\sigma \cosh kh} \sin \sigma t \cos kx \tag{A.13}$$

Using these two results for ∅ and η the angular frequency of the wave σ can be solved:

$$\sigma^2 = gk \tanh kh \tag{A.14}$$

Solving for $\tanh kh$ shows that each k has a distinct σ and h and gives:

$$k = \frac{\sigma^2}{g \tanh kh}. \tag{A.15}$$

Substituting the result for ∅ into the linearized KFSBC and DFSBC and solving for η results in Equation below:

$$\eta = \left(\frac{H}{2}\right) \cos(kx - \sigma t). \tag{A.16}$$

Using the dispersion relation of Equation A.14 with wave celerity given by c=λ/T and angular frequency by σ=2π/T results in:

$$c = \sqrt{\frac{g}{k} \tanh kh}. \tag{A.17}$$

This can be reduced for h/λ>0.5 (Deep waves) to:

$$\sigma^2 = gk \rightarrow c = \sqrt{\frac{g}{k}}, \tag{A.18}$$

And for h/λ<0.05 (Shallow waves) to:

$$\sigma^2 = gk^2h \rightarrow c = \sqrt{gh}. \tag{A.19}$$

Using f=c/λ with the appropriate λ based on the boundary conditions and discussed in the thesis gives the cavity frequency prediction formula.

6 Appendix B Copyright permissions

Pending permissions.

7 Appendix C
Detailed analysis of depth effect on resonator

This detailed analysis of the frequency components obtained for the range of depth tests with varying inflow velocity and fixed cavity opening length (L_{ec}) provides additional insight and support of the proposed hydrodynamic frequency mode prediction using Equation 3.5. The notation used is slightly different than the discussion and is defined as follows:

A1, A2, A3, …	Interaction between wave mode and hydrodynamic mode occurring in order of appearance during increasing inflow velocity. Equivalent to "Pn" in discussion.
C1, C2, C3, …	1^{st}, 2^{nd}, 3^{rd}, … longitudinal cavity wave mode using closed-closed boundary conditions for shallow cases and cavity length corrected open-closed boundary conditions for intermediate and deep cases.
Froude1, Froude2, …	1^{st}, 2^{nd}, … hydrodynamic mode using model proposed in Equation 3.5.
L1, L2, …	1^{st}, 2^{nd}, … lateral cavity modes using closed-closed boundary conditions.
H1, H2, …	Harmonics of resonant waves occurring from interaction of cavity waves and hydrodynamic frequencies arranged for increasing inflow velocity.

The discussion of the progression of change on the system with increasing depth begins with the h=0.04 m result since shallower results simply do not respond to any excitation by the shear layer. Contours of power spectral density along with the waterfall plots from which they are derived are presented below for the first case in Figure 7.1. For the h=0.04 m case below, the fundamental cavity frequency is predicted using shallow water wave

theory with closed-open boundary conditions and a corrected cavity length that accounts for added mass of the open boundary condition.

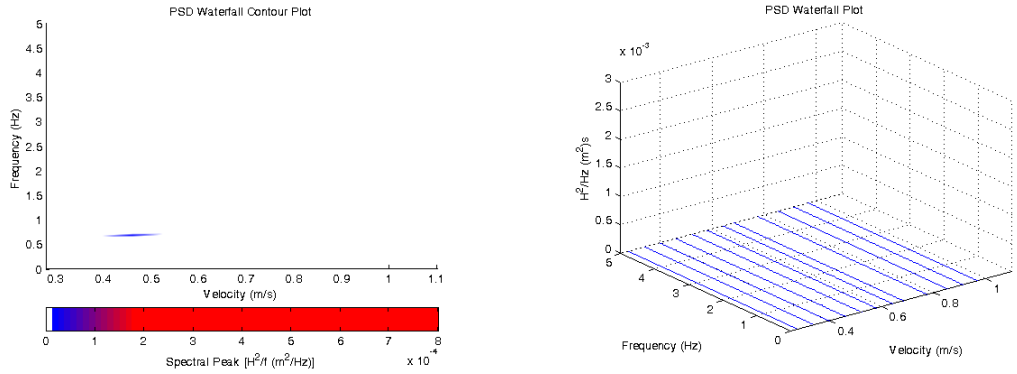

Figure 7.1: PSD data for h=0.04 m, Lec=0.161 m, Lc=0.622 m.

Essentially no regular cavity wave is present due to a large difference between the hydrodynamic frequency and the natural frequency of the cavity. The first mode of the cavity wave should be in the shallow regime and a frequency component is observed at the natural frequency of the cavity (C1 in Figure 7.2). There is evidence that this mode is most easily excited at this frequency by any system disturbance although for this case not a periodic disturbance. This frequency mis-match between C1 and Fr1 and the frequency response of the cavity occurring near C1 can be seen from the overlay of the theoretical hydrodynamic and cavity frequencies in Figure 7.2.

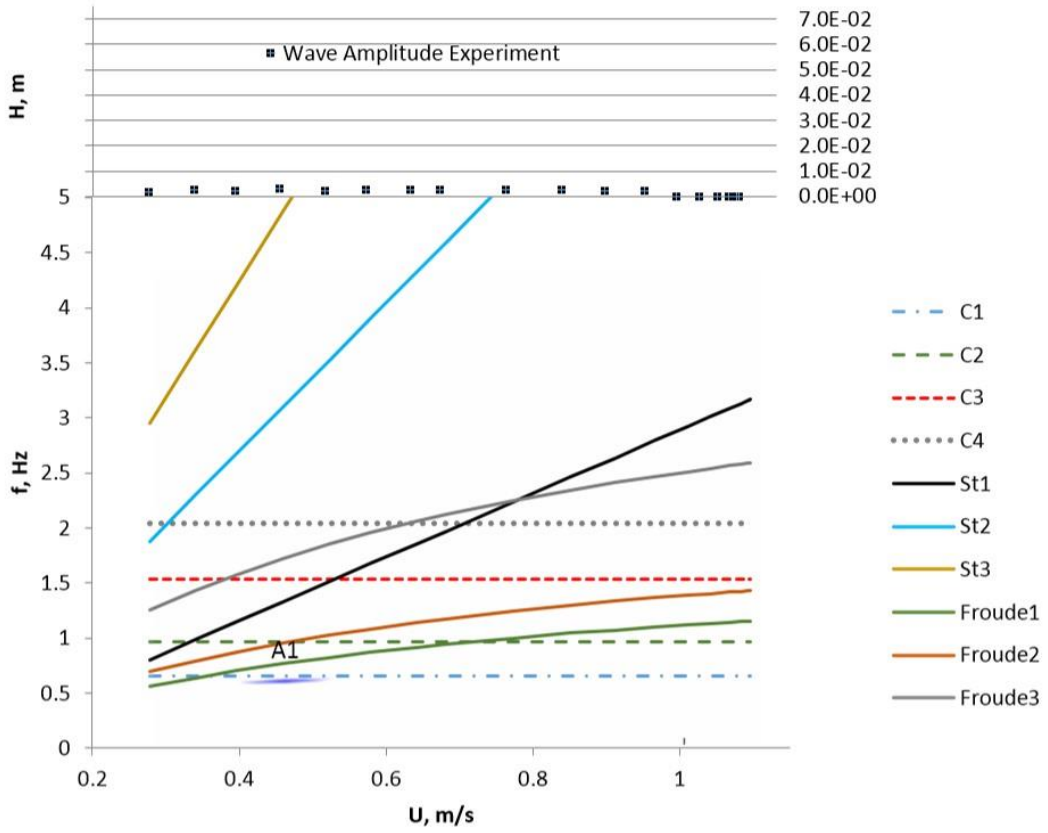

Figure 7.2: PSD frequency overlay along with cavity free surface height data (h=0.04 m).

Since the disturbances are not in phase with the system response a sustained net energy transfer to the cavity wave is not observed (resonance does not occur) and any random flow oscillations for which the system responds are dissipated as can be seen by the averaged wave amplitude data collected.

Increasing the cavity depth to 0.06 m still results in a shallow wave classification for the first mode with a peak response at inflow velocities near 0.64 m/s. This peak is shifted up ~40% from 0.47 m/s from the previous depth test while the natural frequency of the cavity has only increased 20% due to the increase in depth.

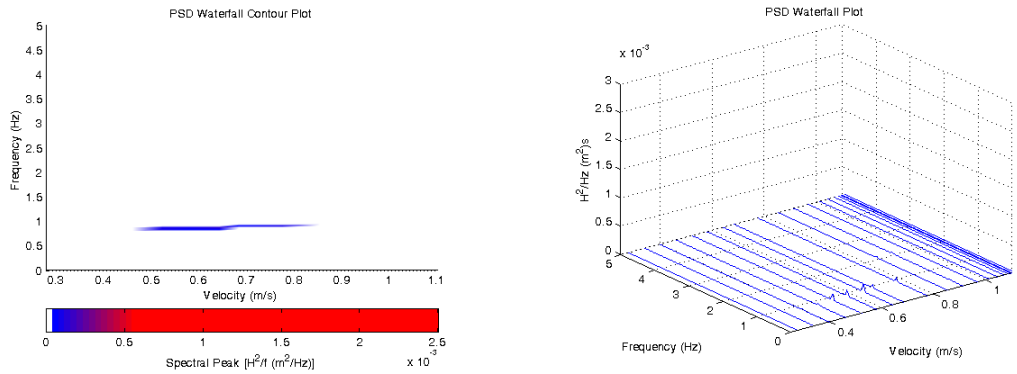

Figure 7.3: PSD data for h=0.06 m, Lec=0.161 m, Lc=0.622 m.

In addition, the system has a larger response width in terms of frequency response to inflow velocities and a periodic response near 0.8 cm in amplitude across this response width. This regular response results from a closer matching of the two frequencies C1 and Fr1 (Figure 7.3) and the low amplitude indicates that the source power from the vortex impingement is not large compared to the dissipative effects. Again, for cases such as this the wave amplitude corresponds simply to the free surface displacement caused by an impinging vortex whereas for deeper cases with strong resonance the vortex actually enters the cavity providing a different form of wave excitation. There is enough interaction for organization of the shear layer but the frequencies are not locked on and the cavity fluid simply oscillates at its natural frequency in response to the out of phase impingement of vortices.

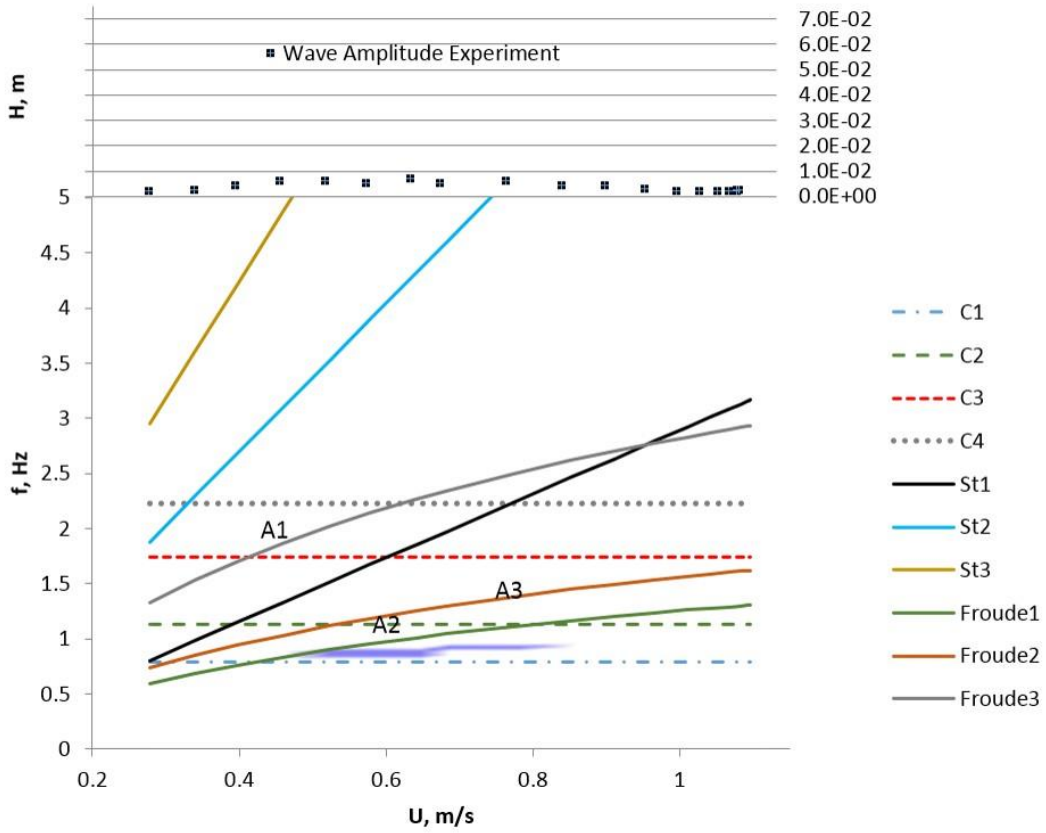

Figure 7.4: PSD frequency overlay along with cavity free surface height data (h=0.06 m).

The peak amplitude A2 is seen to occur over the range of the response width indicating that the amplitude of the cavity wave is large enough to begin causing pressure fluctuations that shift the shear layer frequency (as C1 and Fr1 theoretical values diverge the A3 peak is still observed closest to C1) or at least that some organization of the shear layer occurs for small-scale Kelvin-Helmholtz instability vortices to coalesce. It should be noted that since the system was restarted before each test case, taking a significant amount of time yet necessary due to the observance of hysteresis during preliminary tests, the measured wave amplitudes were not immediately observed. The steady state oscillation only came about after the long term mode/effects dominated from smaller

disturbances which in itself is somewhat a form of hysteresis since any random disturbances cause the system to respond at the natural frequency thus strengthening vortex-cavity interaction.

For the 0.09 m depth test the fundamental cavity frequency C1 is also a shallow wave mode and the previously mentioned trends continue as can be seen in Figure 7.5.

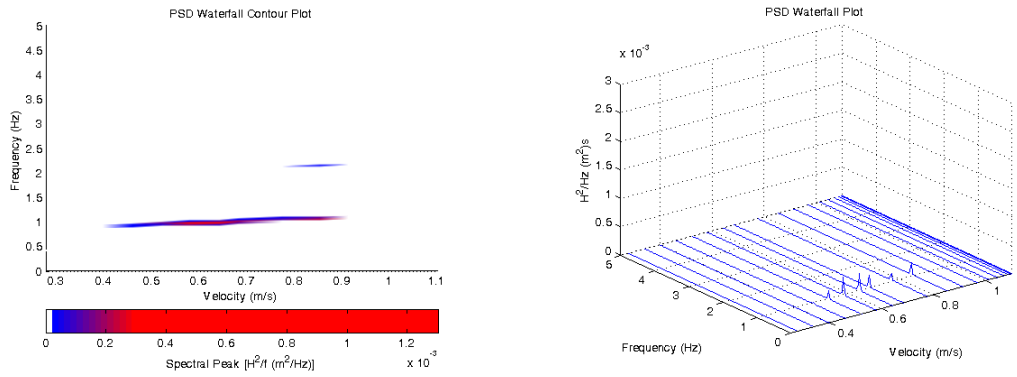

Figure 7.5: PSD data for h=0.09 m, Lec=0.161 m, Lc=0.622 m.

An increase of 20% of the natural frequency of the cavity due to the increase in depth resulted in no shift the in A1 peak staying at ~0.64 m/s. The first appearance of a secondary frequency response peak H1 is observed in Figure 7.6 near C2-Fr1 but at a frequency close to the 1st harmonic of A1. As for the 0.06 m case the predicted C1 frequency is very close to the measured frequency when using the calculated +9.5% increase in wave celerity associated with a peak amplitude of 0.0112 m.

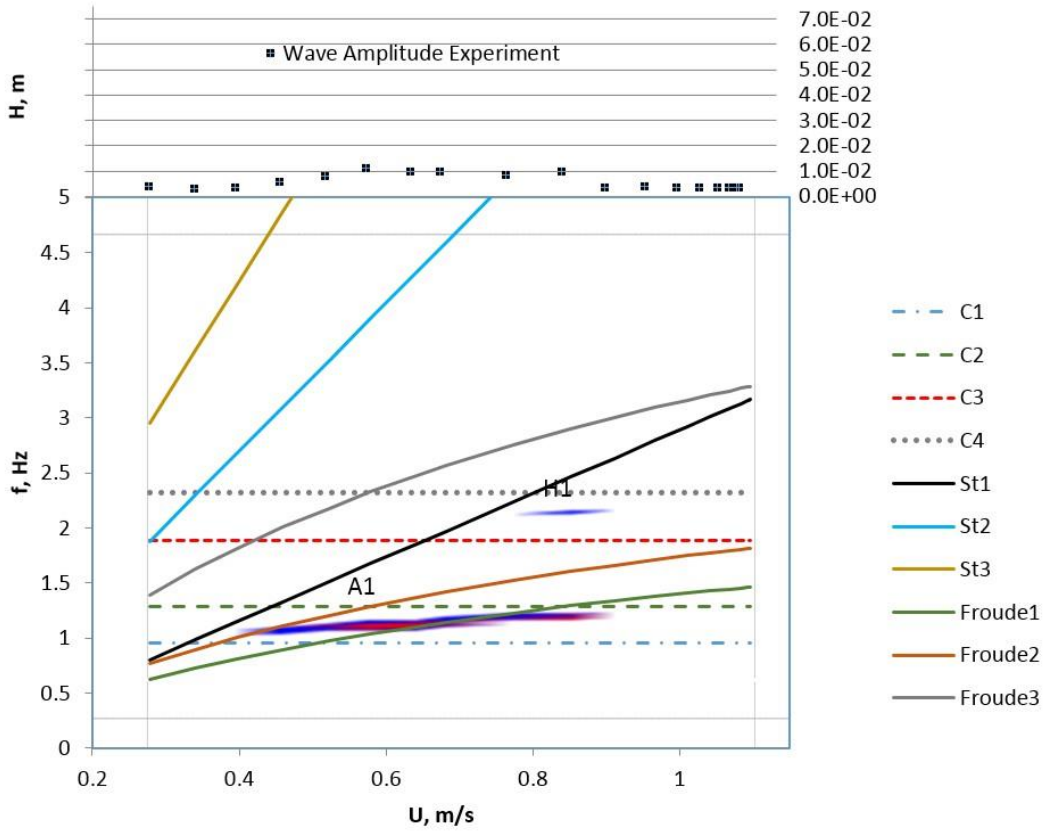

Figure 7.6: PSD frequency overlay along with cavity free surface height data (h=0.09 m).

The next depth case can no longer be classified as having a mode with a shallow water wave condition and is fully within the intermediate regime.

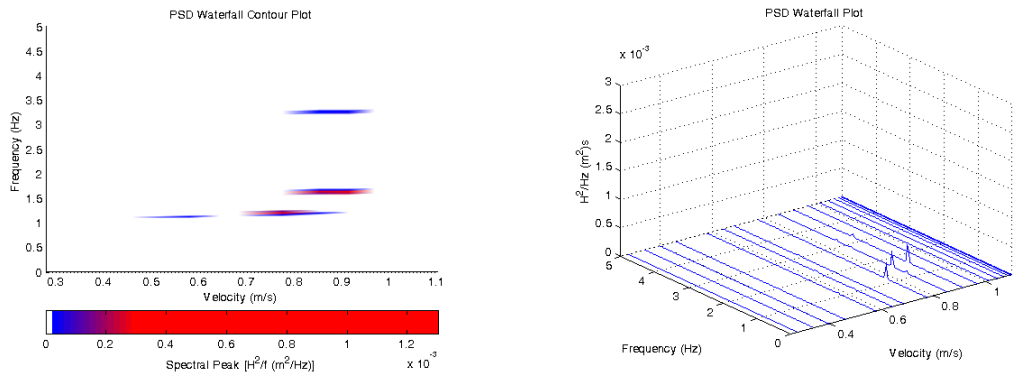

Figure 7.7: PSD data for h=0.12 m, Lec=0.161 m, Lc=0.622 m.

In this case we see that a peak amplitude of 0.0131 m occurs for a matching of C3 and Fr2 along with a significant high frequency component that occurs near Fr3 and the second lateral mode. This high frequency component L1 corresponds to a deep water wave lateral mode of the cavity with $L_{eff}=W_c$ and closed-closed conditions. Using the appropriate conditions a frequency for this lateral mode of 3.53 Hz is predicted and is within +10% of the measured component. The L1 interaction is also within +4.6% of the 1st harmonic of A3.

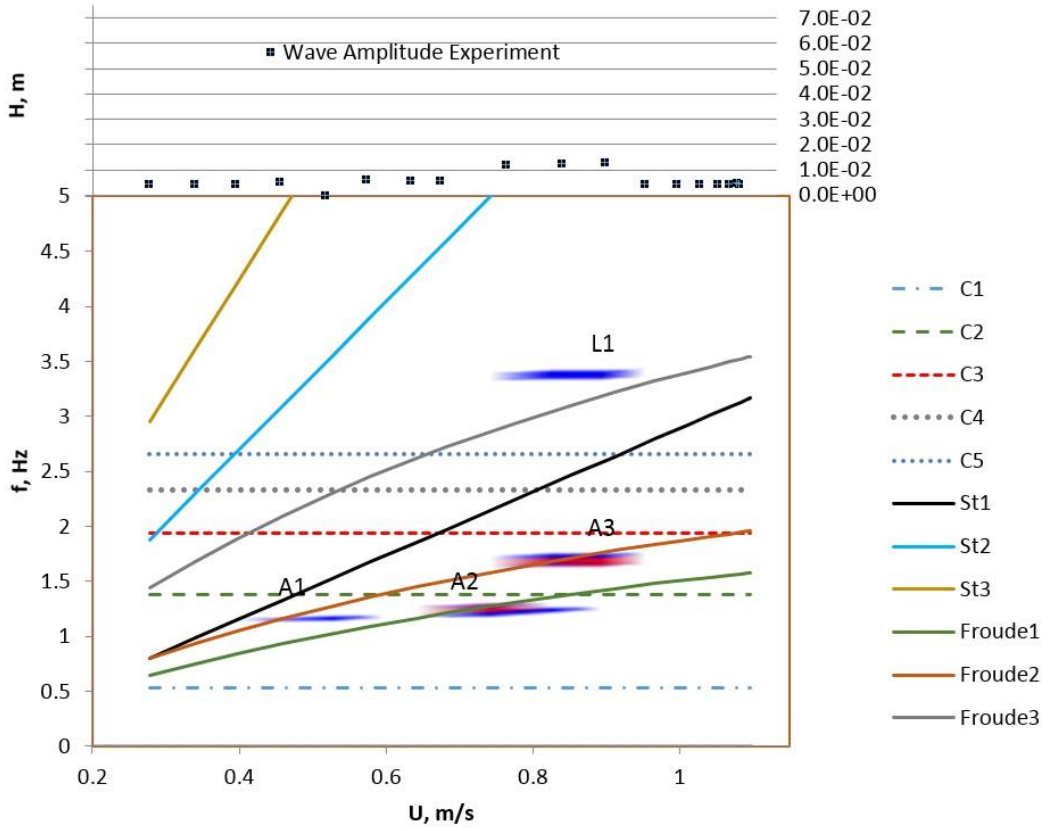

Figure 7.8: PSD frequency overlay along with cavity free surface height data (h=0.12 m). Lesser peaks are observed at A1 and A2 corresponding to interactions of Fr2-C2 and Fr1-C2 respectively but it is apparent that the cavity frequency at C3 is over predicted by the theoretical model for the maximum amplitude case. A significant wave amplitude is not

present suggesting that non-linear effects on wave celerity due to wave height do not explain this disparity as an increase in C2 frequency although as second mode wave is occasionally observed. This may demonstrate that a strong second hydrodynamic mode has pulled the cavity frequency by shifting the wavelength. A mode jump is also observed in both the hydrodynamic and cavity wave modes between A2 and A3. The mode jump between A2 and A3 is consistent with the open-closed case since it occurs for the second and third mode of the cavity wave. The cavity frequency is over predicted for the second and third modes.

The 0.15 m case is perhaps the most interesting of the tests in that a very three-dimensional wave with significant lateral and longitudinal modes is observed.

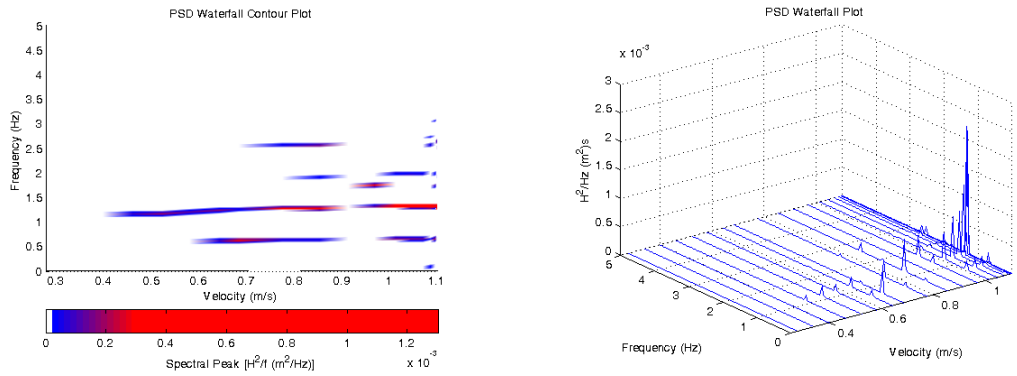

Figure 7.9: PSD data for h=0.15 m, Lec=0.161 m, Lc=0.622 m.

A maximum amplitude of 0.0356 m is observed at the maximum inflow velocity but the data set is unable to capture the peak amplitude due to the limitations of the flow facility in an open channel configuration where pressurization is not possible. In any case this peak at A4 does not correspond well with interactions between the free shear layer and a cavity mode. While Fr2-C3 interaction occurs near A4 the main frequency components are observed near C2 and C1. The wide range of frequencies observed without corresponding interactions and poor Q-factor indicates broadband excitation of cavity

modes rather excitation from shear layer mode of interest. In this case Fr1-C2 (A3) and Fr2-C3 (between A3 and A4) interactions are observed and correspond to resonant coupling. The low frequency component occuring at C1 however, is also not explained by the hydrodynamic model. The component at H1 is a distance away from Fr3 but occurs at a frequency higher than the 1st lateral cavity mode and 5.5% less than the 1st harmonic of A4 occurring near C2.

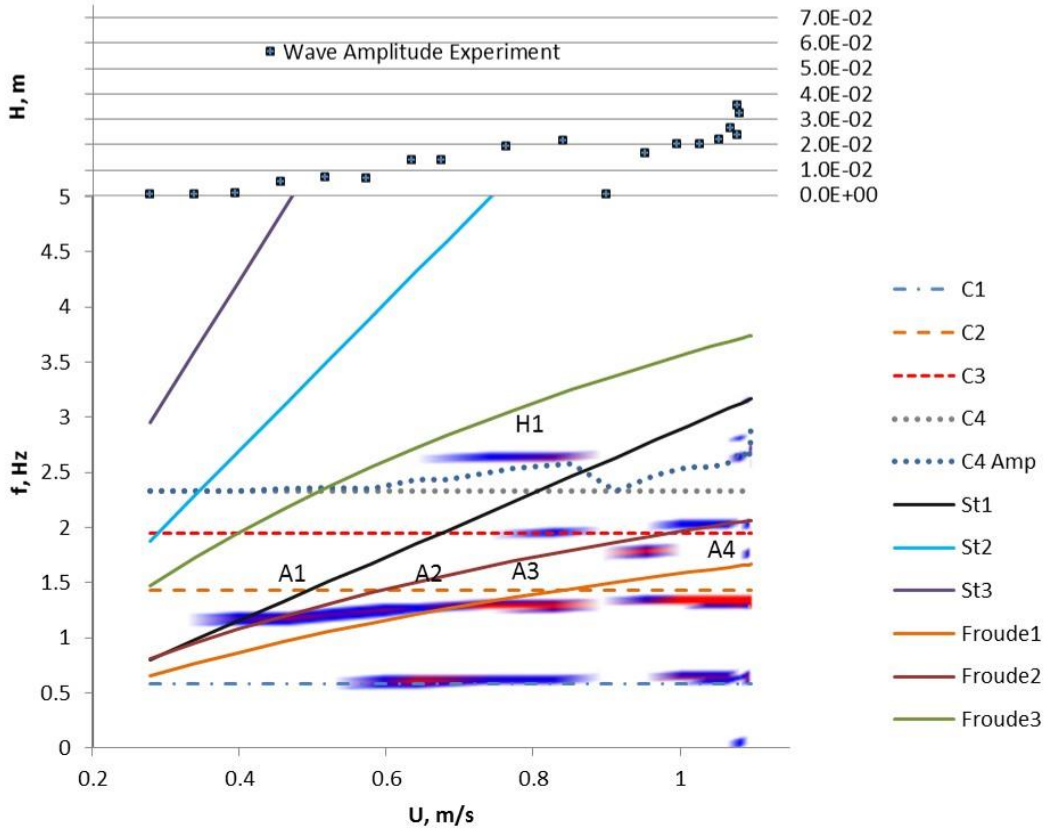

Figure 7.10: PSD frequency overlay along with cavity free surface height data (h=0.15 m).

It is apparent that a highly complex system can be excited requiring careful consideration from an energy harvesting perspective; while potentially providing additional power contributions to the wave the many frequency components would require special

consideration in terms of matching phases of the net power harvested from the system to these contributions to avoid breaking down the coupling. This may prove impractical due to the further complication of shifting frequencies depending on wave amplitude height and standing waves and phase shifts caused by the motion of wave absorbers discussed in Section 2.4.6.

In the h=0.18 m case a maximum cavity wave amplitude was observed of 0.0267 at the maximum inflow velocity.

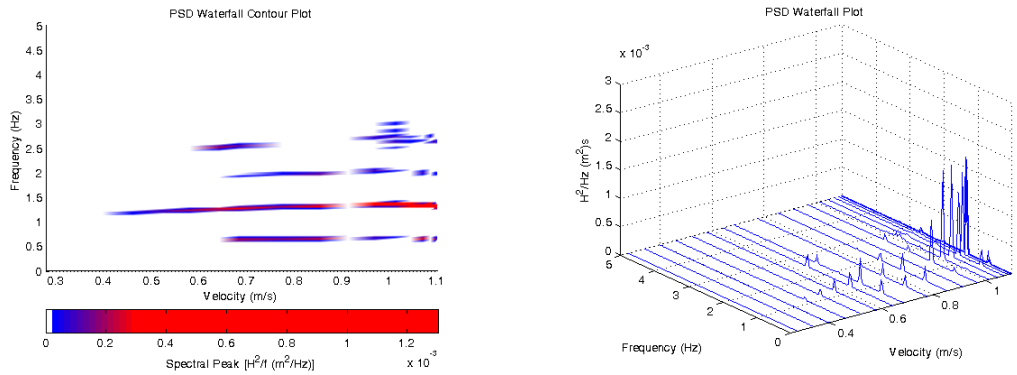

Figure 7.11: PSD data for h=0.18 m, Lec=0.161 m, Lc=0.622 m.

A similar range of frequencies is excited as was seen for the 0.15 m case and amplitude peaks are observed with A1 corresponding to Fr2-C2 and a A2 with Fr1-C2 and a Fr3 interaction near the 1st lateral cavity mode. This lateral mode is 4.7% higher than the predicted frequency of the lateral mode and 1.5% lower than the first harmonic of A2 and also close the C4 frequency when wave amplitude effects are taken into consideration. There is again a low frequency component occurring at the C1 frequency without excitation of a hydrodynamic mode of interest. This is likely to occur from noisy inflow conditions that excited the cavity modes seen in the PSD waterfall plot. Considerable vibrations due to the phase difference between the cavity wave and the shear layer may cause broadband excitement of other frequencies as observed near maximum inflow

velocity: for strong 1st hydrodynamic modes (at high inflow velocities) near 3rd cavity modes if the cavity frequency is not sufficiently close destructive interference between standing waves and incident waves generated by the shear layer impingement excites a range of cavity frequencies. The phase difference is seen both in this system noise and in the smaller wave amplitude in comparison to the 0.15 m case.

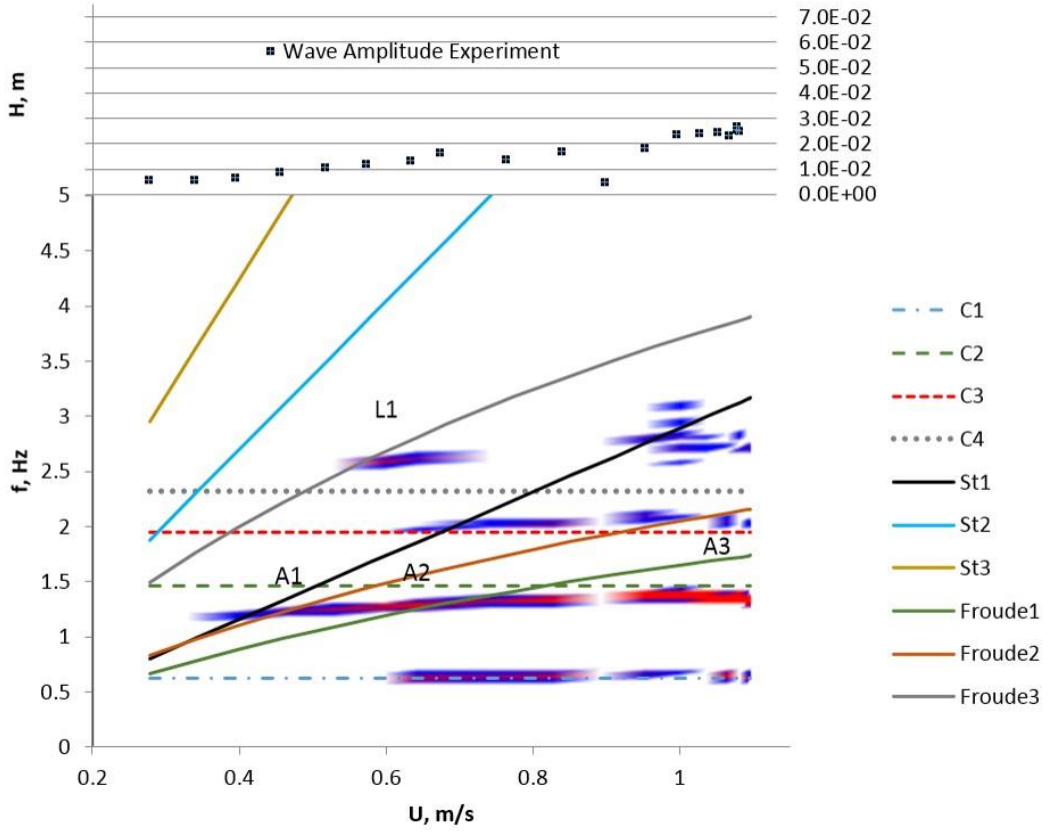

Figure 7.12: PSD frequency overlay along with cavity free surface height data (h=0.18 m).

The highest mode, C4, is a deep water wave and applying correction for wave height increases the prediction of C4 bringing it closer to the high frequency components near the maximum inflow velocity. There is also a Fr3-C4 interaction near 0.6 m/s that is near the frequency of the 2nd mode of a lateral cavity wave mode as previously mentioned. Once again, C2 is over predicted even though according to wave height corrections it

should be under predicted. Using L_c=0.622 m instead of L_c=0.461 m provided the correct under prediction of cavity frequency in general while the 0.12 m and 0.15 m cases worked best with L_c=0.622 and closed-closed boundary conditions. However, this model failed to correspond with hydrodynamic interactions with cavity frequencies well and resulted in significant error in predicting wavelength in comparison to the experimentally measured values. The value of L_{eff} calculated from the measured wavelength was lower by 10% for the first mode, 6% for the second mode, and 2% lower for the third mode. Results for the most commonly excited second mode were typically within 2% of that predicted by the model and are used here. This is discussed further in the hydrodynamic prediction section.

Higher inflow velocity data collected from the h=0.20 m case was deemed compromised due to an incident with the capacitive wave gauge wherein recalibration was required. However, the valid data shows identical trends to those of the previous intermediate water wave cases, namely the h=0.15 m and h=0.18 m cases. A notable feature about the data in this intermediate range is that the effect of depth on the resonant frequency of the cavity is much reduced as compared to cases exciting shallow water waves.

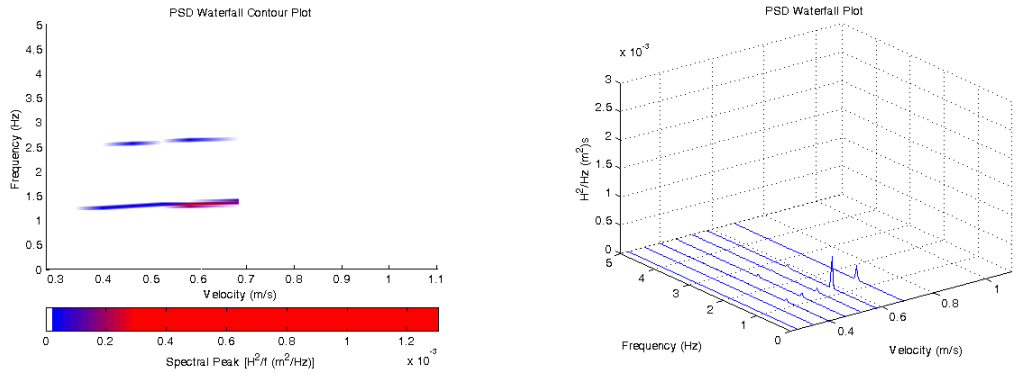

Figure 7.13: PSD data for h=0.20 m, Lec=0.161 m, Lc=0.622 m.

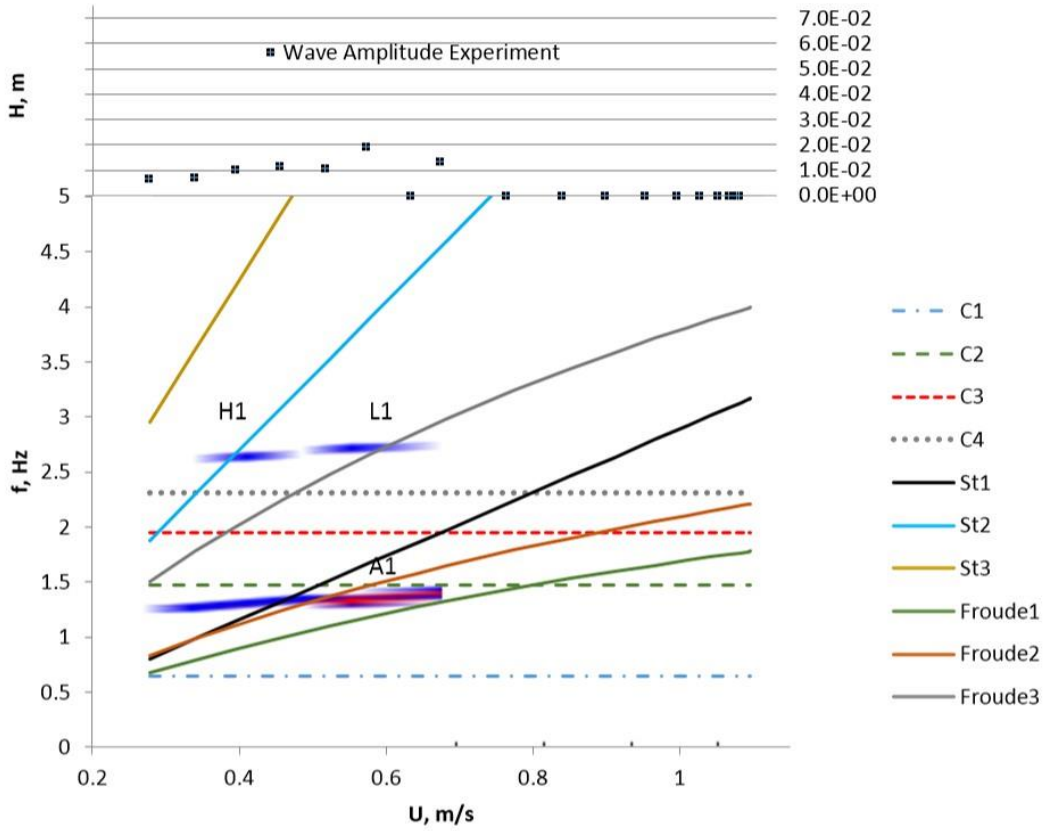

Figure 7.14: PSD frequency overlay along with cavity free surface height data (h=0.20 m). Peak amplitude was measured at A1 at an inflow velocity 0.59 m/s at 0.019 m in magnitude corresponding to Fr1/Fr2-C1. Mode jumping was again observed intermittently to Fr3-C4 at a reduced amplitude magnitude. The interaction at L1 is 7.6% higher than the 1st lateral mode frequency and very close to Fr3 but it is also 10% higher than the 1st harmonic of A1 and near the corrected C4 cavity frequency. A harmonic frequency H1 is also observed within 3% of the 1st lateral mode and is not near L1. It appears that since H1 occurs away from Fr3 with very similar characteristics to L1 these higher frequency components are harmonics of the primary modes occurring near C4. The system is excited less easily by this higher Strouhal mode as seen when the system responds near the cavity frequency rather than being driven by the interaction.

Further increasing the cavity depth to 0.24 m continues shifts the cavity frequency to excite lateral cavity wave modes at lower inflow velocities.

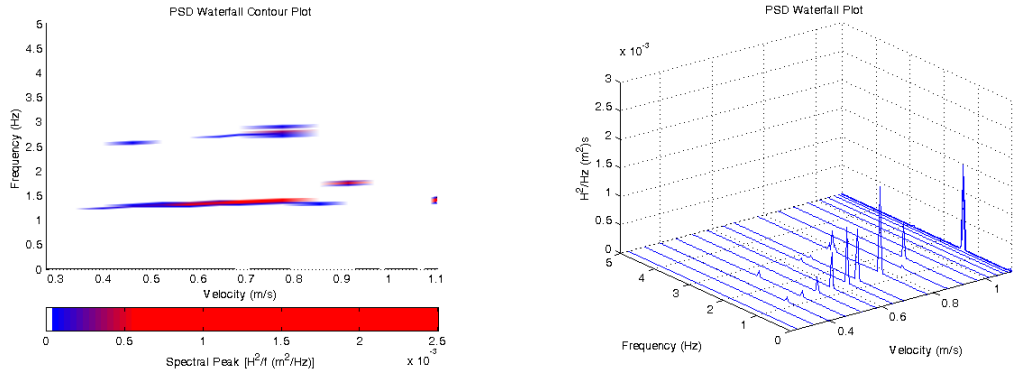

Figure 7.15: PSD data for h=0.24 m, Lec=0.161 m, Lc=0.622 m.

An amplitude peak occurs near 0.69 m/s corresponding to Fr2-C2 and a lesser peak A2 corresponds to Fr1-C2 while Fr3 excites a lateral mode near L1 within 7% of the 1st lateral cavity mode. The component at H1 is within 1% of the harmonic of the dominant mode. At the upper range of inflow velocity the system cascades and a wave amplitude close to that observed at the 0.69 m/s peak is observed at the C2 frequency despite not being in the proximity of one of the predicted hydrodynamic frequencies while Fr2-C2 and Fr3-C4, both deep water wave cases, interact. This is also observed for the 0.270 m and 0.300 m depths cases. In any case the dominant frequency interaction becomes more pronounced in comparison to shallower cases.

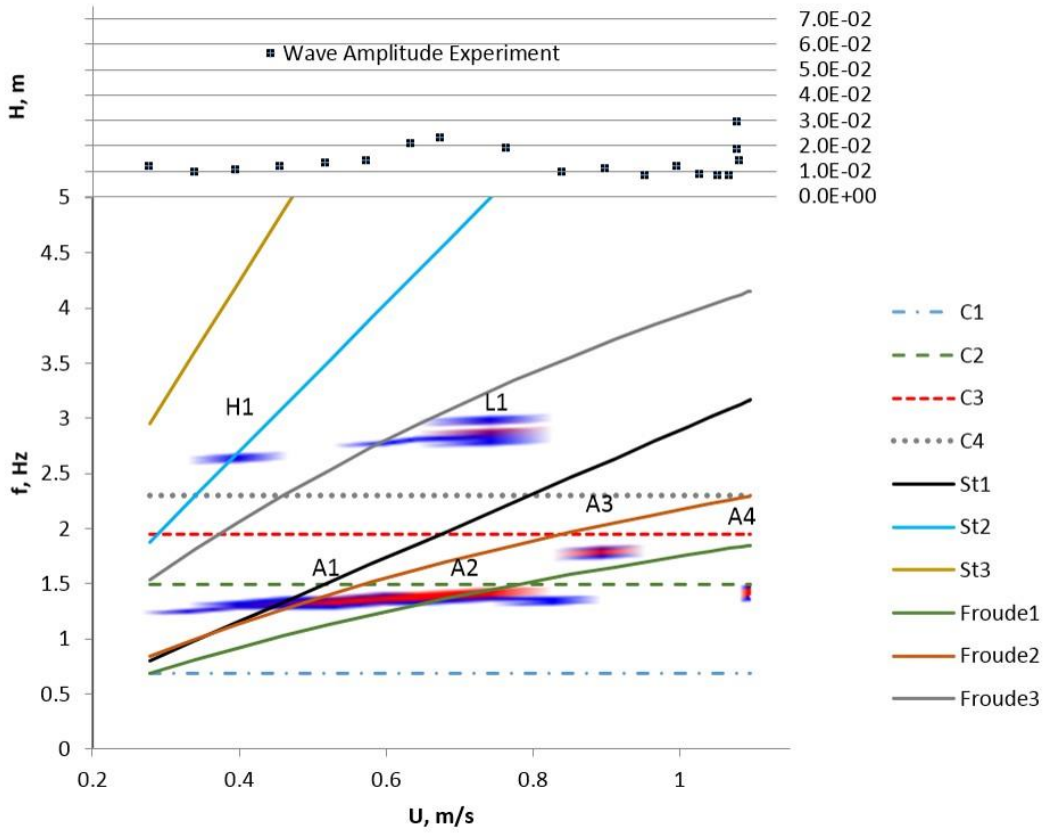

Figure 7.16: PSD frequency overlay along with cavity free surface height data (h=0.24 m).

The final two depth cases at h=0.27 m and h=0.30 m are very similar as would be expected with minor changes to the cavity wave frequencies between the two depths. A more pronounced peak amplitude is observed at a higher velocity in comparison to the 0.24 m case and the broadband excitation of the wave at the upper range of inflow velocity is also observed.

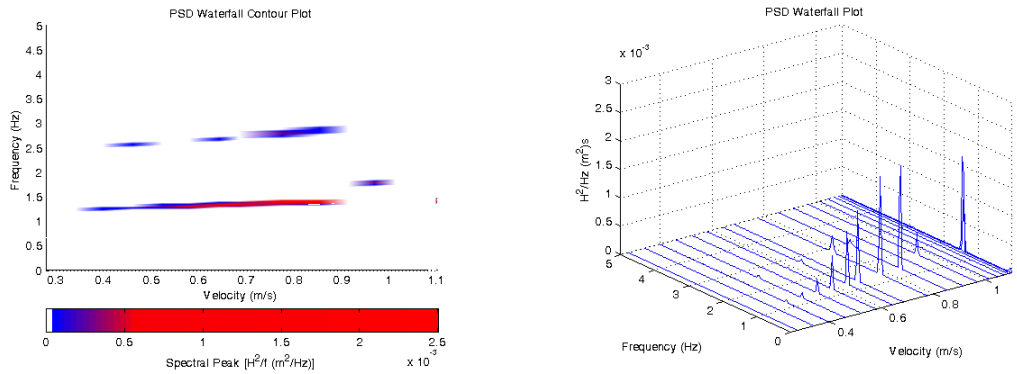

Figure 7.17: PSD data for h=0.27 m, Lec=0.161 m, Lc=0.622 m.

Peak cavity wave amplitude was found to be 0.027 m at an inflow velocity of 0.77 m/s. Non-linearities are once again observed in the form of significant secondary spectral peaks and resonance broke down after 0.91 m/s until the end effects occurred. As the inflow velocity is increased Fr1 approaches the over predicted C2 frequency, the wave amplitude and spectral peak increase, and lock on occurs at A3. Increasing the inflow velocity past peak resonance results in decreased amplitudes and eventual break down of the resonant coupling as seen in the wave amplitude and waterfall plot data.

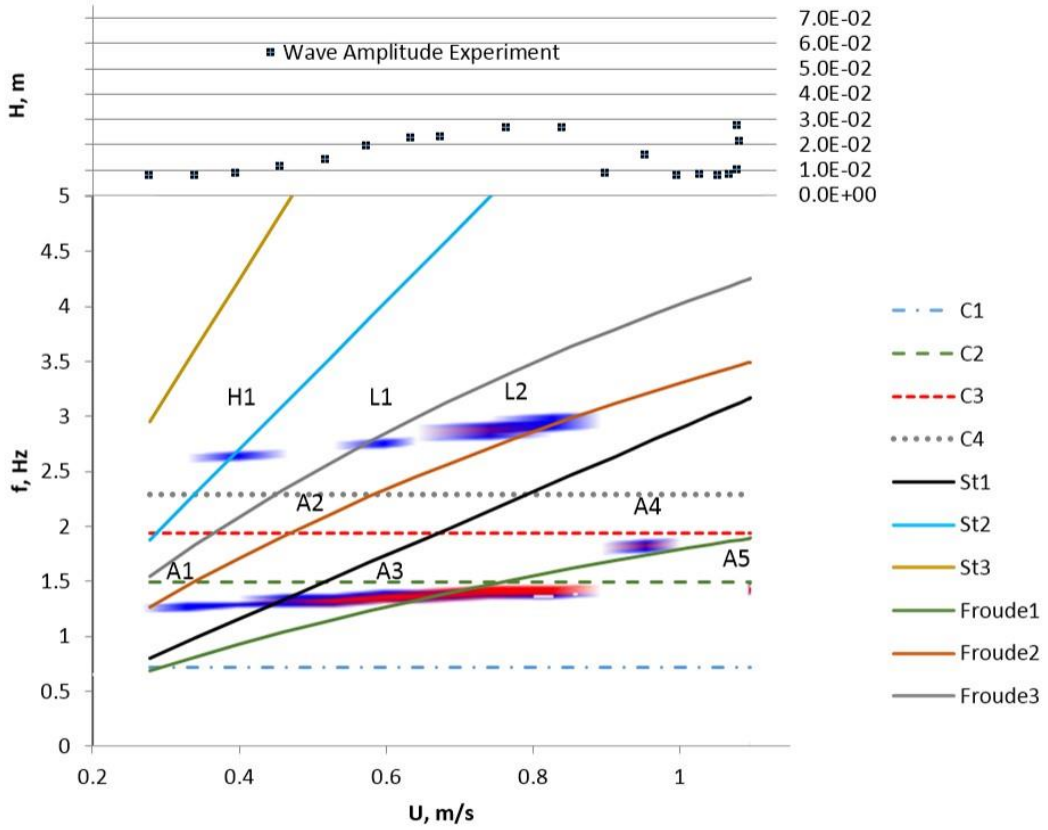

Figure 7.18: PSD frequency overlay along with cavity free surface height data (h=0.27 m).

An amplitude peak A4 also occurs with Fr1-C3 near 0.97 m/s and then decays. The system parameters are matched well enough that a cavity wave is observed with a minimum of 0.008 m wave amplitude across the entire velocity range where spectral peaks in the vicinity of A1 are observed. This is seen in the contour plot as a very wide band spanning the data set. The very large peak amplitude and spectral peaks observed at A5 occurs near a C2 frequency but is not within range of a hydrodynamic mode. The wide range of frequency responses across the cavity modes is not observed as it was for the 0.15 m and 0.18 m cases where broadband excitement near the upper regions of the flow are observed but this interaction is still considered outside of the scope of the investigation and is attributed to external excitation perhaps by lock on with a mode that

was previously causing the broadband excitation at lower depths. The higher mode interactions at H1, L1, and L2 were higher than the 1st lateral cavity mode by 3.3%, 7.6%, and 13% respectively. The component at H1 was within 1.4% of the first harmonic of the A1 interaction and L1 and L2 were identical to the harmonic of A3. The components at L1 and L2 are significant since they line up with the predicted Fr2 and Fr3 trends and occur at the amplitude corrected C4 frequency indicating that at some point in the data set these hydrodynamic modes may have contributed to a resonant mode.

System Hysteresis:

The effect of wave amplitude on wave celerity reached a maximum of 17.5% for the C4 mode as would be expected. This can provide insight into the hysteresis observed since the celerity of higher modes at deeper depths is affected more by wave amplitude than for lower modes. Therefore at inflow velocities at which higher hydrodynamic modes can be generated interaction at lower hydrodynamic and cavity modes can cause wave amplitude to increase the effectively higher cavity mode frequencies within range of a hydrodynamic mode and organization of the shear layer can be influenced by this higher wave mode and lead to mode jumping. The large wave amplitude can effectively help the system jump to higher mode interactions to maintain resonance whereas restarting the system for each test will result in eventual decoupling when the hydrodynamic and cavity frequencies diverge with increasing velocity and collapse of resonance is observed. This is as seen at the U=0.91 m/s data point in Figure 7.18. It should be noted that this higher mode interaction at A4 did not occur for nearly 20 seconds after reaching the correct inflow velocity. The previous point at U=0.91 m/s was recollected twice before leaving the system for 120 seconds without any observed resonance. When the system was not

restarted however, both the 0.91 m/s and subsequent points resonated and the frequency spectrum was more continuous.

As mentioned, similar trends were also observed for the 0.30 m case although this case did not resonate as well as the 0.27 m depth. Peak amplitude was measured at 0.0235 m at 0.68 m/s rejecting the 0.03 m amplitude occurring at 1.1 m/s for the same reasons previously mentioned.

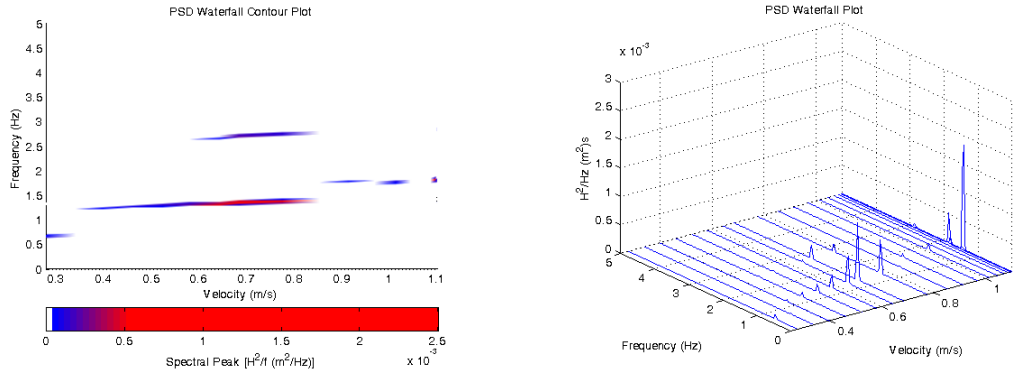

Figure 7.19: PSD data for h=0.30 m, Lec=0.161 m, Lc=0.622 m.

A peak at A1 corresponds to Fr1-C1 with a lesser A2 associated with Fr2-C2 and peak amplitude observed at A3 with a close matching of Fr2-C2. The component at H1 is closer to Fr3 and within 10% of the 1st lateral cavity mode but within 1.3% of the harmonic of A3. This is also near the effective frequency of C4 and is notable since H1 occurs near C4 again despite a lower error of 10% seen in this depth case and the 0.15 m depth case in comparison to the 17.5% seen in the 0.27 m case. This shows once again that the higher frequency components seen in deeper cases correspond best with the corrected C4 frequency since it is observed to occur with or without being in the vicinity of hydrodynamic modes. Cases of lateral mode excitation obvious in that they correspond more closely with lateral cavity modes than C4 frequencies, can be found without the presence of large amplitude waves excited by longitudinal modes, and

overlap with hydrodynamic modes show amplitude and spectral peaks of significance (see 2nd lateral cavity mode in 0.12 m case).

The non-linearity is also observed as seen by the secondary spectral peaks at higher frequencies. This is consistent with Rossiter's observations for an acoustically coupled system in air [24].

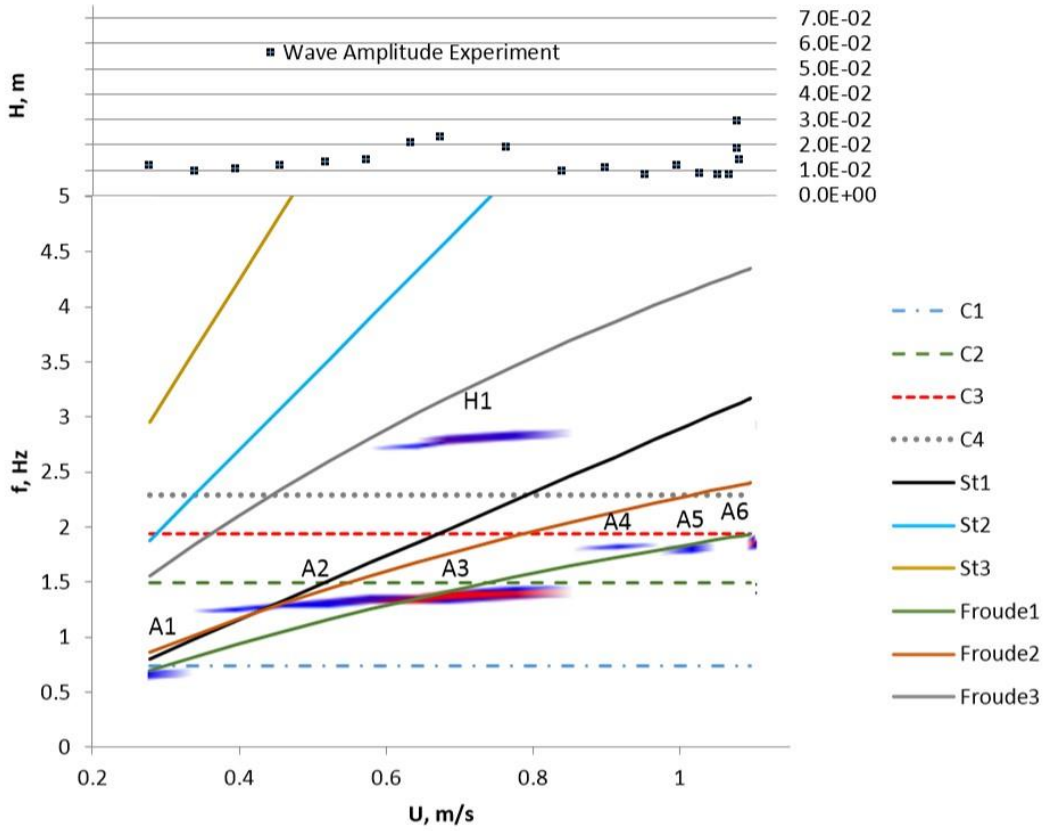

Figure 7.20: PSD frequency overlay along with cavity free surface height data (h=0.30 m).

It is unclear why A1 occurs near C1 where in all other depth cases no components of amplitude or spectral peaks were observed at the lower range of inflow velocities at C1 despite there being an overlap of predicted cavity and hydrodynamic frequencies at this point. This mode is also observed in the h=0.15 m and h=0.18 m cases where it is not in the vicinity of a hydrodynamic mode.

The comments on higher frequency components are difficult to compare in the frequency overlay and spectral contour format presented previously. They are best presented by some summarizing points on the higher harmonics given in the table below.

Table 7.1: Analysis of unaccounted for frequency components.

Depth	Harmonic of lower frequency near lateral mode	Lateral mode near hydrodynamic mode	Higher mode is a harmonic
0.30	H1	None	H1
0.27	H1 L1 L2	L1 L2	H1 L1 L2
0.24	H1 L1	L1	H1 L1
0.20	H1 L1	L1	None
0.18	L1	L1	None
0.15	H1	None	H1
0.12	L1	L1	None
0.09	H1	None	None

For 0.30 m, 0.27 m, and 0.15 m which are the large amplitude cases harmonics were observed near lateral modes and close to amplitude corrected C4 frequencies. In the case of 0.30 m and 0.27 m these were closer to the corrected C4 frequencies whereas the 0.15 m case corresponded slightly closer to the 1^{st} lateral cavity mode. Components near both lateral cavity modes and hydrodynamic modes corresponded to corrected C4 frequencies along with harmonics of the dominant frequency components. However, L1 for the 0.20 m, 0.18 m, and 0.12 m cases corresponded best with the 1^{st}, 1^{st}, and 2^{nd} lateral cavity modes respectively. Harmonics not in the vicinity of corrected C4 amplitude were observed for 0.20 m and 0.09 m cases. Based on these observations it can be concluded

that harmonics of large waves are observed for deep cases and are most commonly, but not exclusively, associated with frequencies close to higher cavity modes. Cases of lateral cavity mode excitement are obvious in that a distinct spectral and amplitude peak is observed; they occur at points closer to lateral cavity mode frequency and hydrodynamic mode interaction than they do to harmonics of the dominant mode. The harmonics not associated with lateral modes indicate that the second mode interactions are more complex and that as depth is increased non-linearities are introduced. Rossiter concluded that after reviewing the amplitude spectra of a shallow system it is typical to observe more than one spectral peak with similar amplitudes [26].

8 Appendix D
Free surface image tracking lens and high speed camera settings

Table 8.1: Lens and software parameters for free surface wave tracking.

Lens Settings	Software Settings	Frame Settings
1:2.8D	Gain 1.4	FR 30-60fps
16	Gamma 0.9	Skip save 10
4.25ft@16	Contrast 4	
	Brightness 11	